



NTNU – Trondheim
Norwegian University of
Science and Technology

Inclusion Optimized Silicon for the Production of Silicones

Andrea Broggi

Light Metals, Silicon and Ferroalloy Production

Submission date: June 2015

Supervisor: Halvard Tveit, IMTE

Co-supervisor: Elisabetta Gariboldi, Politecnico di Milano

Norwegian University of Science and Technology
Department of Materials Science and Engineering

PREFACE

This thesis concludes a Master of Science education in Light Metals, Silicon and Ferro alloy production at the Norwegian University of Science and Technology (NTNU), Norway. It will also be considered a valid thesis for the conclusion of a Master Degree in Materials Engineering and Nanotechnology at Politecnico di Milano, Italy, as the candidate was part of a Double Degree program between the two universities.

This work was carried out at the the Department of Material Science and Technology at the Norwegian University of Science and Technology, NTNU, Trondheim. Experiments have been performed also at Elkem Thamshavn. The work has been carried on by the interest of Elkem AS.

ACKNOWLEDGMENTS

I would like to express my gratitude to my supervisor from Norway Professor Halvard Tveit, Department of Material Science and Technology, NTNU, for the useful comments, remarks and engagement through the learning process of this master thesis. The weekly meetings with Halvard Tveit, Vegar Andersen and Kjell Håkon Berget have been an opportunity for me to have a challenge to face every week and motivated me to increase my knowledge on silicon in the upcoming future.

I would like to thank my supervisor from Italy, Professor Elisabetta Gariboldi, Department of Mechanical Engineering, Politecnico di Milano, for her objective point of view which was a necessary help for my research. The advices I received from her have been of outstanding importance, especially in the last part of this work.

Also, I would like to thank the participants in my survey, who have willingly shared their precious time during the process of researching. I would like to thank Professor Merete Tangstad and all the people in the SiManTi group. It was an important social environment which improved my skills as researcher and in moving criticism to myself and to who I will be dealing with in the future. Ingvill Vikan Myhre and Henning Kjørnli, for the industrial experiments performed with the help of the staff at Elkem Thamshavn, whose workers have already a very busy schedule. The people from Elkem Fossegrenda who have been interested in my work, especially Harry Rong and Torbjørn Røe. Professor Otto Lohne for his interesting suggestions from his wide knowledge of intermetallic phases. Jan-Otto Hoel for his extremely clear explanation of the fluidized bed reactor used in the silicones production. Birgitte Karlsen, Yingda Yi, Trygve Schanche, and Dimtry Slizovskiy for training me to use the laboratory equipment.

I would like to thank my loved ones, who have supported me throughout entire process, keeping me in harmony anytime I asked for help. My parents and my brother, which encouraged me with their best wishes. All the wonderful people I have met in these two years in Trondheim, especially Peace Kim, Bilal Khan, Feng Ni and Mazlum Boyaci, as well as all the friends which have supported me from Italy. A special thought goes to Matteo Carlessi, Stefano Cattaneo, Marcello Bolognini and Silvia Bianchi.

Thank you all for your patience and support.

ABSTRACT

One of the challenges with silicones production is the accumulation of impurities from metallurgical grade silicon (MG-Si) in the reactor. Size, shape and density of the intermetallics affect the accumulation, and their size distribution is also dependent on the thermal history of silicon. Different annealing treatments were carried out on MG-Si in order to investigate the re-ordering of the intermetallics from liquid state. The surfaces of the sample were analyzed with BSE-SEM images and the computer program ImageJ®. The results show that the size of the intermetallics increases with time and temperature, whereas aspect ratio and number of inclusions have the opposite trend. Temperature above 850°C is a necessary condition for transformations to start.

The composition has changed after a melting step was performed in air. XRF chemical analysis confirms the effects of oxidation refining and segregation. The software SiStruc® calculated the expected contents of phases based only on thermodynamics. EPMA and BSE-SEM image analysis estimated the phase composition on an untreated and on a treated sample. A comparison between expectations from SiStruc® and EPMA-BSE combined analysis is also presented. It can be stated that there could be reactions between intermetallic phases. The effects of the annealing and refining on the composition are compared to the expected change on reactivity and selectivity in the silicones production.

SAMMENDRAG

En av utfordringene med produksjon av silikon er akkumulering av intermetalliske urenheter fra metallurgisk silisium (MG-Si) i reaktoren. Størrelse, form og tetthet av de intermetalliske partiklene påvirker akkumulering, og størrelsesfordeling til partiklene er avhengig av den termiske historien til silisium under utstøpning. Forskjellige varmebehandlinger ble utført på MG-Si prøver for å undersøke omordningen av de intermetalliske partiklene fra flytende tilstand. Tverrsnitt ble sagd ut og overflatene av prøvene ble analysert med BSE-SEM-bilder. Bildene ble analysert ved hjelp av dataprogrammet ImageJ[®]. Resultatene viser at størrelsen av de intermetalliske partiklene øker med økende tid og temperatur under varmebehandlingen, mens sideforhold og antall partikler oppfører seg på den motsatte måten. Temperatur over 850° C er nødvendig for at denne transformasjonen skal skje.

Sammensetningen har endret seg etter silisium ble smeltet i luft. XRF analyser bekrefter effekten av oksidativ raffinering og segregering. Dataprogrammet SiStruc[®] ble brukt til å beregne de forventede mengdene av intermetalliske faser, basert kun på termodynamikk. EPMA og BSE-SEM bilder ble analysert for å beregne fasesammensetningen fra en ubehandlet og en behandlet prøve. En sammenligning mellom forventningene fra SiStruc[®] og resultatet fra EPMA-BSE analysen er også presentert. Reaksjoner mellom de intermetalliske fasene kan forekomme, i tillegg til de observerte endringene i kjemisk sammensetning. Basert på teori om intermetalliske fasers egenskaper i MCS prosessen, er det forsøk å predikere effekten av varmebehandling og raffinering av MG-Si til MCS prosessen. Prediksjonen har grunnlag i den estimerte fasefordelingen beregnet med SiStruc[®] ut i fra endringen i kjemisk sammensetning ved raffinering og varmebehandling.

Table of Contents

PREFACE.....	1
ACKNOWLEDGMENTS.....	3
ABSTRACT.....	5
1 INTRODUCTION AND PREVIOUS STUDIES.....	13
1.1 General information on silicon.....	14
1.2 Silicon production.....	16
1.2.1 <i>Production process.....</i>	16
1.2.2 <i>Oxidation and refining of MG-Si.....</i>	18
1.3 Heat transfer during solidification.....	21
1.3.1 <i>Heat transfer regimes.....</i>	22
1.3.2 <i>Solidification in an industrial and carbon mold.....</i>	23
1.3.3 <i>Effects of segregation.....</i>	25
1.4 Diffusion in silicon.....	27
1.4.1 <i>Fick's laws for diffusion.....</i>	28
1.4.2 <i>Diffusion mechanisms.....</i>	29
1.4.3 <i>Short-circuit diffusion regimes.....</i>	31
1.4.3.1 <i>Diffusion along grain boundaries.....</i>	32
1.4.3.2 <i>Previous works about diffusion in silicon.....</i>	35
1.4.4 <i>Diffusion-driven transformations.....</i>	38
1.5 Transformations driven by surface energy.....	39
1.5.1 <i>Splitting and coarsening of particles.....</i>	40
1.5.2 <i>Diffusion-controlled coarsening.....</i>	42
1.5.3 <i>Wetting on grain boundaries.....</i>	44
1.6 Annealing of Si-alloys.....	46

1.7 Binary and ternary systems in MG-Si.....	50
1.7.1 <i>Fe-Si system: the FeSi₂ phase transformation.....</i>	51
1.7.2 <i>Common intermetallics in MG-Si.....</i>	55
1.8 Sistruc®.....	57
1.9 Parameters influencing microstructure in the MCS production process...58	
1.9.1 <i>Influence of the fluidized bed reactor and particle size distribution.....</i>	58
1.9.2 <i>Influence of intermetallic phases.....</i>	61
1.10 Description of the case of study.....	62
2 SHAPE CHARACTERIZATION.....	64
2.1 EXPERIMENTAL.....	64
2.1.1 <i>Thermal history experiments.....</i>	64
2.1.2 <i>SEM analysis and geometrical parameters data collection.....</i>	66
2.2 RESULTS.....	67
2.2.1 <i>Untreated sample.....</i>	67
2.2.2 <i>Heat treated samples.....</i>	68
2.2.3 <i>Reference molten sample.....</i>	71
2.2.4 <i>Annealed samples.....</i>	71
2.2.5 <i>Cross-section temperature profile model.....</i>	72
2.3 DISCUSSION.....	73
2.3.1 <i>Mechanism of transformation.....</i>	74
2.3.2 <i>Aspect ratio.....</i>	76
2.3.3 <i>Area.....</i>	80
2.3.4 <i>Number of particles.....</i>	84
2.3.5 <i>Major and minor axis.....</i>	87
2.3.6 <i>Evaluation of uncertainties and further comments.....</i>	92
3 COMPOSITIONAL CHARACTERIZATION.....	93

3.1 EXPERIMENTAL.....	93
3.1.1 XRF analysis.....	93
3.1.2 EPMA and X-ray mapping.....	94
3.1.3 EDS-BSE-ImageJ [®] analysis.....	94
3.1.4 TFS (TiFeSi ₂) characterization.....	95
3.2 RESULTS.....	95
3.2.1 XRF and SiStruc [®] analysis.....	95
3.2.2 EPMA and BSE-SEM analysis.....	97
3.2.2.1 Untreated and treated sample at 600°C.....	97
3.2.2.2 Sample annealed at 1200°C.....	101
3.2.3 X-Ray mapping.....	103
3.3 DISCUSSION.....	106
3.3.1 Chemical analysis: refining and segregation effects.....	106
3.3.2 Kinetic effects: untreated sample.....	108
3.3.3 Chemical reactions: annealing effect.....	111
3.3.3 Minor elements in intermetallic phases.....	114
3.3.5 TiFeSi ₂ (TFS) geometrical characterization.....	115
3.3.6 Evaluation of uncertainties and further comments.....	122
4 CONCLUSIONS.....	123
5 FURTHER CHALLENGES.....	126
REFEFRENCES.....	128
APPENDIX.....	133
A. Analysis of the heat treated samples.....	133
B. Analysis of annealed samples.....	136
C. Chemical analysis.....	138

D. Position profiles in the samples analyzed.....	139
<i>D.1 Area</i>	139
<i>D.2 Aspect ratio</i>	142
<i>D.3 Counted particles</i>	145
<i>D.4 Major axis</i>	148
<i>D.5 Minor axis</i>	151

When he wins a battle, the warrior celebrates. This victory has cost him anxious moments, nights racked with doubt, endless days of waiting. [...] His companions see the warrior of light's joy and think: 'Why is he doing that? [...] He is savouring the best gift that victory can bring: confidence. He celebrates yesterday's victory in order to gain more strength for tomorrow's battle.

(P. Coelho, "The manual of the warrior of the light")

1 INTRODUCTION AND PREVIOUS STUDIES

Silicon and its alloys play a relevant role in everyday life. This element is a valuable and abundant resource. It can be used as an alloying element in aluminum and steel, main component of silicones and electronic products. Its abundance is due to the high amount of SiO_2 in the earth crust. This can be explained by the high stability of the bonding between the two elements contained in the oxide. However, for the same reason, high energy input and reducing agents are required to produce elemental silicon. Silicon has to be separated from oxygen at such high temperatures that it would transform into a liquid. Once solidified, it is crushed to the optimal size and shape for further application.

Silicones production is the most valuable application of silicon in chemical industry. In this process, solidification of elemental silicon is an important step for the product quality. The thermal history of solidification has to be controlled to obtain a wanted microstructure of the material. Changes in shape and composition of the intermetallic compounds occur during solidification. The driving forces of these transformations are mainly diffusion and surface energy reduction. The mechanism of these transformations needs to be understood from thermodynamics, as well as from results and hypothesis from previous works.

Different phases can be generated according to the starting composition of the material and the diffusion rates of the element through the matrix or the grain boundaries. A software developed after experimental studies can help us understand which phases can be formed at a given starting composition. Previous works show that the reactivity and selectivity of the silicones production reaction are affected by the presence and the amount of different intermetallic phases.

1.1 General information on silicon

Silicon is the 14th element in the periodic table and belongs to the group 4A (carbon group). It can be considered as the “building block” of many substances found in nature, as described by **Zumdahl (2007)**. *“Silicon is an important constituent of the compounds that make up the earth’s crust. In fact, silicon is to geology as carbon is to biology. Just as carbon compounds are the basis for most biologically significant systems, silicon compounds are fundamental to most of the rocks, sands, and soils found in the earth’s crust”*. It is not a coincidence that most of the rocks, sands and soil contain silicon or its compounds, such as silica (SiO_2) or silicates. Its great affinity to oxygen forms stable bounds and crystalline structures which can resist at high energy input.

The element was discovered 200 years ago by the Swedish chemist Jöns Jakob Berzelius. The electric arc furnace technology developed 100 years ago for silicon and ferro-silicon production. The invention of the Söderberg electrode technology further improved the production at industrial scale. Nowadays, the main applications of silicon are aluminum alloys, electronic and solar applications, and silicones production.

The silicones production process used nowadays was developed by Dr Eugene Rochow, and consists in the production of dimethyl-dichlorosilane (MCS). Since the discovery of this process, silicones' industry has grown up to a strong and valuable business.

This product will behave as precursor to a wide variety of compounds, called silicones. A silicone is a polymer, which has a Si-O-Si backbone, combined either in chains or rings. As well as organic polymers, silicone can contain substitute groups, such as carboxyl (-COOH), hydroxyl (-OH), or carbonyl (=O). This feature is common between silicon and carbon, since they belong to the same group in the periodic table. Silicones are frequently used in a wide range of applications: water repellent products or cable insulation, as well as additives to medicines or make-up products.

The purity of silicon required for silicones production is not as strict as the one required for electronic applications. Metallurgical-grade silicon (MG-Si) can be used in the first case, whereas solar-grade silicon (SoG-Si) can be used in the second. The former can be produced in an electric arc-furnace and its impurity content can vary between 1-4%wt. The latter requires a energy-consuming refining process from MG-Si to decrease the impurity content down to ppm or ppb level. The techniques used are vacuum and ladle refining, as well as distillation and thermal decomposition (Siemens process).

The amount of silica and quartz in the earth crust is high, but not infinite. Soon it will be important to develop efficient refining techniques to reduce (or control) the quantity of unwanted elements. Some of them are improving year by year, such as vacuum and slag refining, as well as leaching and directional solidification.

As the silicon demand is increasing, the industry has to find the most convenient way to decrease costs, increase product quality and deal with health, safety and environment (HSE) issues, access to energy and raw materials. Figure 1 shows the increase in consumption of silicon from 2000, and the forecast consumption until 2019.

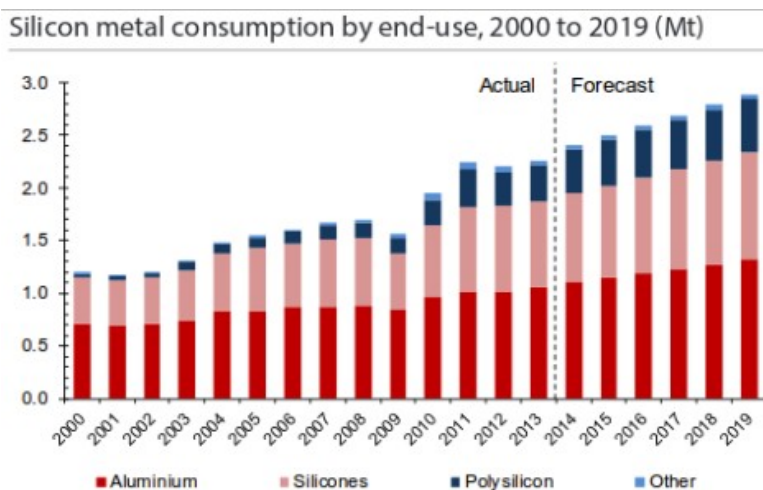


Fig. 1: Silicon consumption in its different main applications (Roskill, 2013)

1.2 Silicon production

1.2.1 Production process

Silicon is produced in submerged arc furnaces by carbothermic reduction. An overview of the process is shown in Figure 2. A charge of quartz and carbonaceous materials (in the form of coke, coal, charcoal and woodchips) is fed into the furnace from the top. As fed through the furnace, it undergoes a series of reactions, which reduce SiO_2 to Si. The silicon production reaction can be summed up by the following reaction:

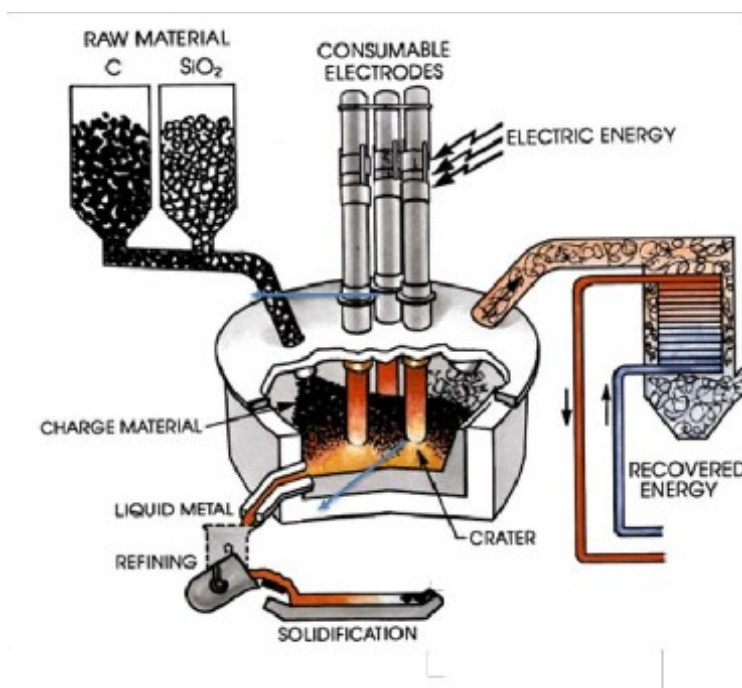
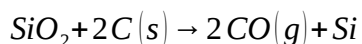


Fig. 2: Silicon production process (Schei et al., 1998)

Energy is supplied to the process from electrodes in the form of electricity, as well as chemical energy from the combustion of carbon and other volatiles.

During this process the temperature in the furnace can reach as high as 2100°C (Schei et al. 1998). The off-gas contains SiO, which oxidizes to produce Microsilica[®], a valuable by-product for further applications in cementitious materials.

Dissolved Ca and Al are always present in the furnace product, and inclusions will form in silicon by reaction with dissolved oxygen. To control the formation of the inclusions, the liquid is tapped into a ladle for a refining process. In this stage, Al, and Ca impurities are removed by oxygen bubbling. Two phases with different densities will form. Since the slag phase will be in equilibrium with the silicon phase, it is possible to control the composition of the silicon phase. Thus, oxygen is added to optimize the composition of the system. Its effect is to oxidize the impurities less noble than silicon and transfer them to the slag phase to the desired extent. However, silicon can be oxidized and some off-gas can be produced. Therefore it is important to control the oxygen flux. Besides, slag forming components (SiO₂-CaO mixture) can be added on purpose to adjust the slag composition.

The typical composition of tapped silicon is shown in Table 1. These numbers indicate the orders of magnitude of impurity content in MG-Si. Impurities can come from Söderberg electrodes (especially as far as Fe is concerned), raw materials, tapping and refining and solidification procedures. The composition range is quite wide, but MG-Si contains between 96-99 %wt silicon.

Table 1: Concentrations of some of the intermetallics present in MG-Si (Ceccaroli et al., 2003)

Element concentration	O	Fe	Al	Ca	C	Mg	Ti	Mn
Low (ppm)	100	300	300	20	50	5	100	10
High (ppm)	5000	25000	5000	2000	1500	200	1000	300

Once the two phases are separated, liquid silicon is cast into iron molds, where the solidification process occurs. Silicon fines are added at the bottom of

the mold before casting to prevent contamination from the lining materials and thermal shocks. In the end, the solidified product is crushed, milled to the desired size and ready for the chosen application.

1.2.2 Oxidation and refining of MG-Si

A slag layer is formed when melting MG-Si. Elements tend to be involved to different extents in the oxidation reaction. This is caused by thermodynamics and kinetics of oxidation.

Thermodynamic effects are presented in Figure 3, which shows the Ellingham diagram. ΔG and temperature are plotted respectively on the vertical and on the horizontal axis. Each curve corresponds to the oxidation reaction of an element. In all the oxidation reactions, the higher the temperature, the higher the ΔG . When $\Delta G=0$, the reaction is at equilibrium. No elements except Au and Ag reach this value at low temperatures. According to thermodynamics, all the elements presented in Figure 3 should exist as oxides in the ranges of temperature of Si refining (1400-1600°C). The elements with lower ΔG will oxidize easier. The slag will mostly contain CaO, SiO₂ and Al₂O₃. Ti makes an exception due to its low activity in the system. Most of the Mg evaporates at 650°C.

Despite their negative ΔG , elements such as Fe, Mn and Cr will not be present in considerable amounts in the slag. Once silicon is solid, no impurities will be able to move to a slag phase. Therefore, these elements will be retained in silicon and will not undergo oxidation. A useful parameter can be introduced when solidification of silicon and repartition of elements is concerned. The *segregation (or partition) coefficient* is the ratio between the quantity of an element in silicon and the quantity in a slag phase. **Morita (2003)** has performed a study about refining of MG-Si to SoG-Si by slag refining techniques. Knowing the value of partition coefficient is crucial if one wants to state whether elements are suitable for slag refining techniques or not. Besides,

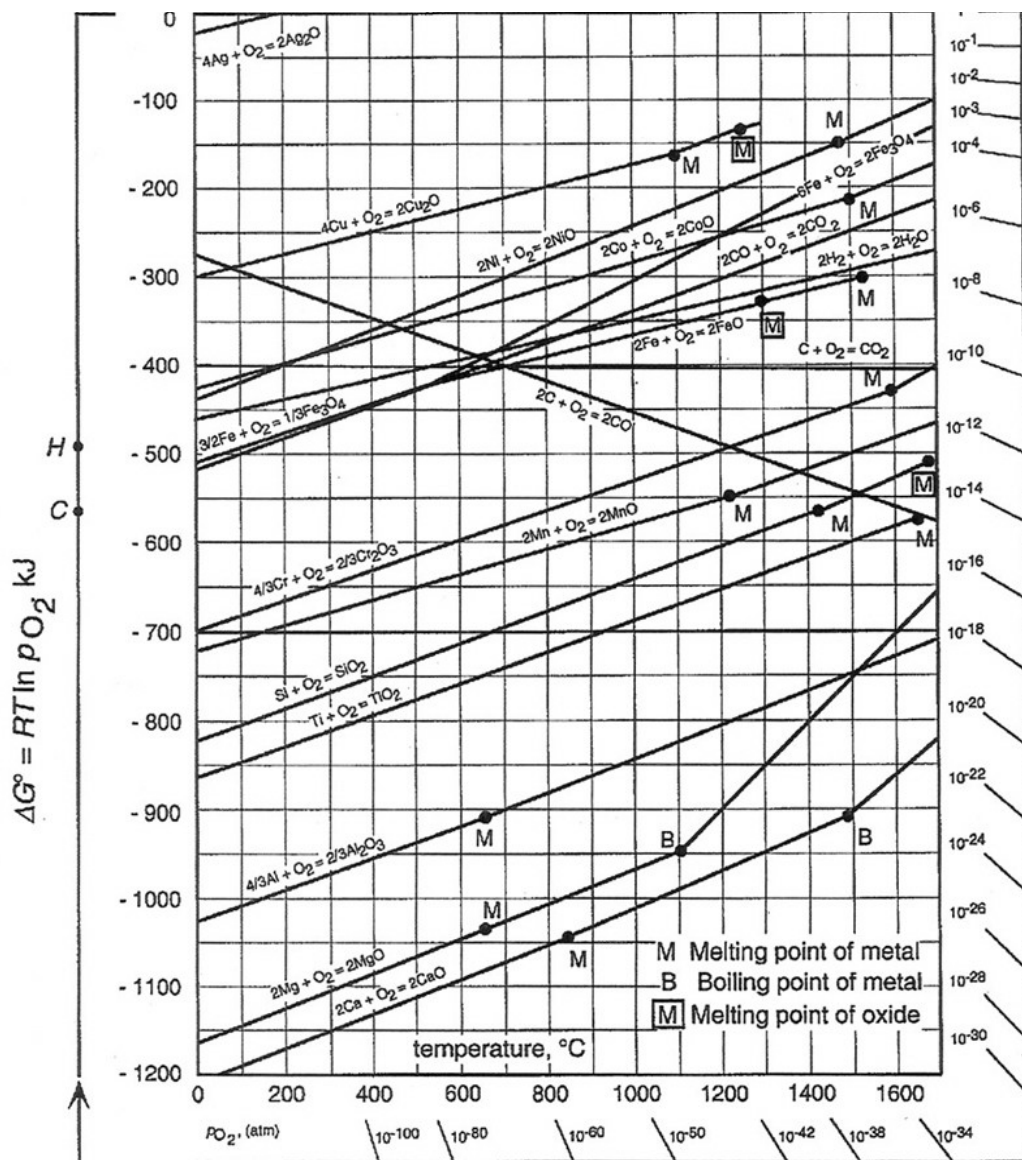


Fig. 3: Ellingham diagram for different oxides (Gaskell, 2010)

effective treatments for impurity removal are suggested. Figure 4 resumes the considerations formulated about this issue.

Table 2 lists the segregation coefficients for slag refining of silicon. These

values have been collected from a work performed by **Hopkins et al. (1986)**. Ti and Fe have a significantly smaller coefficient than Al. Calcium's segregation coefficient was not calculated, but it is known from experience that high quantities of this element can go to a slag phase, i.e. the partition coefficient can be greater than 1. It is also interesting to note that Ca can evaporate when Si is melting, hence the necessity of Ca addition during the refining step for MG-Si.

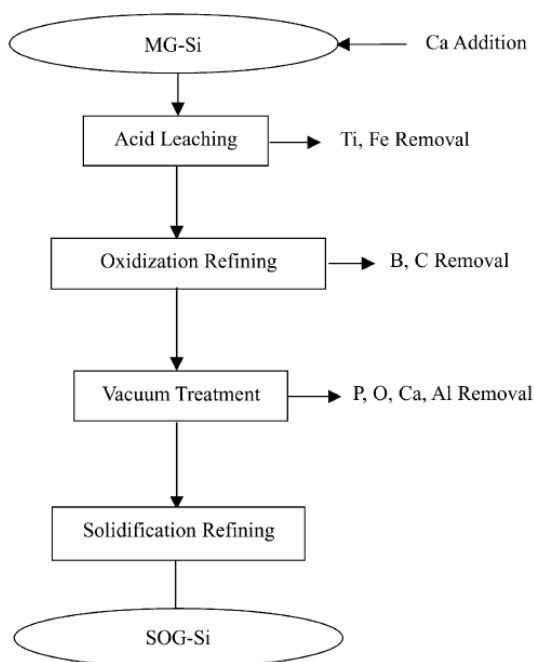


Fig. 4: Proposed low-cost method for MG-Si refining to SOG-Si of different elements (Morita, 2003)

Table 2: Segregation coefficients (Hopkins et al., 1986)

Element	Segregation coefficient
Fe	6.4×10^{-6}
Ti	2.0×10^{-6}
Al	2.8×10^{-3}

1.3 Heat transfer during solidification

When a material solidifies, its enthalpy changes. The variation will be negative in this case, i.e. heat is extracted from the melt to the environment. The change in enthalpy in this case can be quantified by the well-known formula

$\Delta H = \Delta H_f + \int C_p dT$, where ΔH_f is the latent heat of solidification of the material and C_p corresponds to its thermal capacity. It is clear that the enthalpy variation is a function of temperature. It cannot be so immediate to understand that the composition of the melt has also an influence. In Figure 5 ΔH is represented as a function of temperature for different amounts of silicon in a cast. The latent heat of solidification is the amount of energy lost at the melting point temperature, which also varies with composition. The latent heat is peculiar for each material. Silicon has a ΔH_f which is almost 5 times higher as the one for Fe or Al, for instance. Latent heats of the most common impurities are listed in Table 3.

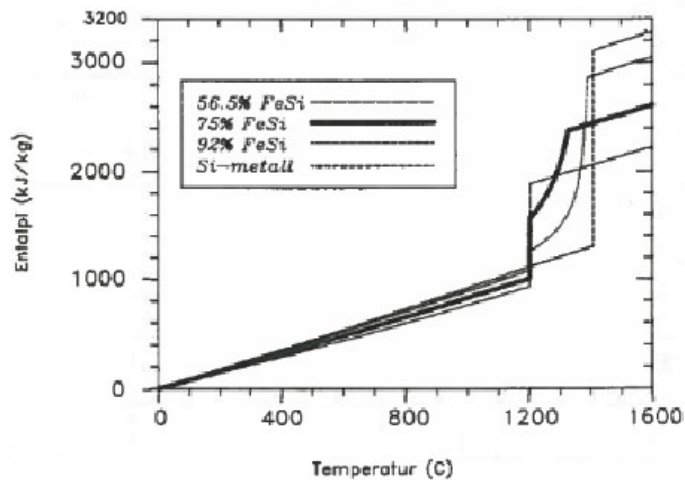


Fig. 5: Enthalpy in Fe-Si alloys from 0 to 1600°C (Tveit, 1988)

Table 3: Latent heat of fusion of the elements involved in MG-Si (Aylward et al., 2008)

Element	Latent heat (kJ/mol)
Si	50
Al	11
Ca	8.5
Fe	14
Ti	15

1.3.1 Heat transfer regimes

Silicon exchanges heat to the environment through three different ways: conduction, convection and radiation (**Incropera et al., 2002**). All these three mechanisms generate a net heat flux which goes towards the region at lower temperature.

When molecules move in a solid, liquid or gas, and heat is transported because of collisions, vibrations and free electrons migration, conduction occurs. No bulk movement is involved, i.e. no bulk flow of matter is related to heat transfer. The contact between two interfaces, such as liquid silicon and the mold walls, is the only cause of conduction. In the contact space, a temperature gradient is formed. Higher temperature gradients increase the molecular energy, thus increasing the heat exchange developed by conduction. Fourier's law expresses the rate of conductive heat transfer

$$q = -k \frac{dT}{dx}$$

where k is the thermal conductivity of the material and $\frac{dT}{dx}$ expresses the temperature gradient.

Convection takes place when heat exchange is related to bulk motion of matter, or mixing. It assumes two different names according to the positions involved in the system. If the volume close to the surface is considered, then it is controlled by diffusion. A boundary layer separates the diffusion controlled

region from the bulk region. Temperature and velocity profiles are developed in the boundary layer, whereas the bulk temperature and velocity are constant and easily measurable. Convection can be forced or natural, according to the cause of the driving force. The temperature difference is the driving force. This must not be mistaken with the temperature gradient involved in conduction. Convection heat exchange rate follows Newton's heat exchange formula $q=h(T_s - T_\infty)$, where h is the convective heat transfer coefficient and T_∞ is the surface temperature. h depends on the condition at the boundary layer. In silicon solidification, convection takes place in the first instants of the casting step, when liquid silicon is poured in the mold.

When electromagnetic waves are involved, the heat exchange mechanism is called radiation. There is no contact between two surfaces exchanging heat through radiation, since electromagnetic waves can propagate in void. The next heat exchange flux by radiation is quantified by the law $q=\sigma\varepsilon(T_s^4 - T_{sur}^4)$, where σ is the Stefan-Boltzmann constant, ε is the emissivity (assumed equal to absorptivity), T_s is the surface of the emitting body and T_{sur} is the surrounding environment temperature. Radiation is the predominant heat exchange mechanism at high temperatures, especially during silicon solidification. The heat amount released can be so high during silicon production that it could be reasonable to recover some heat through thermoelectric materials, as suggested by **Lobo (2010)**.

1.3.2 Solidification in an industrial and carbon mold

Now that the heat exchange mechanisms are known, it can be possible to explain and understand how solidification of silicon in thin casting mold occurs. M.F. Møll has carried on a study about the solidification of silicon in an industrial size mold and its consequences on the microstructure (**Møll, 2014**). A mathematical model of silicon solidification was designed in COMSOL[®] in order to explain the higher concentration of impurities in the center rather than

at the edges of a thin cast. Liquid silicon is poured into a mold covered with fines at the bottom to avoid contamination. As the heat is released from the melt to the surroundings, room temperature is reached due to a change in the enthalpy of the material. The amount of heat during the transformation from liquid to solid state corresponds to the latent heat of solidification of the material.

The resistance to heat transfer to the surroundings influences the rate of heat removal during the solidification. Also, the conductivity of solid silicon can be significant. However, this parameter is not decisive at the high heat conduction rates values found in casting processes such as thin casting. Figure 6 shows the configuration of the process and how the solidification goes on at different snapshots.

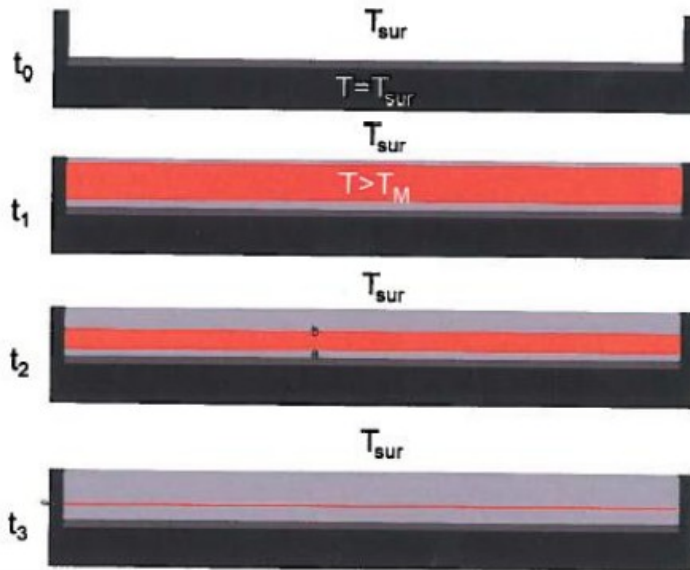


Fig. 6: Heat flow during solidification at time t_0 , t_1 , t_2 and t_3 . The mold is illustrated in black, the fines in dark grey, liquid silicon in orange and solid silicon in light grey (Møll, 2014).

t_0 is the snapshot prior to filling of the mold, where all the surfaces are at room temperature.

t_1 corresponds to the instant after the filling of the mold. The difference between the temperatures of the melt and the mold is large. Solidification starts instantly at the mold wall due to conduction. From the top surface, heat will be lost through both radiation and convection. Heat will be transported by conduction through the solid silicon. At the solid-liquid interface latent heat will be released. The enrichment of alloying elements in the liquid increases the density of the liquid. Low density silicon will therefore float at the top, while higher density liquid will sink.

At t_2 , the heat will be transported in the direction where the temperature gradient is largest. Two solidification fronts will develop, one moving downwards and one moving upwards. The rate of their movement will depend on how fast the heat is removed from the top and the bottom.

At t_3 , since there has been macro-segregation of alloying elements in the liquid during solidification, the area where the two fronts meet is enriched in alloying elements.

When a carbon mold is used instead of a steel one, the solidification is also fast, but the solidification front speeds are altered. The mechanisms are still the same, i.e. radiation and convection at the top and conduction at the bottom. However, the solidification front coming from the top moves much faster compared to the front coming from the bottom. The heat exchange with silicon at this point of a mold with poor thermal properties is very small. The low thermal conductivity of carbon reduces the conductive heat exchange rate. The speed slows even more if the mold is also heated, thus reducing the temperature difference with the liquid metal. The impurities accumulate in the liquid phase and precipitate as intermetallics at the bottom of the cast.

1.3.3 Effects of segregation

“A worker in refining metallurgy is not only concerned with attaining the specified mean composition of his melt; he must also take into considerations what happens during solidification” (Engh, 1992). The variation of the

impurity distribution must be understood and related to the solidification process. Such phenomena are respectively called micro- and macro-segregation.

Micro-segregation occurs within distances of the order of a dendrite size. It is driven by the variation of solute in the liquid compared to the solid. It can be described in an easier way if it is assumed that no diffusion occurs in the solid, the liquid is uniform in composition and there is no back-diffusion from the solid to the liquid. These are the condition under which the Scheil equation is formulated as

$$\frac{c_s}{c_0} = kf^{k-1}$$

with:

c_s = solid concentration, after solidification

c_0 = concentration before solidification

k = partition coefficient

f = liquid fraction

The partition coefficient is the ratio between the element quantities in the solid and in the liquid. It represents how much an element can be affected by segregation. If $k=1$, no segregation occurs. If k tends to 0, the solute is found in the highest quantity in the last fraction which solidifies. k can change to a smaller value, called k_{eff} , if the effects of back diffusion from the solid are considered.

The Scheil equation can be also used to describe macro-segregation. In this case, the distance involved is the whole cast profile. Macro-segregation is not always a clever solution for decreasing element in the cast. If the cooling rate is too fast, it would just result into accumulation of impurities in certain parts, rather than into a decrease in impurities. The main causes of macro-segregation are the difference in solute content between a solid and a liquid phase, as well as the different solubility of the element within the phases. **Engh (1992)** quotes

an example of macro-segregation in silicon. A study of a FeSi casting is considered. When a liquid containing 75%wt. Si and 25%wt Fe is molten, Si starts to precipitate at 1315°C. The liquid will be rich in Fe until the eutectic point is reached. Cooling from the bottom can start segregation occurring from this point. When a block is directionally cooled from the top, segregation occurs at the top. Silicon will precipitate at the solidification front and the melt will be richer in Fe. Being heavier, the impurity-rich liquid will sink. Once the liquid has solidified, a concentration profile is generated. Equations describing macro-segregation are derived from Scheil equation. One of them is Flemings equation, which describes macro-segregation as a result of interdendritic flow (**Flemings, 1971**).

$$\frac{\partial f}{\partial c_i} = -\left(\frac{1-\beta}{1-k}\right)\left(1 - \frac{v}{dz/dt}\right)\frac{f}{c_i} \quad \text{or} \quad \frac{\partial f}{\partial c_i} = -\left(\frac{1-\beta}{1-k}\right)\left(1 + \frac{v \partial T / \partial z}{\partial T / \partial t}\right)\frac{f}{c_i}$$

with

$$\beta \quad \text{defined as} \quad 1 - \beta = \frac{(\rho_s - \rho)}{\rho}$$

$\partial z / \partial t$ = solidification front velocity

$\partial T / \partial z$ and $\partial T / \partial t$ = partial derivatives of the temperature profile of the solidification front expressed by the function $T(z,t)$

v = local velocity of the interdendritic liquid relative to the solid

1.4 Diffusion in silicon

Diffusion of interstitial elements can be a relevant mechanism of microstructural variation at the ranges of temperature which silicon undergoes during solidification. The diffusion coefficients are also a function of temperature and follow Arrhenius law. This part will describe in detail the thermodynamics of diffusion regimes in solid state. If not specified, the material from this chapter is from **Sutton and Baluffi (1995)**, **Hondros (1983)** and

Shewmon (1989).

1.4.1 Fick's laws for diffusion

Diffusion consists in the transport of chemical species which develops in a system out of equilibrium. The system presents a chemical potential gradient. A concentration gradient is a more understandable and concrete concept than a chemical potential gradient: Fick's law is therefore commonly used

$$\vec{J}_i = -D_i \frac{dC_i}{dx}$$

The proportional factor between the flux and the concentration gradient is termed diffusivity, or intrinsic diffusion coefficient. Its dimensions is an area divided by time. If we consider the time evolution of the concentration profile, $C(x, y, z, t)$, this can be determined by differentiation of the previous equation. Fick's second law is found, and represents nothing more than a material balance as a function of time and position.

$$\frac{dC_i}{dt} = \frac{d}{dx} \left(D_i \frac{dC_i}{dx} \right)$$

The gradient in this potential is the driving force for diffusion. A diffusional flux will then arise. It will be proportional to the diffusion potential gradient. The most important quantities involved are $\vec{J}_i(\vec{r})$ (flux of component i , mol s m⁻²) which describes the rate at which i flows through a unit area fixed with respect to a specified coordinate system, and C_i , i.e. the number of moles of component i per unit volume.

During self-diffusion in a pure material, whether a gas, liquid, or solid, the components diffuse in a chemical homogeneous medium. The flux of the component i can be written in terms of the chemical potential or in terms of the concentration

$$J_i = -M_i C_i \frac{d\mu_i}{dx} = -D_i \frac{dC_i}{dx} \quad \mu_i = \mu_i^0 + RT \ln(a_i) = \mu_i^0 + RT \ln(n_i \gamma_i)$$

where

M_i = mobility of the element i

μ_i^0 = chemical potential of i in reference state

a_i = activity of i

γ_i = activity coefficient of i

n_i = atomic fraction of i

By substituting the second equation in the first, and assuming Henry's law condition (i.e. dilute solution) the diffusion coefficient can be expressed as

$D_i = M_i RT \cdot \ln a_i$. Deviations due to the activity coefficient can be introduced, and resumed by the following law:

$$\frac{D_i}{M_i RT} = 1 + \frac{d \ln(\gamma_i)}{d \ln(n_i)}$$

Alloys tend to be more ideal with rising temperature. Any deviation from

$\frac{D_i}{M_i RT}$ will then decrease.

1.4.2 Diffusion mechanisms

It is assumed that diffusion in solids occurs by the periodic jumping of atom from one lattice site to another. The diffusion coefficient can be related to the jump frequency by considering two adjacent lattice planes. Atomic jumping in a crystal can occur by several basic mechanisms, The dominant mechanism depends on crystal structure, nature of the bonding in the host crystal, relative differences of size and electrical charge between the host and the diffusing species, and the type of crystal site preferred by the diffusing species. A substitutional atom can migrate to a neighboring substitutional site without cooperative motion and with a relatively small activation energy, if the neighboring substitutional site is unoccupied. In the following figure, the vacancy is initially separated from a particular substitutional atom (indicated by shading). In Figure 7b, it has migrated by exchanging places with host atoms to

a nearest-neighbor substitutional site of the shaded atom. In Figure 7c the vacancy has exchanged sites with the substitutional atom, and in Figure 7d the vacancy has migrated some distance away. As a result, the particular substitutional atom is displaced by one nearest-neighbor distance, while the vacancy has undergone at least five individual displacements.

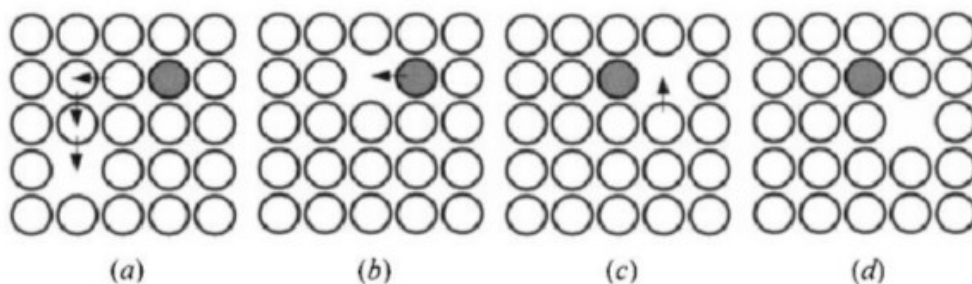


Fig. 7: Vacancy mechanism for substitutional diffusion

Interstitial sites are a set of atomic positions distinct from the lattice sites; here, typically, smaller atoms than the ones which constitute the crystal can locate. In the following figure we see the interstitial sites in a lattice. The interstitial atom must attain enough energy to distort the host crystal as it migrates between substitutional sites. This mechanism is expected for small solute atoms that normally occupy interstitial sites in a host crystal of larger atoms.

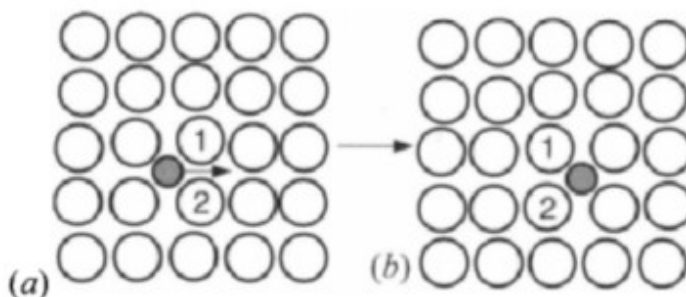


Fig. 8: Schematic representation of interstitial diffusion

1.4.3 Short-circuit diffusion regimes

Rapid diffusion along line and planar crystal imperfections occurs in a thin region centered on a defect. For a grain boundary, the region is a thin slab, roughly two inter-atomic distances thick, including the material in the grain boundary core. These regions are very thin in comparison to the usual bulk diffusional transport distances. Thin slabs or cylinders of effective thickness δ can replace imperfections and help in modeling diffusion. Effective diffusivities at this points are larger than the diffusivity in the adjoining crystalline material.

Figure 9 presents self-diffusivity data for FCC metals on a single Arrhenius plot. With the exception of the surface diffusion data, the data are represented by ideal straight-line Arrhenius plots. If the various activation energies were independent on temperature, the curves would be realistic. At temperatures below the melting point there are different kinds of diffusivity, the one in the lattice D^{XL} typically is lower than the boundary D^B . When the temperature is growing the ratio between the two mechanisms becomes smaller. D^S has lower activation energy and rising diffusivity. Moreover, when the temperature

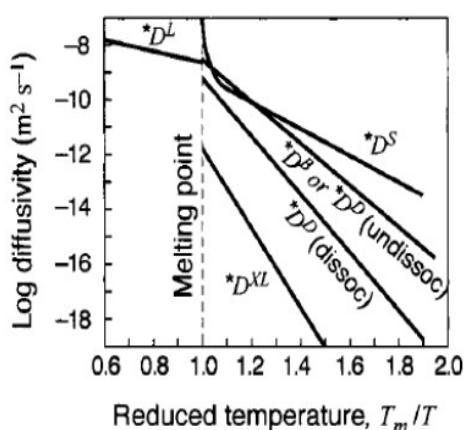


Fig. 9: Arrhenius plot for different kinds of diffusivity. The ones considered will be D^B (at grain boundary), D^{XL} (in bulk crystal), D^S (along a free surface)

approaches the melting point, the atoms in the surface become almost free. In this graph the activation energy is a constant, as far as interfaces are not involved. In this case different coordination numbers lead to have different activation energies.

It is possible to calculate a parameter called diffusion length by using the simple formula

$L=2\sqrt{Dt}$. L is defined as a measure of how far the

concentration of an element with diffusion coefficient D has propagated in a direction by diffusion in time t (**Bird, 1976**). Short-circuit diffusion in polycrystalline materials with stationary grain boundaries can be classified in three regimes, according to the comparison between the diffusion length and the grain size of a material:

A. Multiple-boundary diffusion regime. Since the diffusion field overlaps multiple boundaries, each diffusing atom is able to diffuse both in the grains and along several grain boundaries during the diffusion time available. The diffusion in the system therefore behaves macroscopically, as if bulk diffusion was occurring in a homogeneous material with uniform diffusivity. Fast grain-boundary diffusion will cause preferential diffusion to occur along the narrow grain-boundary cores beyond the main diffusion front, but the number of atoms will be relatively small and this effect cannot be depicted;

B. Isolated-boundary diffusion regime. The diffusion length in the grains is significant but smaller than the grain size. In this regime, the diffusant moves along a boundary while simultaneously leaking out by diffusing into the adjoining grains. An analysis of this type of diffusion is considerably more complex than for diffusion in the A and C regimes since it involves solving for the coupled diffusion fields in the grain boundary and in the adjoining grains;

C. Grain-boundary diffusion regime. As the bulk diffusion length is negligible, significant diffusion occurs only in the thin grain-boundary slabs.

1.4.3.1 Diffusion along grain boundaries

During grain-boundary diffusion, an atom will move between various types of sites in the core and jumps will have different activation energies. The overall diffusion rate is therefore not controlled by a single activation energy. In addition, Arrhenius plots for grain-boundary diffusion should exhibit some curvature. However, such curvature may be difficult to detect when the data are of moderate accuracy and exist over limited temperature ranges.

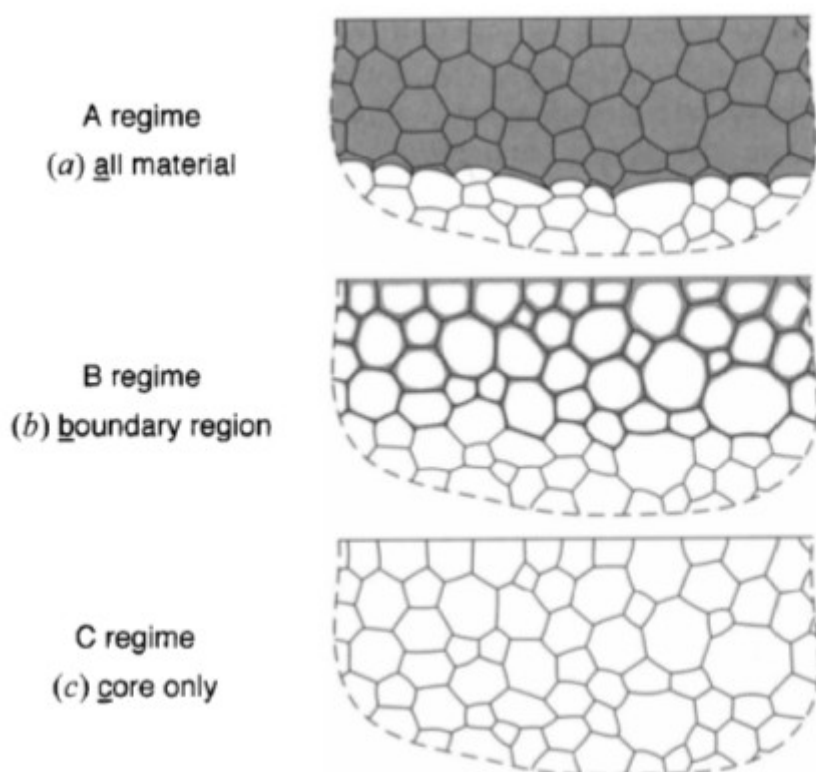


Fig. 10: The A, B and C regimes for self-diffusion in a polycrystalline material with stationary grain boundaries.

Grain-boundary diffusivities in metals at $T=0.5T_m$ are 7 to 8 orders of magnitude larger than crystal diffusivities. Provided that defects are present at sufficiently high densities, significant amounts of mass transport can occur in crystals at surface and grain-boundary diffusion even though the cross-sectional area is relatively very small. As the temperature is lowered further, the ratio of diffusivities becomes larger and short-circuit diffusion assumes even greater importance. There are many situations, particularly at low temperatures, where diffusion along grain boundaries is the dominant mode of diffusional transport and therefore controls important kinetic phenomena in materials.

The diffusion rate along small-angle grain boundaries is generally lower than

along large-angle grain boundaries. It approaches the diffusivity in a bulk crystal free of imperfections as the crystal misorientation approaches zero, i.e. the two crystals have the same orientation angle. This event is due to two factors. First, the diffusion rate along a dislocation core is lower than along large-angle grain boundary cores. Second, the density of fast-diffusion paths is smaller in small-angle grain boundaries than in large-angle grain boundaries. Small-angle grain boundaries consist of periodic arrays of lattice dislocations at discrete spacings that approach infinity as the crystal misorientation approaches zero. Figure 11 presents diffusivity data for a series of tilt boundaries as a function of the misorientation tilt angle. The structures of these boundaries vary considerably as the misorientation changes. In the central part of the plot, the minima occur at crystal misorientations (values of θ) corresponding to singular boundaries. The ends of the plot (where the crystal misorientation approaches zero) correspond to small-angle grain boundaries, and the diffusivities are correspondingly low. The regions centered around the maxima correspond to general grain boundaries.

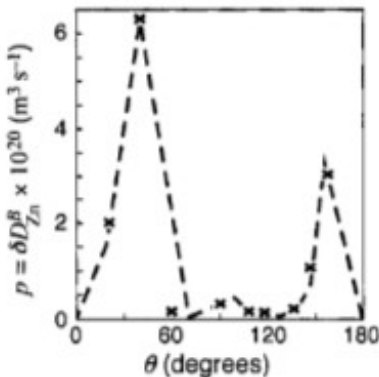


Fig. 11: Grain boundary diffusivity of Zn along the tilt axis [110] symmetric tilt grain boundaries in Al as a function of the tilt angle (Sutton and Baluffi, 1995)

In a poly-crystal containing a network of grain boundaries, atoms may migrate in both the grain interiors and the grain boundary slabs. They may jump into or out of boundaries during the time available, and spend various lengths of time jumping in the grains and along the boundaries. Widely different situations may occur, depending upon such variables as the grain size, the temperature, the diffusion time. At elevated temperatures the importance of the boundary diffusion will be diminished. At very long diffusion times, the distance each atom diffuses will be relatively large, and each atom will be

able to sample a number of grains and grain boundaries. If the boundaries are moving, an atom in a grain may be overrun by a moving boundary and be able to diffuse rapidly in the boundary before being deposited back into crystalline material behind the moving boundary.

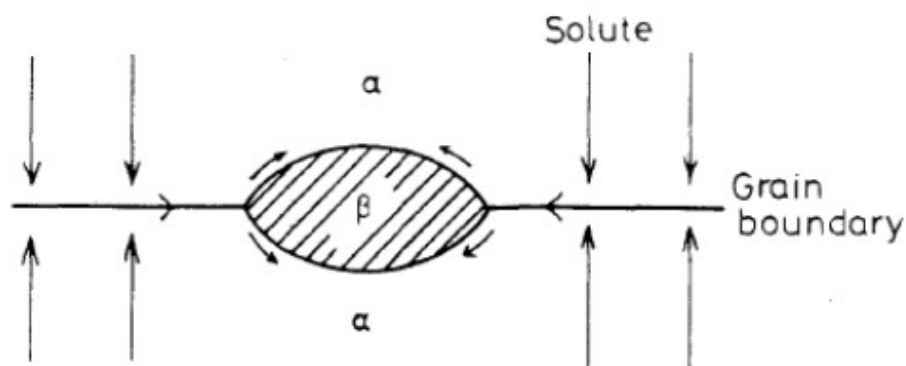


Fig. 12: Grain boundary diffusion can lead to rapid lengthening of grain boundary precipitates

1.4.3.2 Previous works about diffusion in silicon

Many studies have been performed about bulk diffusion in silicon of the most common impurities: their results are gathered in the book by **Fisher (1998)** and collected in Table 4.

Measurements of diffusion coefficient and activation energies have been performed by different researchers. Unfortunately, there is not a complete agreement between the different results. According to **Graff et al. (1981)**, “*the spread of values can be caused by (i) additional undesired impurities introduced especially during extended treatments of the specimens at high temperatures, (ii) iron [or other diffusants – Ed.] reactions with dopant atoms or other impurities, and (iii) precision of differing method for the determination of the activation energy*”. In order to inquire bulk diffusion coefficients, n- or p-doped silicon polycrystalline materials with known thickness are usually studied. The diffusant is inserted as dopant in the matrix by evaporation.

Annealing at different times and temperature are able to quantify the diffusion coefficient of silicon. A concentration vs temperature plot is derived. By using Fick's laws, D_i is derived as a function of temperature. This procedure has been followed by **Isobe et al. (1989)** and **Collins et al. (1957)**. Once D vs T has been plotted, D_0 and E_a are derived respectively by extrapolation at $T= 0$ K and by the slope of the graph D vs $1/T$.

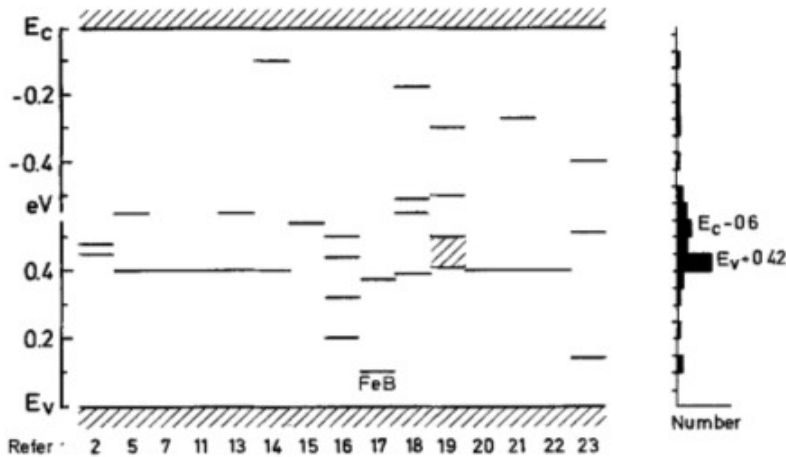


Fig. 13: Activation energies of bulk diffusion of iron in silicon as published in the literature. The references numbers come from **Graff et al. (1981)**

Table 4: Bulk diffusivity parameters in silicon for common impurity elements present in silicon (Fisher, 1998)

Diffusant	Temperature range (°C)	Diffusion parameters D_0 (cm^2/s)	Activation energy (eV)
Al	-	8.0	3.47
Fe	800-1070	0.02	0.71
Ti	600-1150	0.12	2.05
Si	800-1200	0.006	3.3

Short-circuit diffusion measurements have also been performed. The

experiments are carried out at lower temperatures (25-600 °C). Activation energies and diffusion coefficients have been estimated by different authors.

The method used is quite peculiar. As it is very difficult to isolate the measurement of the diffusion at the grain boundary, similar conditions have to be developed. Since the number of diffusing atoms within the slabs is exceedingly small, the experimental measurement of boundary concentration profiles is difficult. Therefore recourse has been made to accumulation methods, where atoms which have diffused along a grain boundary are collected and counted. For example, solute atoms have been deposited on one surface of a thin film specimen possessing a columnar grain structure. They were diffused through the film along the grain boundaries and accumulated on the reverse surface. Negligible crystal diffusion occurred in those conditions. Diffusion through the film specimen was therefore controlled by the rate of grain-boundary diffusion. The diffusion length is measured, and D is easily calculated by the law $L = \sqrt{(2Dt)}$, after annealings at fixed times and temperatures. This approach has been followed by **Sundaresan et al. (1983)**, **Hwang et al. (1980)**.

According to **Sundaresan et al. (1983)**, aluminum is an impurity which has a grain-boundary diffusion coefficient which is higher than its bulk coefficient. This can have further consequences. Grain-boundary diffusion will be preferred and the the number of defects will be reduced in the bulk as the impurities will move to the grain boundaries. The experiments performed in this work show that if aluminum is diffused at 800°C for 1 hour in silicon, it will not produce significant grain-boundary passivation. However, the diffusion length can be in the order of 50 μm .

Surprisingly high grain-boundary diffusion coefficients have been found by **Hwang et al. (1980)**. The activation energy was measured to be 2.64 eV and D_0 was extrapolated at $1.3 \times 10^7 \text{ cm}^2\text{s}^{-1}$ after experiments in the temperature range 350-425°C, after 16-hours-long annealings. Higher temperatures can increase this value further, but at such temperatures bulk diffusion dominates.

1.4.4 Diffusion-driven transformations

Generally a transformation which occurs at constant temperature can be described with the help of Avrami's law:

$$y = 1 - \exp(-kt)^n$$

with

y = percentage of phase transformed

k = constant, depending on temperature and produced phase

t = time

n = constant dependent on the transformation type

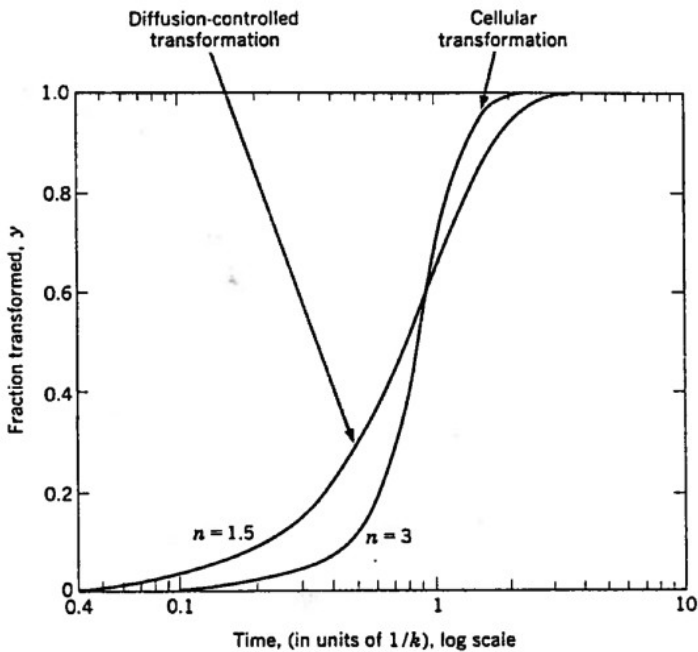


Fig. 14: Avrami's law dependency of a transformation occurring at constant temperature (Bjorndal, 1990)

The law describes how fast a transformation goes. In Figure 14 it can be noticed that the transformation starts with slow speed, but it increases rapidly

until the most has been transformed. Then the reaction takes speed again. The slope of the curve depends on n . An alloy can go from a phase to another by different ways, which can be mainly resumed into two main groups.

In the first group the crystal is totally reconstructed, either in the crystallographic or in the chemical composition. This can only happen with diffusion and/or when atoms move through the grain boundaries between the old and the new phase. The transformation often occurs between passages through metastable phases. An important group are the transformations with precipitation of particles. This is typical when the transformation is not complete. Some of the produced phase is left after the transition, by then it will have a slightly different chemical composition. The new phase nucleates and grows with diffusion of atoms over relatively long distances. The majority of the diffusion controlled transformation implies also that all the original phase is converted to one (or more) new phases (for example, what happens in an eutectoid transformation). One of the new phases nucleates first, often at the grain boundaries, dislocations or defects. Eventually other phases forms easily around the first ones, often at their borders.

The second group includes all those reactions which do not involve diffusion. Only some alloys can undergo this kind of transformation, especially at quenching conditions. Otherwise diffusion based reactions will get time to happen. When a material is rapidly quenched, there is a strong chemical driving force which can cause the material to have an unexpected structure. The stresses which appear can make the atoms migrate for distance smaller than the lattice parameter, causing it to change. These transformation are extremely rapid. An example can be the martensite structure reaction in martensitic steels.

1.5 Transformations driven by surface energy

Interfaces between two phases or two portions of matter usually are not precise and mathematically defined surfaces. They are rather inhomogeneous

regions within which the transition between the two adjoining parts occurs. General relationships can be derived for an overall system consisting of an interface and two adjoining bulk phases, α and β .

A fundamental thermodynamic quantity which is involved in this problem is the interface free energy γ . In a bi-crystal system, γ is equal to the increase in the Gibbs free energy of the entire system (G) per unit increase in the interface area (A), when temperature (T), pressure (p) and moles (n_i) of the components are held constant:

$$\gamma = \left(\frac{dG}{dA} \right)_{T, p, n_i}$$

SI-units of γ are Jm^{-2} . The area of the interface can increase by just moving atoms from the bulk to it. Interfaces have a higher energy than the bulk. However, it can be so low that the surface energy value will always be positive. If the atoms are less densely packed, γ tends to decrease with increasing temperature.

1.5.1 Splitting and coarsening of particles

The problem we are considering now is the change in geometry of a single particle in a two-component, two-phase system (the matrix and the particle are respectively made of the phases α and β). It is assumed that the particle composition consists of pure component β , and that the two phases are immiscible. An elongated particle is exposed to a high temperature, and undergoes a melting transition. Its surface energy will therefore have an influence on the final shape. The equilibrium conditions are $\mu_B^\alpha = \mu_B^\beta$ or, in terms of pressure, $p^\beta - p^\alpha = \frac{2\gamma}{r}$.

If the system is at equilibrium, the concentration reaches the equilibrium value, and the pressure is the same in the two phases. On the other hand, if the concentration is different from the equilibrium concentration, we have two

different pressures in the two phases. Minimum pressure difference equals equilibrium state. It is easy to notice that equilibrium conditions are reached when the radius of the particle is as small and uniform as possible. The only shape in nature which encounters both the conditions is the spherical one. As a consequence, an elongated particle will start to split in multiple particles. The contact angle with the α phase will determine the extent of the splitting transformation: the higher the angle, the more hydrophobic the surfaces, the higher and more similar the number of particles generated. The starting minor axis will be the radius of the generated particles. A particle distribution of spherical droplets is therefore generated at short times.

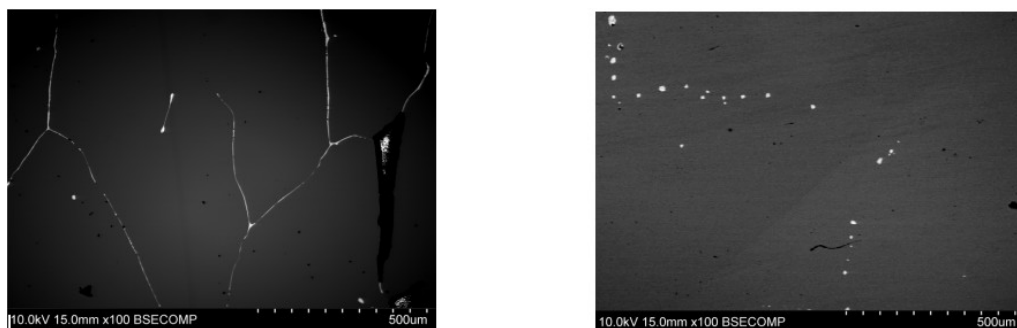


Fig. 15: Splitting transformation involving melting of grain boundary particles: before (left) and after (right) the melting. Pictures from this work's experiments

At longer times, another transformation called Ostwald ripening (or coarsening) is occurring. If the starting system presents many particles and a high temperature, “small” particles tend to disappear, whereas “big” ones tend to increase their size progressively. At any time, a distribution of particles sizes will exist. It can be quantified by defining a particle-size distribution function, $f(r,t)$ whose units are L^{-4} . Total interfacial energy reduction provides the driving force for coarsening of a particle distribution. When a particulate phase is embedded in a matrix of a second phase, flux from smaller to larger particles causes the average particle size to increase as the total interfacial energy decreases. The particles compete for absorbing the solute, and the larger

particles have the advantage.

1.5.2 Diffusion-controlled coarsening

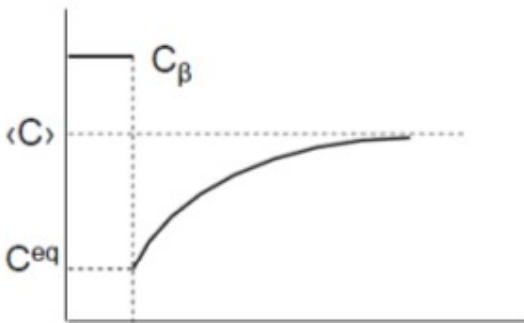


Fig. 16: Diffusion control coarsening, concentration profile

A pure and constant composition of the solute on the left of the vertical dashed line in Figure 16 represents the interface. The assumption is that at the interface there is always the equilibrium concentration in the matrix. In this system there are many different particles and an average equilibrium concentration. We have a concentration gradient,

which will cause diffusion. We can solve the problem with the diffusion equations, assuming a diffusion-control mechanism.

The general situation is depicted in Figure 17. The concentration difference, $\langle C \rangle - C_{eq}$, is spent to support diffusion in the matrix under diffusion control. During diffusion-limited coarsening, the interfaces surrounding the particles maintain the concentrations of the solute in the phase close to the equilibrium values. The rate of coarsening is then controlled by the rate at which diffusion takes place between the particles. Because particles of different sizes are distributed throughout the bulk randomly, developing an exact model that couples diffusion to particle size evolution is challenging. However, a mean-field approximation is reasonable. Diffusion near a spherical sink has a short transient and a steady state characterized by steep concentration gradients near the surface. The particles act as independent sinks in contact with a mean-field of concentration $\langle C \rangle$. Each particle is surrounded by a spherically symmetric diffusion field (fluxes are indicated by arrows).

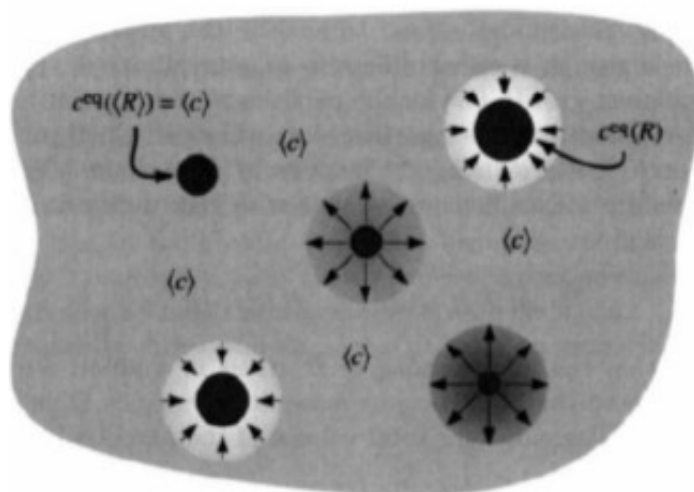


Fig. 17: Diffusion controlled coarsening

In the mean-field approximation, each particle develops a spherically symmetric diffusion field with the same boundary condition fixed by the mean concentration, $\langle C \rangle = C^{eq}(\langle r \rangle)$. This mean concentration is lower than the equilibrium concentration of the smallest particles and higher than the largest particles' equilibrium concentration. Therefore, the large particles tend to grow and the small particles to shrink. A particle with size $\langle r \rangle$ will not have any flux. Its dimensions will be fixed and its concentration will be C^{eq} .

The diffusion problem can be solved for a particle distribution, instead of a single particle. A random distribution of particles and recognize that the general situation around any particle is the same, so we divide our system in many spherical cells, each one surrounding a particle. If we do this, we will have a small overlap between the spheres, so it is not correct. From a practical point of view these overlapping regions have no relevant effect. The result will be similar to Figures 16 and 17, and explained by the law

$$\frac{dr}{dt} \propto \left(\frac{1}{\langle r \rangle} - \frac{1}{r} \right)$$

Therefore when $r < \langle r \rangle$, $\frac{dr}{dt}$ is negative, and when $r > \langle r \rangle$, $\frac{dr}{dt}$ is positive. The behavior of any particular particle depends only on its size compared to the mean particle size.

A steady-state (normalized) distribution function is approached asymptotically as $t \rightarrow \infty$. This steady-state distribution, illustrated in Figure 18, is approached by all initial distributions. During annealing, the mean particle size increases with time, and the number of particles decreases because the smallest particles disappear as the larger ones grow.

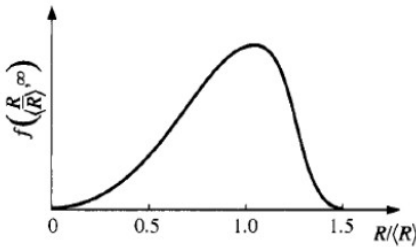


Fig. 18: Final steady-state normalized PSD for diffusion-limited coarsening

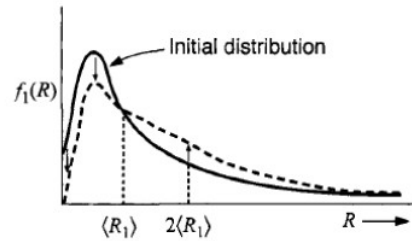


Fig. 19: Initial distribution changing with time according to the growth law expressed in the previous equation. The smallest particles disappear with relatively large shrinkage rates, so the lower end of the distribution collapses to zero

1.5.3 Wetting on grain boundaries

Ignoring any misfit strain energy, the optimum nucleus shape should be that which minimizes the total interfacial free energy. The optimum shape for an incoherent grain-boundary nucleus will consequently be two joined spherical caps as shown in Figure 20, with θ given by a force balance:

$$\gamma_{\alpha\alpha} - 2\gamma_{\alpha\beta} \cos \theta = 0 \quad \rightarrow \quad \cos \theta = \frac{\gamma_{\alpha\alpha}}{2\gamma_{\alpha\beta}}$$

assuming $\gamma_{\alpha\beta}$ is isotropic and equal for both grains. The excess free energy

associated with the nucleus will be given by

$$\Delta G = -V\Delta G_v + A_{\alpha\beta}\gamma_{\alpha\beta} - A_{\alpha\alpha}\gamma_{\alpha\alpha}$$

where V is the volume of the nucleus, $A_{\alpha\beta}$ is the area of the interface α/β with energy $\gamma_{\alpha\beta}$, and $A_{\alpha\alpha}$ the area of the α/α grain boundary with free energy $\gamma_{\alpha\alpha}$ destroyed during the process. When the derivative of ΔG with respect to r is equal to zero, the critical radius of the spherical precipitates can be found. This size will not depend by the grain boundary dimensions. The corresponding activation energy will be proportional to θ .

$$r^{*c} = \frac{2\gamma_{\alpha\beta}}{\Delta G_v} \rightarrow \Delta G_{het}^{*c} \propto S(\theta) \quad S(\theta) = \frac{1}{2}(2 + \cos\theta)(1 - \cos\theta)^2$$

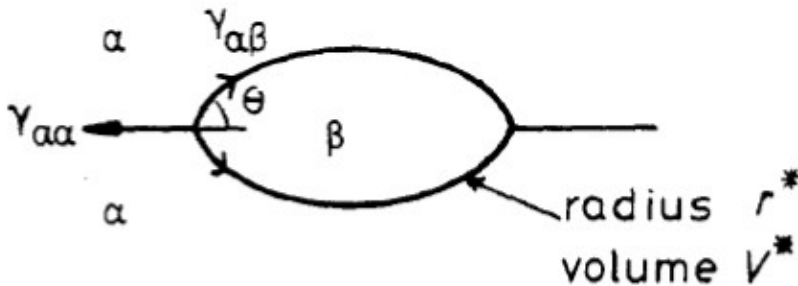


Fig. 20: Thermodynamic model of precipitation of particles at the grain boundary. r^* and V^* are the critical nucleus radius and volume

$S(\theta)$ is called *shape factor*. The ability of a grain boundary to reduce ΔG_{het} depends on $\cos \theta$, which varies according to the nucleation site configuration. If there are grain edges or corners, θ will be reduced, and the particle will follow closely the grain boundary profile. High-angle grain boundaries are particularly effective nucleation sites for precipitates with high $\gamma_{\alpha\beta}$. The effect of the microstructure is shown in Figure 21.

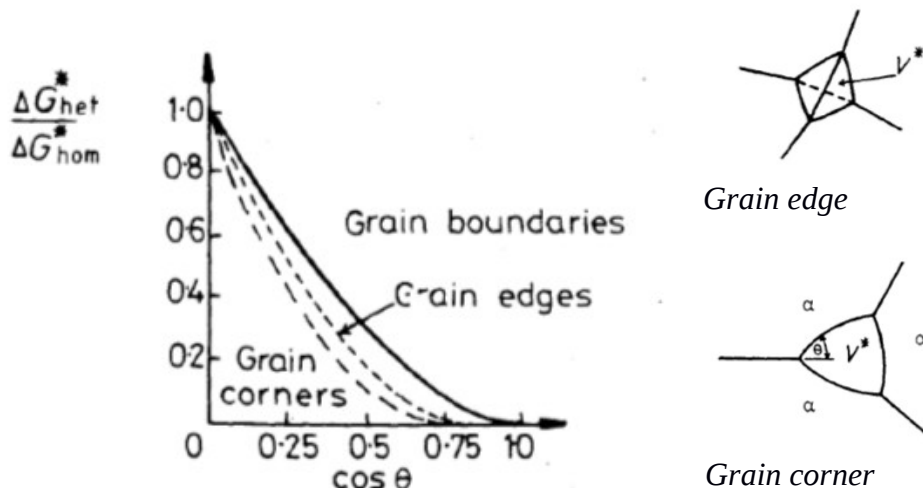


Fig. 21: Effect of theta on the activation energy for grain boundary nucleation relative to homogeneous nucleation. Different configuration of the grain boundary can also have an effect (Cahn, 1956)

Although these equations are only approximate and were derived for a planar interface, the conclusions are not significantly altered by allowing curved interfaces. Thus, it can be shown that any linear dimension of a spheroidal precipitate increases as \sqrt{Dt} provided all interfaces migrate under volume diffusion control.

1.6 Annealing of Si-alloys

Few studies have been performed concerning the geometrical characterization of the intermetallics in metallurgical grade silicon by controlling the thermal history. Size, shape and composition of the intermetallics are determined by the total impurity level, the solidification and the cooling process. The distribution of intermetallic phases is influenced by cooling rate and grain size of the starting material (Margaria, 1994).

Because of solidification fronts moving, the temperature is changing through time at different positions in the cast. Rong has analyzed the temperature development during the solidification and the effect of an annealing on microstructure during solidification of a thick cast (**Rong, 1992**). Figure 22 shows a typical temperature profile for a silicon ingot cast in an iron mold with casting thickness of 16.5 cm. The thermocouple closest to the top surface (T1) increases first to the melting point of silicon and decreases after some minutes. The temperature flattens out at about 1250°C. The thermocouple close to the solidification boundary (T2) increases to the melting point, and stays at this temperature for about 25 minutes. The thermocouple above the solidification boundary (T3) starts to drop from the melting point very quickly. T3 continuously drops after a few minutes, in contrast to thermocouple T1.

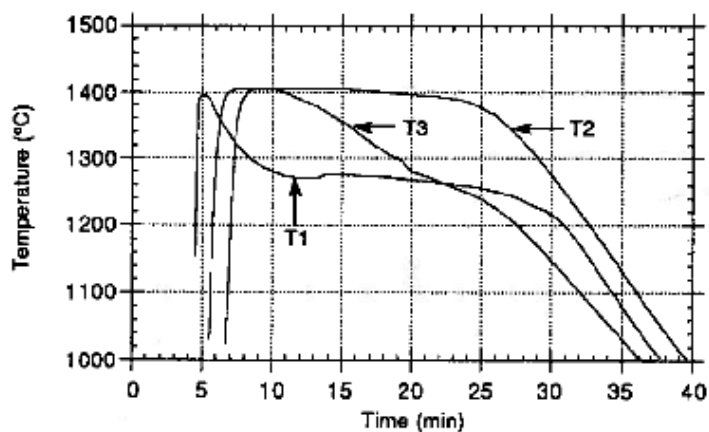


Fig. 22: Annealing at different positions in the cast. (1), (2) and (3) correspond respectively to top, solidification boundary and area above the solidification boundary (**Rong, 1992**).

M.F. Møll has also analyzed the temperature dependence in further detail (Møll, 2014). Figure 23 illustrates that the temperature profile in the cast is changing at a fixed time according to the cast thickness position. The material is cooled fast initially at the top and at the bottom due to the high temperature gradient with the surroundings. Once solidified, silicon will cool with a slower rate. The opposite is observed for positions close to the area where the solidifying fronts meet. The initial cooling is slow because of the partial release of latent heat inside the cast, while the subsequent cooling was rapid. The thicker the cast, the longer time is available to rearrange the microstructure before solidification.

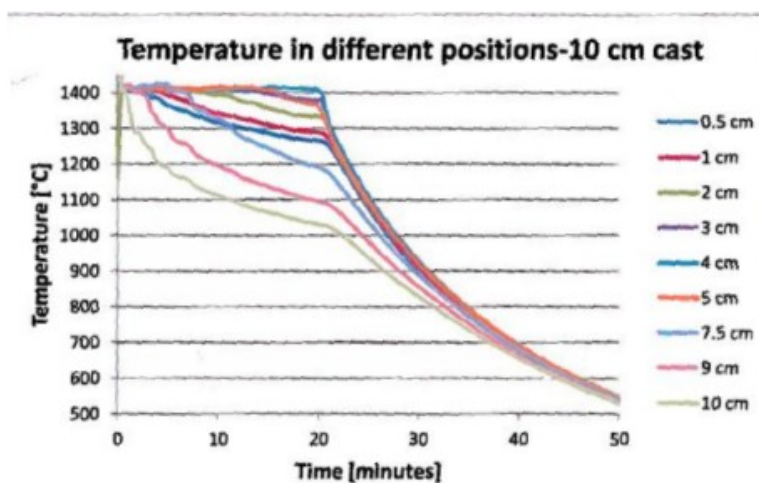


Fig. 23: Temperature in different positions from the bottom of a 10 cm modelled cast. Close to the top or the bottom, the temperature decreases fast initially, but slow subsequently due to the heat from the other areas that must be transported through the surfaces (Møll, 2014)

The annealing after solidification can have effect on structure as another experiment performed by Rong (1992) shows. A silicon sample was melted and solidified at known rate. A second sample was melted and held at 1200°C for 12 hours. At this temperature only the intermetallic particles were still in liquid state, whereas the silicon matrix was solid already. Figure 23 shows the

different microstructures of the two samples. The grain size is approximately equal in both, showing that annealing at 1200°C does not affect the grain size. However, the shapes of the intermetallic phases (white areas) have changed. In the first sample the inclusions are found as elongated bands on the grain boundary. After annealing they appear as round particles. It seems that the elongated particles have split due to surface energy effects. The temperature required to get an annealing effect is estimated to be above the melting point of the intermetallics, between 900 and 1200°C. A decrease in surface energy is thought to be the main driving force for this microstructural change.

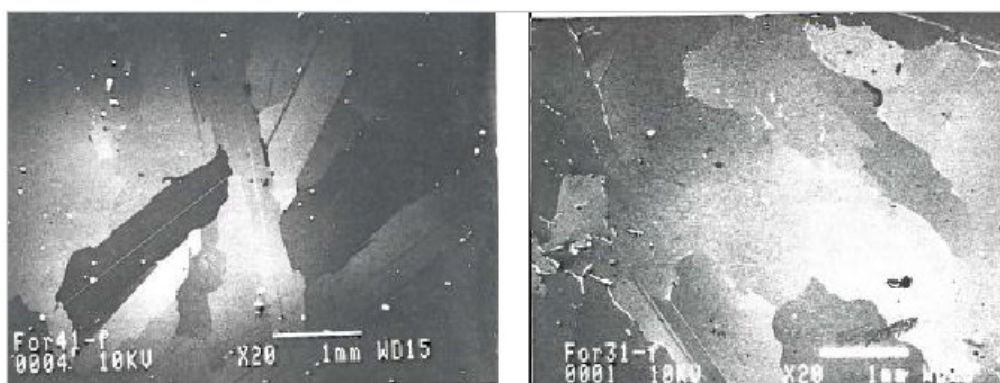


Fig. 24: Differences in microstructure between annealed (left) and original (right) sample (Rong, 1992)

Chung has studied the effect of retrograde solubility in MG-Si during fractional melting (Chung, 2010). Retrograde solubility occurs when the solubility of some impurities in silicon increase above the eutectic temperature (Weber, 1983). This phenomenon requires the intermetallics to be in liquid state. Different annealings at different times and temperatures can influence this phenomenon. A MG-Si sample with 99% purity was chosen. It contained impurities of Ti, Fe and Al. In cases 1, 2 and 3, the temperature rose to 700, 1240 and 1410°C respectively. The heating rate was fixed at 2°C/min. All the samples were quenched after being maintained at their respective temperatures

for 6 hours.

Impurities seem to be distributed randomly in the reference sample, and in case 1 there was not much difference from the initial conditions. At 700°C the temperature is too low and no compound turns to liquid state. Only solid diffusion might be occurring, but the time might be too slow to notice radical changes. In case 2 impurities begin to coalesce at grain boundaries, pores and cracks, and accumulated more at the edges than in the center of the sample. In case 3 and 4, the impurities are also observed at the edges. This means that the impurity rich liquid in the center moves to the edge of the sample at 1410°C through the network of pores and grain boundaries.

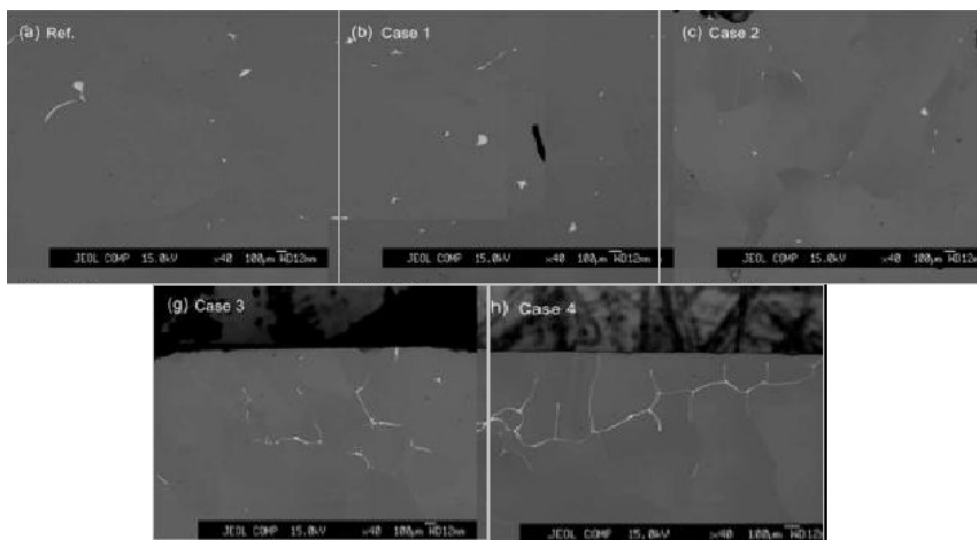


Fig. 25: Cross-sectional images of an as-received reference sample and various heat treated samples (Chung, 2010)

1.7 Binary and ternary systems in MG-Si

Iron, aluminum, calcium and titanium are the most common impurities in MG-Si. This part will focus on the binary and ternary systems between these elements, in order to understand which phases are present in the intermetallics. Trace elements are also common, but they will not be a part of this work,

therefore they will not be considered.

1.7.1 Fe-Si system: the FeSi_2 phase transformation

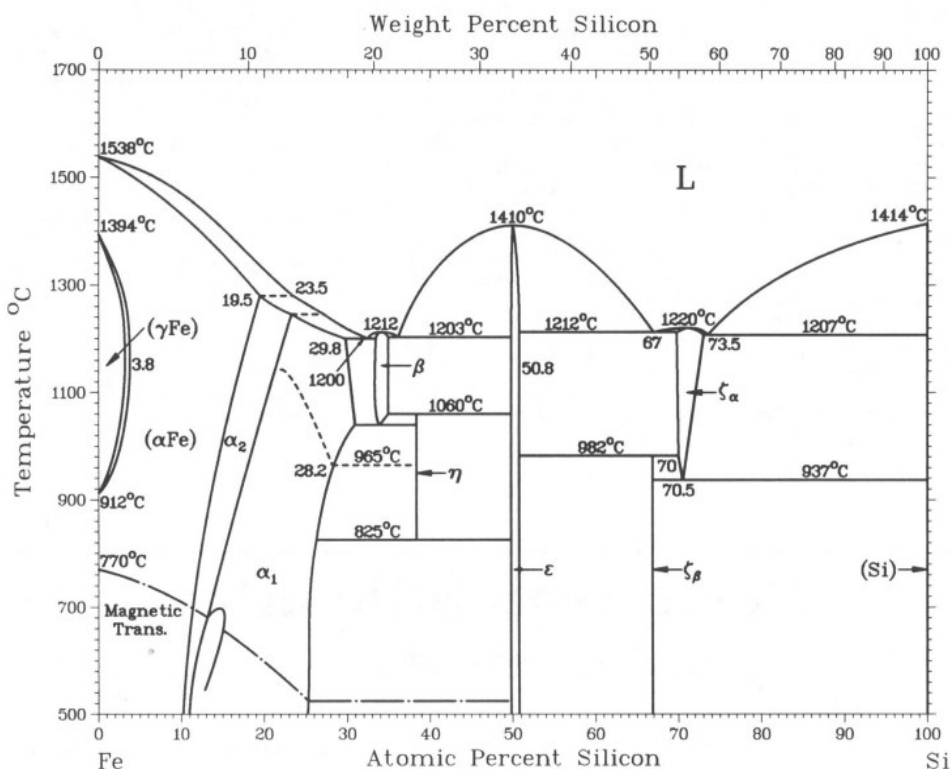


Fig. 26: Fe-Si phase diagram (Massalski, 1990). The phase ζ_α and ζ_β correspond respectively to HT- FeSi_2 and LT- FeSi_2

Since the high-Si content area is concerned, high amounts of FeSi_2 are expected to be found in MG-Si. This phase will have two different microstructures according to the temperature (HT- FeSi_2 and LT- FeSi_2 , corresponding respectively to high temperature and low temperature). If the cooling rate to room temperature is fast enough, the HT- FeSi_2 structure can be obtained (see Figure 26). In industrial solidification, the cooling rate is fast enough for this transformation not to happen completely. It has been shown by a previous work that the transition from HT- FeSi_2 to LT- FeSi_2 takes 3 hours at

700°C in order to be complete (**de Huff, 1969**). Besides this, **Anglezio et al. (1990)** have reported that the HT-FeSi₂ is stabilized by aluminium substitution in the structure. According to **Margaria (1996)** the maximum content of Al can be up to 8% at. in order to improve the stability in a efficient way.

Boomgard (1972) has performed a study about the transformation from HT to LT-FeSi₂. He states that the transformation occurs in two steps:

- *Step 1: HT-FeSi₂ → LT-FeSi₂ (Si)*: in the first step, the transformation occurs with a change in volume, and starts at defects such as cracks or grain boundaries. If these are not present, the reaction will be hindered.

- *Step 2: LT-FeSi₂ (Si) → LT-FeSi₂ (Si) + Si*: As soon as step 1 has started, an interface will begin to move through the material. Behind the interface there will be a supersaturated LT-phase where silicon precipitates. As a matter of fact, the HT-phase structure has a high vacancy concentration in the Fe lattice. Its structural formula can be closer to FeSi_{2.3} rather than to FeSi₂. Therefore silicon precipitates can be noticed during this transition, especially at the grain boundaries. This reaction has no defined starting or ending point, i.e. it occurs together with step 1.

Tveit (1988) has enquired this transformation in a 75% Si-alloy. It was noticed a marked slowing on the cooling rate under slow cooling of a sample when the temperature was between 950 and 910°C. It can be suggested that an exothermic reaction would occur. SEM and X-ray analysis confirmed on the other hand that no LT-phase had been produced. Besides, cracks were noticed in the material. This was thought to be caused by step 1 described by Boomgard's theory. The defects are introduced in the material before step 2 has started and LT-phase has formed. The transition also starts on grain boundaries and defects. Small Si-precipitates are noticed in the LT-phase matrix. Around the LT-phase, HT-phase can be noticed.

Bjorndal (1990) has inquired into the phase transformation from HT-FeSi₂ to LT-FeSi₂ by performing heat treatments on 58% and 75% FeSi. The produced

material was undercooled HT-phase. X-ray diffraction was carried on at temperature ranges between 600°C and 890°C. Subsequently a time-temperature plot was traced. The results show that the transformation occurs at around 600°C after more or less 1 hour. Higher temperatures make the transformation start later. From 710° C up the transformation starts almost immediately.

The electron microscope experiments showed that heat treatment at 740°C leads almost all the sample to be transformed into a LT-phase with many silicon particles precipitating. They are formed within 1 hour of heat treatment at 740°C. LT-phase contains many thin stripes. It was not discovered which compound they correspond to, but it is thought that they can be a mixture of the two phases. If heated at 600°C, a completely different structure is formed. After 12 hours two sharply separated phases appear but no silicon precipitates are observed. LT-phase begins to be formed in the area with high amounts of primary silicon.

It was found that three samples heated to 600, 740 and 850°C in the same way show two different transformations. The sample heated at 600°C does not show any Si-precipitates in the transformed phase, but it looks homogeneous. It can be possible that Si particles were generated, but maybe not seen at the magnification chosen for the analysis at the microscope. The particle size is hence decided by the heat treatment temperature. Another hypothesis is that step 1 from Boomgard's theory is actually happening, but step 2 is not. In step 1, a supersaturated phase is created, and subsequently Si precipitates out from them during step 2. The precipitation step goes slower at lower temperatures. From the other experiments performed at different times and temperatures, it was seen that step 2 is strongly dependent on temperature. At 740°C a LT-phase matrix contains Si precipitates. The structure corresponds to the one found by Tveit, in Figure 27.

In the end, in the sample treated at 850°C for 24 hours the transformation occurs only in a well-defined area. However, if the treatment was shorter than

16 hours, no transformation would occur. The Si-precipitates are 5 times bigger than the sample treated at 740°C. Si precipitates are larger since higher temperature enhances higher mobility of atoms in the material.

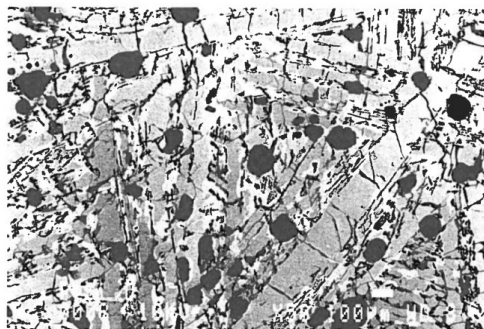


Fig. 27: Sample of a 58% ferro-silicon treated at 600°C for 12 h. HT-FeSi₂ is grey, LT-FeSi₂ is white and Si-precipitates are black (Bjorndal, 1990)

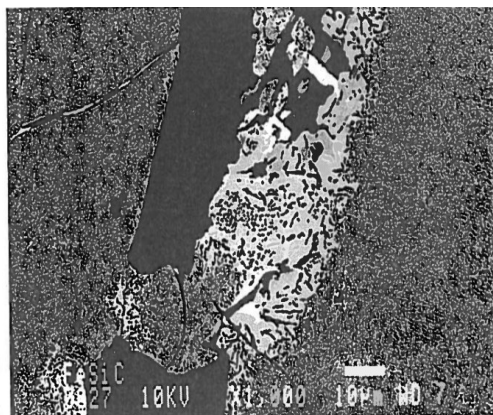


Fig. 28: Sample heat treated at 740°C for 13 hours. Magnification at 1000x (Bjorndal, 1990)

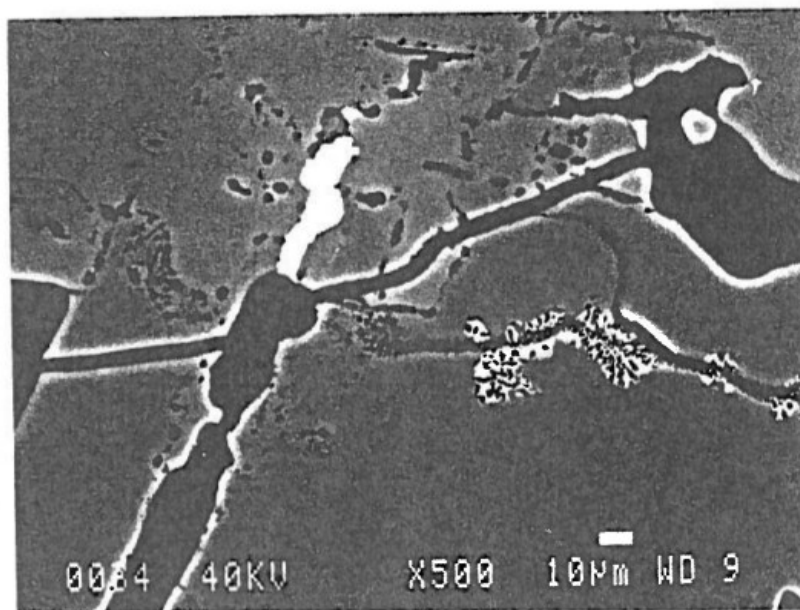


Fig. 29: Transformation in the 75% Si-alloy: The sample was heated at 850°C for 24 hours (Tveit, 1988)

1.7.2 Common intermetallics in MG-Si

The Al-Si phase diagram shows a simple eutectic system. At high percentages of silicon, Al is solubilized to a limited amount. However, silicon has solubility in Al phases.

As far as Ca-Si and Ti-Si systems are concerned, CaSi_2 and TiSi_2 are the only phases relevant for MG-Si. TiSi_2 will not be formed in high amounts, since the ternary phase FeSi_2Ti forms easier. This is the only phase coming from the ternary system Fe-Si-Ti.

In the Al-Si-Fe system **Anglezio et al. (1990)** reported Al_3FeSi_2 and $\text{Al}_8\text{Fe}_5\text{Si}_7$ as the most common phases in MG-Si, which corresponds to the Si-rich area. Other works by **Schei et al. (1992)**, **Rong (1992)** and **Margaria et al. (1992)** confirmed the same results. In the end, for the quaternary system Al-Ca-Fe-Si the phase of highest importance is $\text{Al}_6\text{CaFe}_4\text{Si}_8$. The most frequent intermetallics in silicon are resumed in Table 5, together with their densities. Silicon density is also reported.

Table 5: Density, composition and details of some of the intermetallics present in MG-Si, compared to silicon

Compound (solid state)	Density (g/cm³)	%at. composition (Sørheim,1994)	Comments (Rong,1992)
FeSi₂	4.74 (Barin, 1989)	Fe – Si – Al 28 – 65 - 7	FeSi ₂ usually contains some Al, up to 10% mol. A decrease in Al content increases the silicon content, thus varying the stoichiometric formula up to FeSi _{2.4} (Al)
Al part (Eutectic Al-Si)	2.7 (Dons, 2009)	Al – Si 88 - 12	It can exist in materials with low Fe and Ca, and high Al.
TiFeSi₂	>5 (Dons, 2009)	Ti – Fe – Si – Al 23 – 22 – 52 - 3	In silicon materials all Ti is found in these phases. It often occurs as small rectangular particles in other phases. Al can be detected in small amounts. It is also possible to find TiSi ₂ , but in smaller quantities. Jo (2014) has performed a research about the mechanical properties of TiFeSi ₂ . Its work consisted in proposing a valid matrix compound for lithiation of dispersed silicon nanoparticles. The lithiation process forms the phase Li ₂₁ Si ₈ which causes relevant volume expansion of the nanoparticles. The matrix releases the stress caused by the volume change on the nanoparticles and acts as a solid support. It was concluded that TiFeSi ₂ is more rigid than silicon.
TiSi₂	3.85 (Dons, 2009)	Ti – Si 33 – 67	
Al₈Fe₅Si₇	≈3.8 (Dons, 2009)	Al – Fe – Si 36 – 23 - 41	It may be that Si is replaced by Al in the FeSi _{2.4} (Al) and that a range of compositions exists for this phase
Al₃FeSi₂	≈3.6 (Dons, 2009)	Al – Fe – Si 52 – 15 - 33	

$\text{Al}_6\text{CaFe}_4\text{Si}_8$	$\approx 4-5$ (Dons, 2009)	Al – Ca – Fe – Si 30 – 4.4 – 21 – 44.6	This is the only quaternary phase except for phases containing minor elements. It is very common when the Ca/Al ratio is very low. There is not a complete agreement about stoichiometry of this compound. It was reported by Schüssler (1989) to be $\text{Al}_4\text{CaFe}_4\text{Si}_6$ and by Dons (2009) to be $\text{CaAl}_5\text{Fe}_7\text{Si}_8$.
CaAl_2Si_2	$\approx 2.6-2.7$ (Dons, 2009)	Al – Ca – Si 39 – 20.6 – 39.3	CaAl_2Si_2 is common when Ca and Al are present in high amounts (>0.1% wt.). It can react with FeSi_2 by annealing at 900°C, producing $\text{Al}_6\text{CaFe}_4\text{Si}_8$, CaSi_2 and Si, according to Margaria (1994)
Si	2.329 (Knacke, 1991)	-	-

1.8 Sistruc[®]

The PC-program SiStruc[®] was developed in 2009 (**Dons, 2009**). Its main purpose consists of calculating the composition, amount and melting ranges of intermetallic phases in silicon, given the weight percentages of Fe, Ca, Al, Ti, B and P. The program can also forecast which phases are developed during solidification of silicon with different impurity levels, and at which temperature they form. Thermal analysis, metallographic experiments and literature studies are performed on MG-Si at different compositions to develop the software. 30 “common” alloys have been inquired, and a phase diagram for the system Al-Ca-Fe-Ti-Si is estimated. The calculation developed in the program are based on directional solidification laws, such as Scheil equation, for the calculation of the composition of the solid:

$$C(s) = k C(liq) \quad \text{or} \quad C(s) = k C_0 (1 - f_s)^{(k-1)}$$

where $C(s)$ and $C(liq)$ are the compositions of the solid and the liquid phase

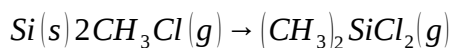
respectively, C_0 is the starting composition of the melt, f_s is the solid fraction (i.e. the “space coordinate” in the direction of the solidification front) and k is the distribution coefficient. k can depend on temperature. It is also possible to include back diffusion of alloying elements into the solid. The back diffusion coefficient have been estimated and inserted in the program from experimental results. The temperature must also be assumed to be constant at the solidification front. Through this program it can be understood that back diffusion might have an important role during solidification of certain elements, i.e. only Scheil equation itself cannot give enough information about the concentration profile in the cast. It is necessary to consider back diffusion for fast elements like Cu, but not for slow diffusing elements like Al and Ca.

Another part of the program can calculate bulk diffusion lengths at given time and temperature for common impurities in silicon (Ti, Fe, Al, Ca, B, P). According to SiStruc[®], the diffusion length for Ca and Al are estimated to be equal. The program is merely based on thermodynamics. Interaction between phases and other effects such as oxidation of elements, losses by evaporation and kinetics, are disregarded.

1.9 Parameters influencing microstructure in the MCS production process

1.9.1 Influence of the fluidized bed reactor and particle size distribution

According to the different application, silicone can require many different production steps to achieve the desired microstructure. One of the crucial process steps is the reaction between silicon and methyl-chloride to produce dimethyl-dichlorosilane, which is the first step of the so called *Direct process*. The main reaction occurring during this step is:



(Cu catalyst, 260 to 370°C)

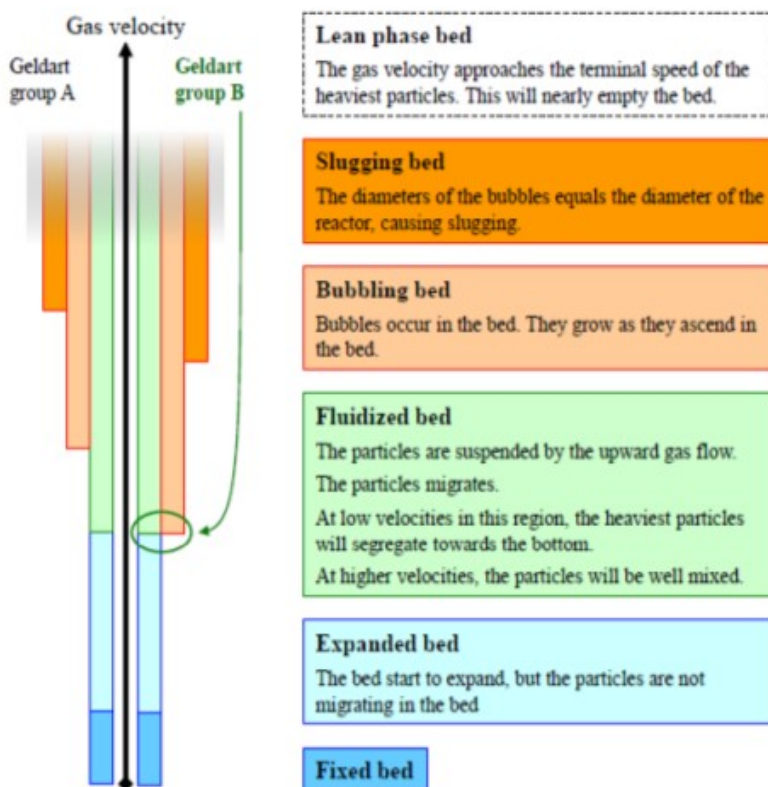


Fig. 30: Fluidization regimes and critical gas velocities for Geldart group A and B powders (Hoel, 2014)

The reaction expressed takes place in a fluidized bed reactor, and the different fluidization regimes are represented in Figure 30. A fluidized bed reactor is characteristic with the gas flow given by the design of the reactor, amount of gas added, pressure and temperature. These parameters give the characteristic cut size of the reactor, i.e. the maximum size below which a particle is removed from the reactor and does not react with the gas.

As far as the particle properties are concerned, the cut size is influenced by

size, shape and density. In order to have a deeper understanding of the behavior of a particle in a fluidized bed, mechanical models are developed. A particle undergoes its gravitational force and the drag force for the liquid. Both of them are a function of the diameter. However, when modeling, the particles are assumed to be spherical. This is not always the case, so an aerodynamic diameter has to be computed. Hence the necessity of investigating the distribution of the values of the aspect ratio comes as well. A narrower aspect ratio distribution in the particles can improve the precision of those models.

The higher density of the intermetallic phases (cfr. Table 4) will result into a smaller cut size, compared to silicon. Therefore if a particle is larger than the cut size, it will accumulate in the reactor. Since the intermetallic phases affect the reaction between silicon and methyl-chloride, accumulation of unreacted impurities is associated with poor reactivity. Besides, if the fluidized bed reactor is operated below a critical gas velocity, the bed will present segregation at the bottom. The dimethyl-dichlorosilane synthesis is exothermic, so an evenly distributed heat transfer rate is needed to avoid local variations. The precipitates isolate the chamber, thus lowering the temperature control of the reaction and increasing the bed temperature. This might have undesired effect on the reaction rate, including a decreased selectivity and damages to the reactor walls. The fluidized bed reactor will fail its main objective, i.e. to distribute heat from exothermic reactions in the most even way as possible.

In the majority of the cases, metallurgical grade silicon creates a Geldart group B powder (**Hoel, 2014**) when ground, i.e. the fluidization minimal speed matches with the minimal bubbling speed. Bubbles are created as soon as the powder is fluidized. This allows good mixing of the particles and the catalyst, but it can affect the reaction rate, since bubbles will entrap some of the methyl-chloride needed for the reaction and reduce the contact time between reactants.

1.9.2 Influence of intermetallic phases

Dimethyl-dichlorosilane (MCS) is the main and preferred product, but by-products can form. Two important parameters for the Direct process are reactivity and selectivity. They are defined respectively as the amount of MCS produced for tonne of silicon, and the amount of MCS with respect to the amount of the other by-products. Besides the reactor conditions, the content and type of intermetallic phases can have an influence on the Direct process. Since there are several parameters affecting it, it is difficult to give specifications about an optimal silicon microstructure associated with optimal reactor conditions. There have been several attempts to describe the effect of the different intermetallic phases, but there is no complete consensus so far about it. The system considered is really complex, as many parameters interfere with reactivity and selectivity of the reaction. For this reason, experiments are difficult to reproduce, and results between different authors are difficult to compare.

Sørheim (1994) has inquired the influence of the intermetallic phases on the production of methyl-chlorosilanes. To study the effect of each intermetallic phase, silicon materials with one or two intermetallic phases each were synthesized. Al, Ca, Fe and Ti were added to molten Si in controlled amounts. Wafers of these materials were exposed to CuCl and CH₃Cl to determine the degree of reaction. A CuCl-ZnO-SnO₂ catalyst was used. Only the phases which react with CuCl and CH₃Cl affect reactivity and selectivity. The work by Sørheim suggests to silicon producers to increase the reactivity by having high amounts of Al₈Fe₅Si₇, Al₃FeSi₂ and Al₂CaSi₂, and to have low content of CaSi₂ and Al₂CaSi₂ in order to enhance the highest selectivity. FeSi₂ and TiFeSi₂ do not have effects on these two factors, but their content should also be as low as possible in order to avoid accumulation in the reactor.

Laroze et al. (1992) and **Margaria et al. (1990)** have followed a similar approach to inquire into this topic. Intermetallic phases have been added to

silicon materials. Reactivity and selectivity test were performed in a stirred bed laboratory reactor. **Schüssler et al. (1989)** has used a similar method to Margaria and Laroze. **Rong (1992)** has also observed that an increase in Al content can increase the reactivity. It is important to notice that the quaternary phases $\text{Al}_6\text{CaFe}_4\text{Si}_8$ and $\text{Al}_4\text{CaFe}_4\text{Si}_6$ are the only phases which increase selectivity. The results from these works have been gathered in Table 6.

Table 6: Effect on reactivity and selectivity of the intermetallic phases (M=Margaria et al., 1992; L= Laroze et al., S= Schüssler et al.).

Phase	Reference	Reactivity		Selectivity	
		Reference	Sørheim	Reference	Sørheim
FeSi_2	M	÷	0	÷	0
CaSi_2	M	+	0	÷	÷÷
FeSi_2Ti	M	÷	0	÷	0
$\text{Al}_8\text{Fe}_5\text{Si}_7$	L	+	++	÷	÷
Al_2CaSi_2	L,M	++	+++	÷÷	÷÷
$\text{Al}_6\text{CaFe}_4\text{Si}_8$	L,M	0	÷	+	++
Al_3FeSi_2	S	++	n.p.	0	n.p.
$\text{Al}_4\text{CaFe}_4\text{Si}_6$	S	÷	n.p.	+	n.p.

1.10 Description of the case of study

Composition, concentration and type of shape of the intermetallics in MG-Si are a key aspect in silicones production. The composition of the intermetallics is affected by the purity of the raw material, as well as by the refining and casting processes (**Bernardis, 2012**). The raw material composition and the furnace electrode composition sets the percentages of Fe and Ti, whereas Ca and Al content can be corrected through ladle refining. The casting technique used influences the shape and size distribution in the cast profile. To have the best size and shape distribution, and in order to avoid accumulation in the fluidized bed reactor, the shape of the intermetallics can be characterized by controlling

the thermal history of the solidification of silicon. For example, in industry several ingots are often moved from the mold and stored on top of each other. This will retain the heat for a longer time and could have an effect on the microstructure of the intermetallic phases.

In this case of study, samples from a MG-Si thin cast will undergo different thermal histories and casting conditions to investigate the solidification and the geometrical parameters of the intermetallics at room temperature, as well as eventual changes in composition.

In the first part, the thermal history will be considered. Silicon will be either heat treated without melting, or melted and solidified, by different thermal histories. In the second part, the effect on the phase composition will be inquired. In the end, a relation between the variation in phase composition and expected effects on MCS production for each phase will be presented. The software SiStruc[®] will predict the phases and confirm that industrial solidification is not happening at equilibrium conditions. An hypothesis about the mechanisms of the transformation can be made by looking at literature and results from previous works.

2 SHAPE CHARACTERIZATION

2.1 EXPERIMENTAL

2.1.1 Thermal history experiments

MG-Si samples were collected from a thin cast produced at the Elkem silicon production plant in Salten. Pairs of samples which share one surface were cut from the thin cast. The dimensions of each sample were of 10x10xthickness mm, with thickness varying between 30 and 45 mm. One of the samples from each pair was not treated at all, in order to be kept as reference. The other sample from the pair was heated in the LHT 04/18 furnace, available at the Metallurgy department at NTNU. Heating rates and cooling rates were constant for all the treatments performed. These two samples will be respectively called *untreated* and *treated* samples from now on.

Some of the material produced at Salten underwent a different thermal history. In this case the annealing consisted of three steps, as shown in Figure 31. About 250 g of silicon were crushed manually to a lump size of 2-3 cm diameter and heated up to 1450°C in a carbon mold with a heating rate of 30°C/min. This temperature was maintained for 2 hours, in order to melt the material. Afterwards the lid of the furnace was opened and the sample was cooled down to the desired annealing temperature. The cooling rate for this step was measured to be 30°C/min to 1200°C and 35°C/min to 1000°C. Once the annealing temperature has been reached steadily in the furnace, the lid was closed again and maintained for the desired time. In the end, the furnace was opened to cool down the mold as fast as possible. Cooling rates up to 20°C/min have been reached in this way. Heating rates and cooling rates were constant for these treatments as well. Samples with this thermal history have been called *annealed*.

The carbon crucible dimensions were respectively 10 cm diameter and 12 cm

in height. The bottom of the mold is spherical-dome-shaped, with an height of 5 cm. The thickness of each cast varied between 3 and 4 cm from the bottom point. In order to compare the effect of the different annealings between each other, a reference sample was cast. Its thermal history consisted in melting silicon at 1450°C for 2 hours, followed by air cooling to room temperature. It will be now on referred as **reference molten** sample. A sample was withdrawn from this cast and heat treated according to the first way exposed, i.e. without the melting step. This sample will be called **remolten treated**.

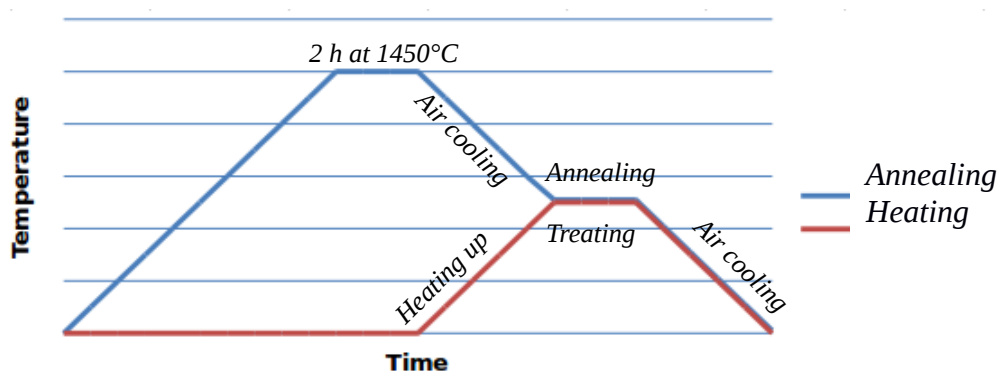


Fig. 31: Schematic representation of the two thermal histories chosen

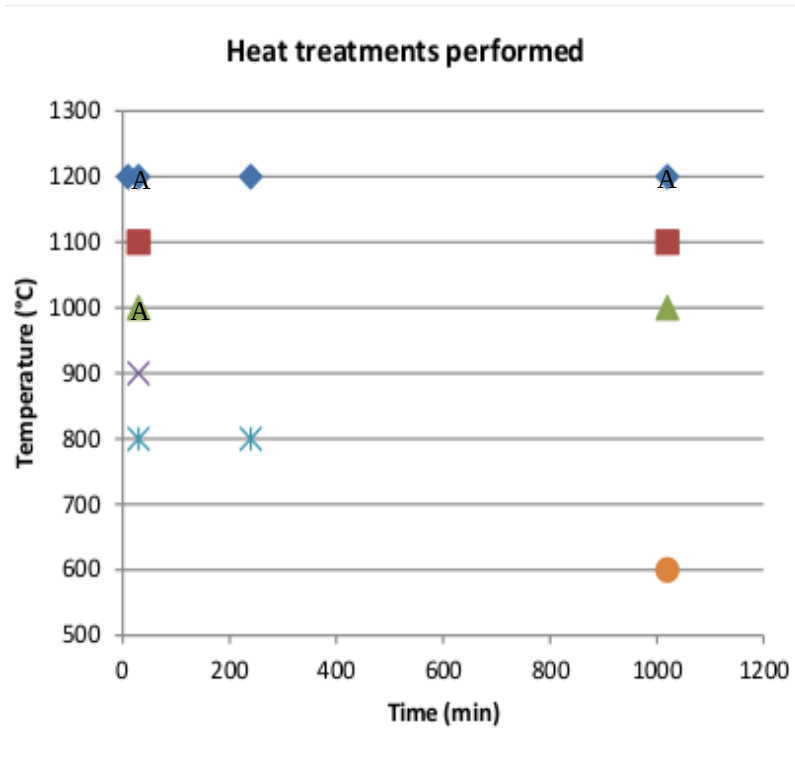


Fig. 32: Heat treatments performed. Annealings have also been performed in the points marked with A

2.1.2 SEM analysis and geometrical parameters data collection

For metallographic analysis, the samples were cast in epoxy and mechanically ground using SiC paper in the order 120, 320, 500, 1200, 2400, and subsequently polished with DP-Mol 3 μ m and DP-Nap 1 μ m polishing discs. Back-scattered electrons images of the surface of interest were taken with a Hitachi SU-6000 FE-SEM. The working distance was set at 15 mm and the voltage at 10 kV. Every picture has an extension of 1.27x0.95 mm² at 100x magnification and a resolution of 2560x1920 pixel. The surface analyzed has an extension of 10xthickness mm².

Figure 33 shows how the surface was scanned. A thickness coordinate step of

2.33 mm was set in order to avoid overlapping of the pictures. Three images have been captured from each thickness coordinate step, with a distance of 0.33 mm from each other. Some pictures have been slightly shifted in order to avoid cracks or local porosities.

The parameters related to each particle have been gathered by the software ImageJ® and analyzed with Libre Office Calc®. For resolution limitation reasons, particles smaller than $12.5\mu\text{m}^2$ (ca. 50 pixel/ptc) were disregarded.

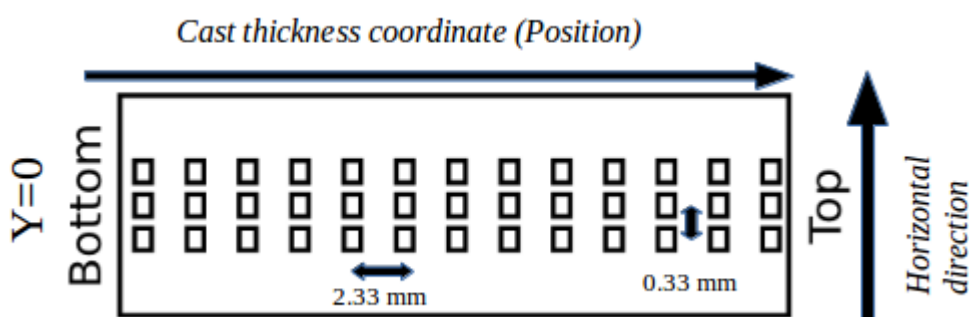


Fig. 33: Sample surface mapping on a 30 mm surface. Each small rectangle corresponds to a SEM image

2.2 RESULTS

2.2.1 Untreated sample

The microstructure of this sample was the one expected, as demonstrated from the previous experiments carried on at Elkem Salten (**Amundsen, 2013**). The solidification front meeting area is located between the bottom and the center for all the samples, as a confirmation of M.F. Møll's model. It can be recognized because of the high quantity of elongated particles at the grain boundaries. All the untreated samples show extended and elongated particles from 10 to 25 mm from the bottom of the cast, according to the sample's thickness. However, both at the top and at the bottom of the cast, the intermetallics have rounded shape and smaller extension (Figure 34).

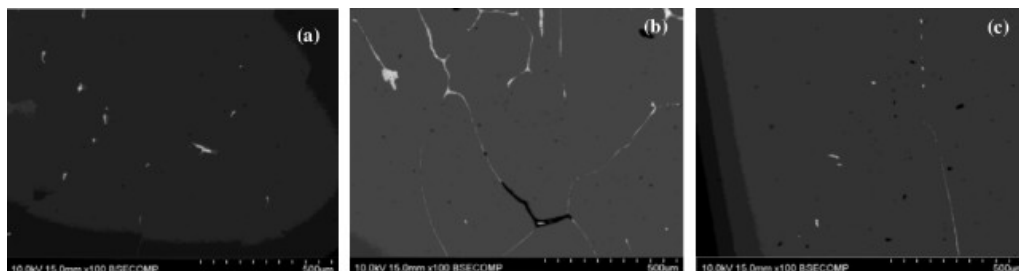


Fig. 34: Untreated sample microstructures at bottom (a), center (b) and top (c) of the cast

2.2.2 Heat treated samples

The pictures in Table 7 are collected from the area where the solidification front meet during the silicon thin casting, where the most relevant microstructural changes occur. As far as the top and the bottom of the sample are concerned, the only change noticed is an increase in size of the intermetallics particles. Relevant changes are noticed at temperatures over 800°C. The material is porous, and after the heat treatment the sample is covered of a thin layer of intermetallics and bubbles, as shown in Figure 35. After grinding and polishing the surface, it is possible to notice that the intermetallics create extended and round particles especially close to the pores.

The same considerations made so far can be done also for the remolten treated sample. The microstructure and the external appearance after the heat treatment are very close to the ones treated from the material as cast.



Fig. 35: Sample before (left) and after (right) a heat treatment at 1200°C for 17 hours. The green-blue layer on the surface is made of intermetallic compounds. The same happens for all the samples treated at a temperature over 800°C.

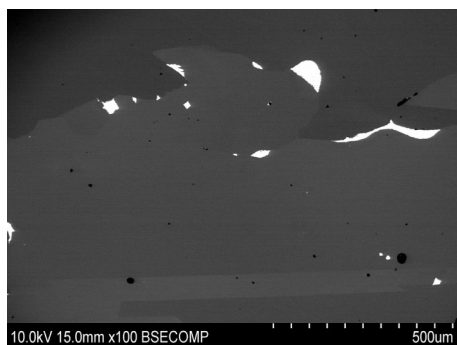
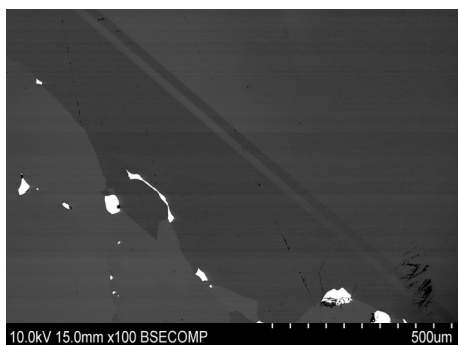




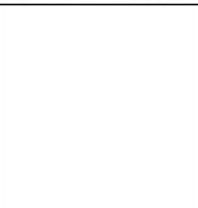
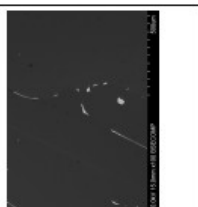

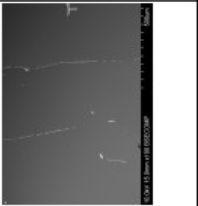
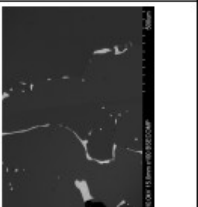
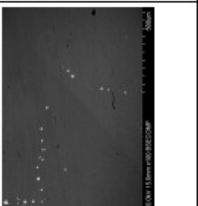
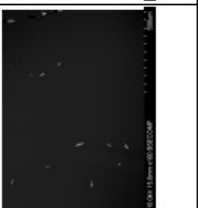
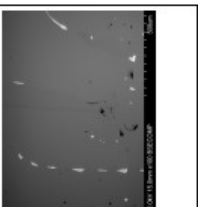

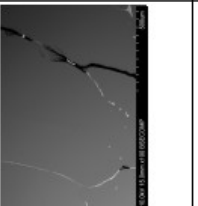



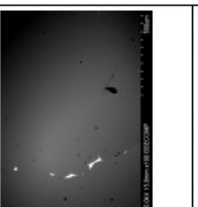
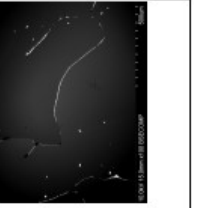
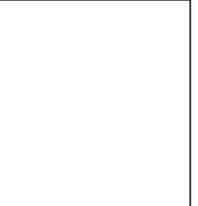
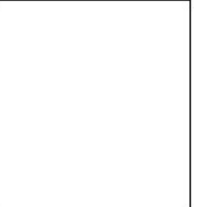
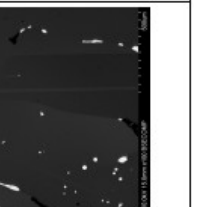
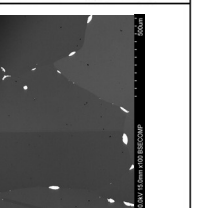
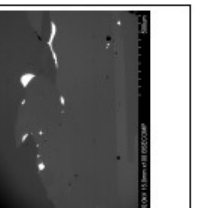


Fig. 36: Remolten treated sample (left) and heat treated sample microstructure (right). The pictures are taken respectively from the bottom and from the solidification front meeting point, which are the zones where the highest changes in microstructure occur compared to the respective reference

Table 7: Pictures from the solidification front point of different heat treated samples

	600°C	800°C	900°C	1000°C	1100°C	1200°C
10 min						
30 min						
240 min						
1020 min						

2.2.3 Reference molten sample

Figure 37 shows the microstructure of the reference molten sample. The size and the number of the particles keep increasing towards the bottom, whereas their circularity has the opposite trend. The impurities are concentrated in the bottom of the sample. The microstructure changes from the untreated material, since the heat exchange occurs in different conditions, and the liquid phase is accumulated progressively towards the bottom. A layer of oxide was noticed at the top, as well as a layer of carbide at the lateral sides of the cast.

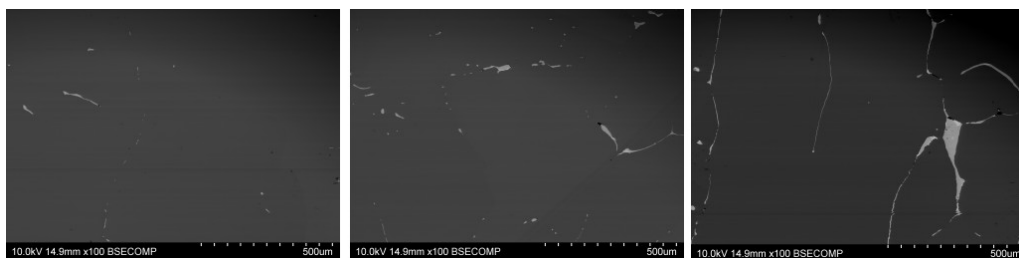


Fig. 37: Reference molten sample microstructure at top (a), center (b) and bottom (c) of the cast

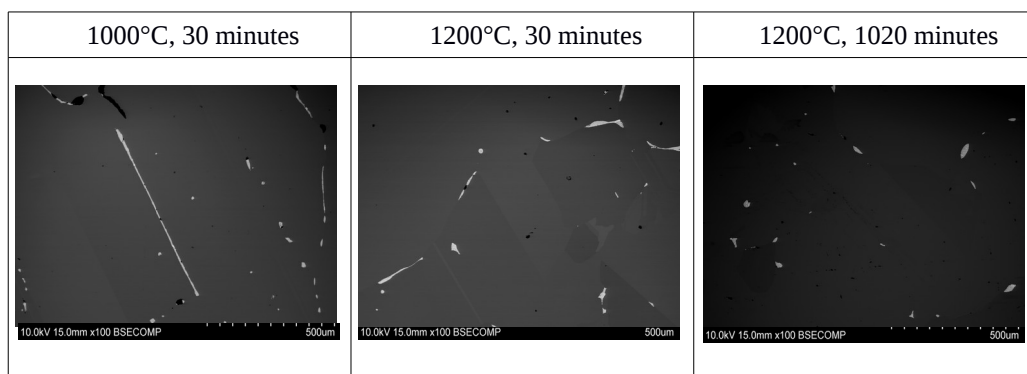
2.2.4 Annealed samples

The annealed sample also show rounded particles at the grain boundaries. The effects on the microstructure are the same as the heat treating, even if it seems that the effects of the annealing are less intense. At long times, a treated and an annealed sample have a very similar microstructure, independent from the starting material considered.

At short times, both elongated and round particles are noticed. The top of the annealed sample show an increase in dimension of the small round particles, compared to the reference molten sample. Table 8 shows the microstructure at the bottom of the three annealed experiments. The pictures should be compared to Figure 37c (bottom of reference molten sample). Thin elongated particles are

progressively replaced by round and large intermetallics. By increasing the treatment time and temperature, the intermetallics tend to reduce in number and increase their extension.

Table 8: Pictures from the bottom of the annealed samples



2.2.5 Cross-section temperature profile model

In order to verify that the modification of the microstructure was not just a surface effect, a simple 1-D model has been created and checked by another image analysis. The model assumes the environment temperature of the furnace to be 1100°C, and only radiation being present. A 25 mm thick sample is placed in the furnace and its temperature profile is analyzed as a function of time and thickness position in the first 10 minutes. Figure 38 shows the temperature profile in the sample as a function of time and different thickness position. As time passes by, the temperature difference between the surface and the core of the sample is decreasing, giving a negligible gap in temperature. Therefore the effects of the annealing in the core and the surface should be similar. In order to verify this, the sample treated at 1200°C for 30 minutes was cut through its cross section and scanned with the SEM. The results are available in *Appendix A*.

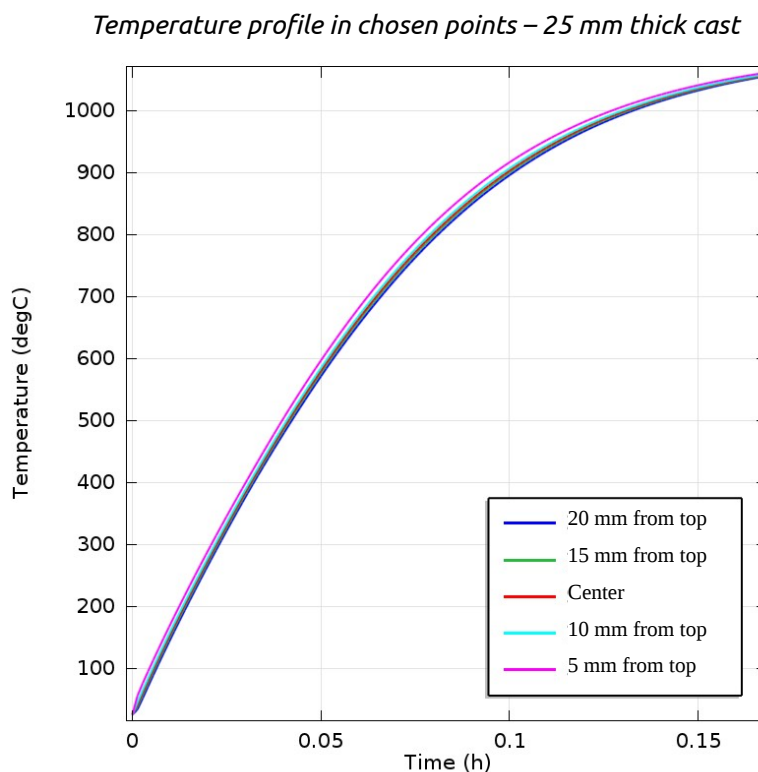


Fig. 38: Model of the temperature as a function of the cast depth coordinate and time (Garcia, 2014)

2.3 DISCUSSION

ImageJ[®] collected information about five relevant geometrical parameters, which will be the topics of this section. These factors are aspect ratio, average particle area, density of particles per μm^2 , major and minor axis of a particle. The parameters have been analyzed from two different points of view expressed in the two following paragraphs.

Firstly, the average values have been calculated respectively for the heated sample and their references, considering all the particles collected from all the pictures. Afterwards, the ratio between the value from the heated and the

untreated sample has been calculated and plotted as a function of time and temperature of the treatments applied. For the annealed samples, the results have been compared with the reference molten sample. This ratio can give an overview of the changes in the total sample. Particle size and aspect ratio distributions will be also investigated to have a deeper understanding of the changes. Standard deviations have also been collected in *Appendix A* and *B*.

This analysis cannot give a complete overview of which areas are mostly involved in microstructural transformations. The effects will also change according to the position in the cast, which show different starting microstructures. The changes of the five parameters as a function of the cast thickness coordinate are analyzed. Each slab's average value was calculated from the data collected from three pictures, and plotted as a function of position. The coordinate $Y=0$ corresponds to the bottom of the cast. *Appendix A* collects all the average values collected for the five parameters, as well as the standard deviation for area and aspect ratio. *Appendix D* collects all the position profiles for all the samples and the parameters.

2.3.1 Mechanism of transformation

The preliminary experiment has been performed on a sample heated at 1200°C for 30 minutes. Both the cross section and the external surface area have been analyzed. The situation between the two surface is comparable. The circularity of these particles reaches the same extent after the treatment. This means that at short times the intermetallics undergo the same microstructural changes both in the core and on the external surface. The average extension of a particle is smaller in the core, as well as the standard deviation. This is due to the movement of the intermetallics towards the edges of the sample during a heat treatment, also noticed by Chung. Hence the transformation happens in all the sample, and the final destination of the movement of the intermetallics through the network of grain boundaries is the external surface of the specimen. The number of particles is also decreased at the external surface because of this

phenomenon. Those particles which have reached a circular shape will subsequently try to decrease their surface energy by increasing their size.

It can be stated that the external surface can give a satisfactory view of the micro-structural transformations, and that the effects of the annealing are not just limited to the surface. This is also confirmed by the temperature profile model developed by Garcia, where the temperature difference between the core and the top sections is very small.

It is very important to underline that this effect is not present in the annealed samples, therefore the extent of the changes, especially for particle extension and number, are reduced. For all the heated samples, the thermal history starts a transformation which can be resumed into three steps:

1) *Melting*: elongated particles at the grain boundary turn into liquid state. By looking in detail at the pictures, the microstructure is essentially unaltered after treatments between 600 and 800°C. This might not be surprising. From the literature study, it is possible to see that the majority of the intermetallics is completely melted at temperatures over 850°C. Even if some compounds might have been liquid, their quantity might not have been relevant enough to be noticed by the changes in the parameters. However, changes in compositions and internal microstructure of the particles are expected in the annealed samples, and further inquired in chapter 3.

2) *Splitting*: particles in liquid state try to search for their own equilibrium shape. The surface energy effect forces the intermetallic to assume a circular droplet shape. The radius of the generated particles will be very close to the minor axis of the original particle. This step is usually confirmed by a reduction of average area, major axis and aspect ratio, and an increase in particle number. This transformation happens in very short times. All the samples treated above 850°C for 30 minutes or less show this behavior in the central part.

3) *Coarsening*: the round particles increase their size to further reduce the surface energy. Bigger particles will try to expand, whereas smaller particles will shrink. Besides, the material which has been flowing from the core tries to

gather and form new particles. This material flow is due most likely to wettability effects between the intermetallic particles and the silicon matrix. This phenomenon can be deduced by the acicular shape at the end of the particles, which follow the grain boundary profile and further lowers surface energy driving forces while the intermetallic is in liquid state. Coarsening is associated to an increase in area and minor axis, and a decrease in aspect ratio and particle number. It is noticed generally at longer times, but also at short times where small and round particles are present already. Hence splitting and coarsening transformation occur together, and sometimes it might be difficult to spot them without an accurate picture analysis.

2.3.2 Aspect ratio

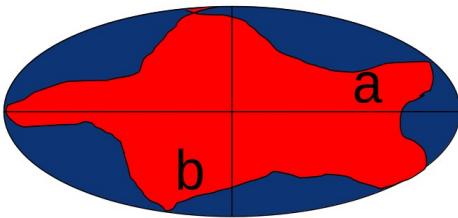


Fig. 39: Definition of aspect ratio: a and b are respectively the major and the minor axis of the ellipse (blue) circumscribed to a particle (red). Therefore $AR=b/a$

The aspect ratio (AR) of a particle is defined as the ratio between the major and the minor axis of the ellipse fitting a particle. This parameter gives an idea about the circularity and how far a shape is elongated. The average value is around 7 for the thin casting starting material, whereas it is about 5 for reference molten sample. Treated and annealed samples reach values down to 2.

Figure 40 and 41 resume temperature and time dependence overview of the aspect ratio variation. The changes in aspect ratio are relevant from 900°C up, also at short times. The point at 800°C has a high number of small particles which drastically reduce the circularity. However, the other parameters are not affected. This deviation can be due to differences in microstructure: a value between 90 and 110% was expected. In terms of circularity, the equilibrium of a particle is reached really early. However, some keep their elongated shape also after 10 or 30 minutes and do not have enough time to rearrange their structure.

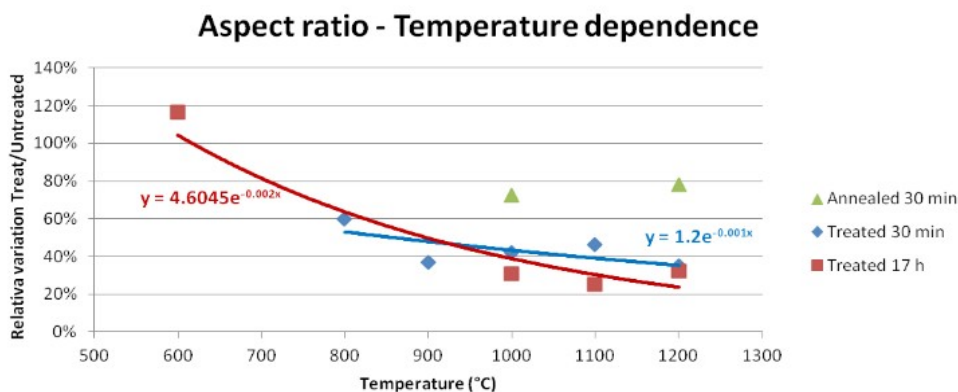


Fig. 40: Temperature dependences at different times of the relative variation for aspect ratio

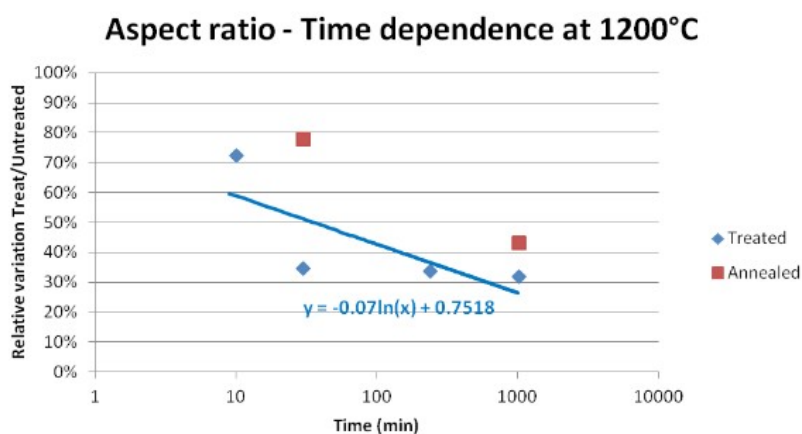


Fig. 41: Time dependence of relative variation of aspect ratio at 1200°C

The particles get more round all over the long time treated samples surface, and the aspect ratio nearly becomes constant and around 2 along the whole heated surface. The time dependence of the aspect ratio transformation follows a logarithmic trend. Splitting occurs after 10 minutes only, and at long times the ratios are very similar. The circularity distribution changes relevantly between samples showing splitting or coarsening. The time effect flattens the

distribution and makes it narrower. An higher number of particles with low aspect ratio is noticed in Figure 42. This is typical of a splitting transformation: more round particles are created from a single elongated one. On the other hand, a narrower distribution and a smaller number of particles is typical of a coarsening transformation (Figure 43).

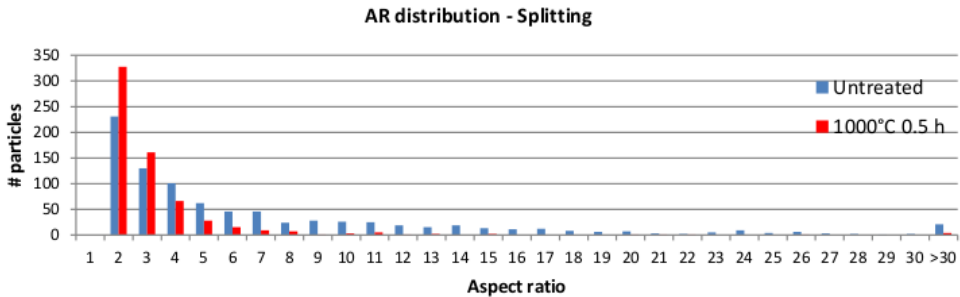


Fig. 42: Distribution of AR values in a sample treated for short times, which shows splitting (compared to the related untreated surface)

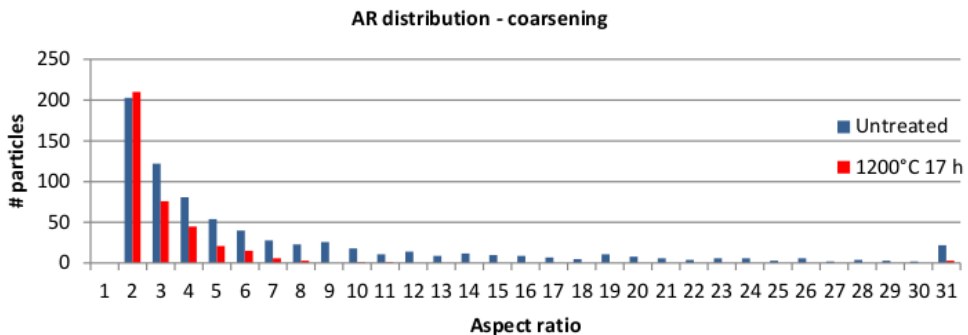


Fig. 43: Distribution of AR values in a treated sample showing coarsening (compared to the related untreated surface)

Figure 44 and 45 show the position trend for the samples showing splitting and coarsening of the particles. Although from both kinds of materials it is possible to see particles with aspect ratios up to 30, the average value in the

reference molten sample is lower because of the different solidification processes. The starting material is coming from a thin cast, where the solidification has two fronts merging towards each other. The reference molten sample undergoes a fast directional solidification, exchanging heat mainly by radiation from the top. The bottom stays warmer for longer time, as it is closer to the heating elements of the furnace. Since the impurities accumulate in the liquid phase, the most rounded particles in the material as cast are found at the top and bottom, where the solid is first formed. On the other hand, for the same reason the reference molten shows mostly elongated particles only at the bottom.

The treated and the annealed sample profile show two important features of the splitting transformation. In the treated sample, a peak with high aspect ratio is noticed close to the solidification front area. The other areas show many round particles. This is due to the kinetics of the transformation. Those particles which did not have enough time to split will keep their high aspect ratio value. The higher number of elongated particles is noticed in this area, both in the untreated and in the short-time-treated sample. In the other areas, smaller particles will find it easier to split, and the coarsening transformation might have started already after 30 minutes. The annealed sample confirms this theory as well. The particles are more uniform compared to the reference molten sample, and the aspect ratio still keeps a lower standard deviation.

When the coarsening transformation occurs, at long times the particles have constant aspect ratio all over the sample. Elongated particles which have resisted at such long times are very few, and the total number of particles is also reduced. Therefore deviations are more relevant in the green and purple graphs in Figure 45. The difference between heating up a sample or cooling it down from molten state is extremely small. It looks as if 17 hours are enough to establish an “equilibrium” situation. The quotation marks are written on purpose, since there are no more changes only as far as the circularity of the particles is concerned.

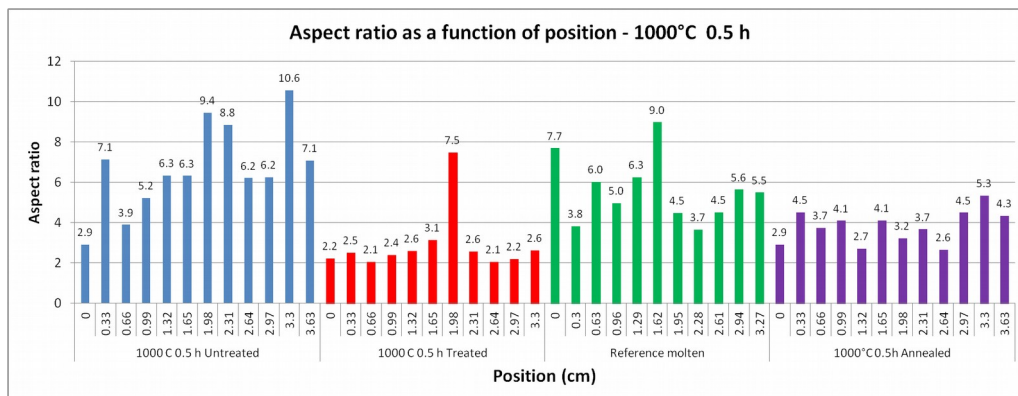


Fig. 44: Aspect ratio as a function of position in samples showing splitting, compared to the relative references

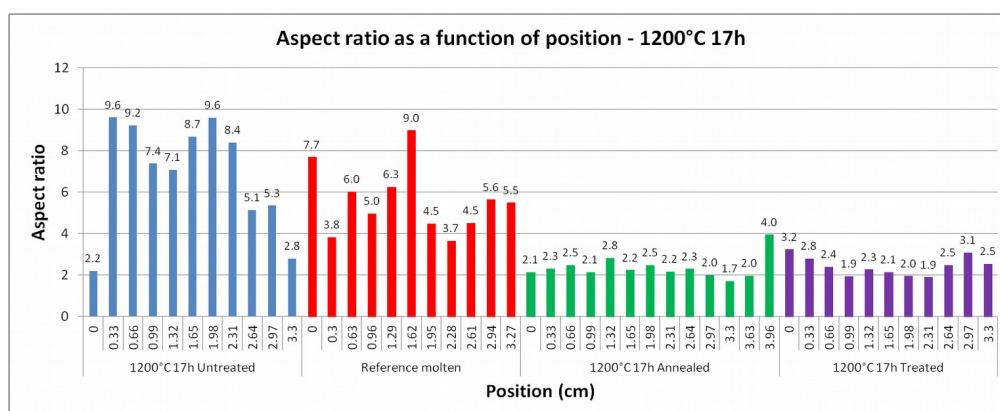


Fig. 45: Aspect ratio as a function of position of samples showing coarsening, compared to the relative references

2.3.3 Area

In this chapter, the parameter called *area* is defined as the average value of the extension of a single particle, considering all the particles found in the sample (or in a specified cast coordinate position). Eventual silicon precipitates, holes and scratches have been excluded during the analysis. This parameter is strictly related to the particle volume, therefore the discussion carried on here

could be valid for a tridimensional analysis as well.

The untreated sample has almost the same values of both area and standard deviation compared to the reference molten. Particle areas have values from 150 to 250 μm^2 in the untreated material, whereas the reference molten sample has an average of 218 μm^2 . Treated and annealed samples show an increase in the particle area up to an average of 400 μm^2 .

Between 900 to 1100°C the effect of the heat treatment is similar at short times. However, the global average value is not so distant from the untreated sample. The two mechanisms are challenging each other at short times, leaving the overall average area almost unvaried, but not locally. At 1200°C there is a

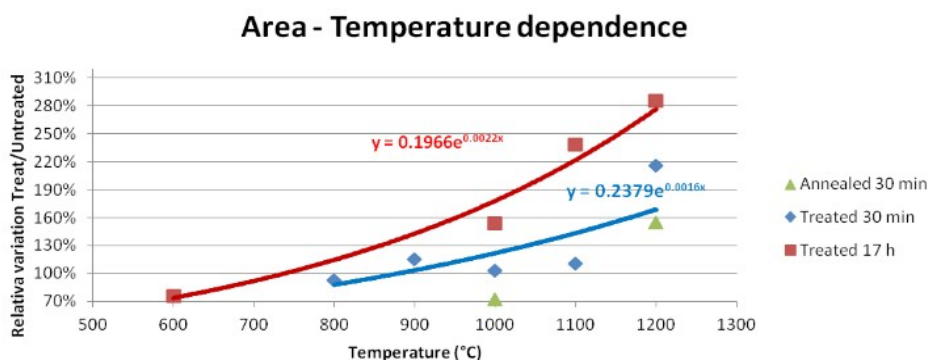


Fig. 46: Temperature dependences at different times of the relative variation for the average particle area

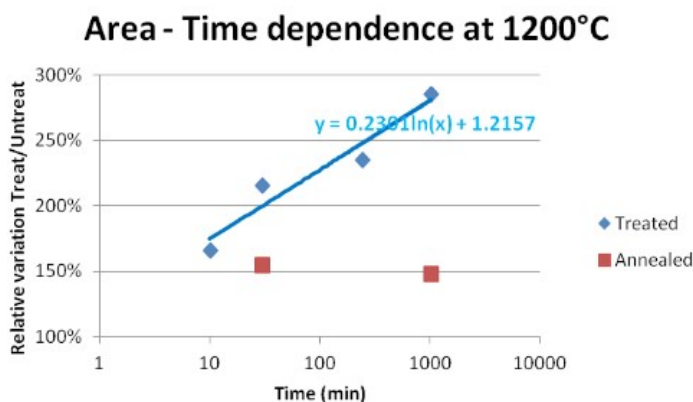


Fig. 47: Time dependence of relative variation of the average particle area at 1200°C

substantial increase of the area extension. This is due to the complete melting of FeSi_2 , as verified from literature (**Massalski, 1990**). FeSi_2 is also the intermetallic compound most present in MG-Si with the range of composition studied. A higher quantity of material will be involved in the transformation, hence its extent will be larger. In any case, the temperature affects the kinetics of the coarsening step.

The effect of the thermal history on the area is similar at both 4 hours and 17 hours of treatment. The particles increase their extension all over the profile up to an average value of $460 \mu\text{m}^2$. At fixed temperature, the time dependence is quite clear. Annealed samples show a lower increase in particle area because of the lower quantity of intermetallic particles present. As a matter of fact, some

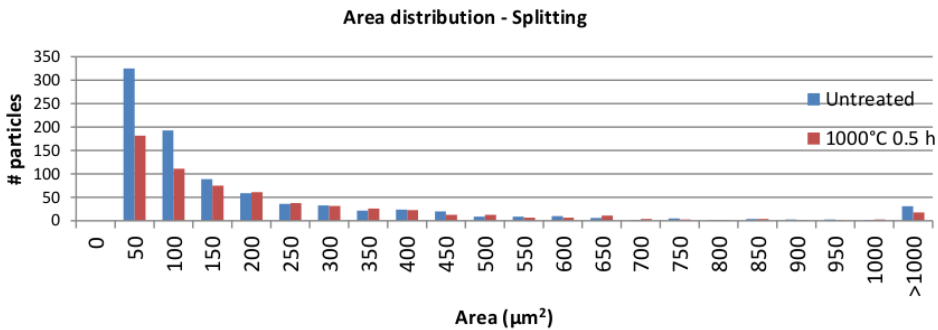


Fig. 48: Distribution of area values in a heat treated sample showing splitting (compared to the related untreated surface)

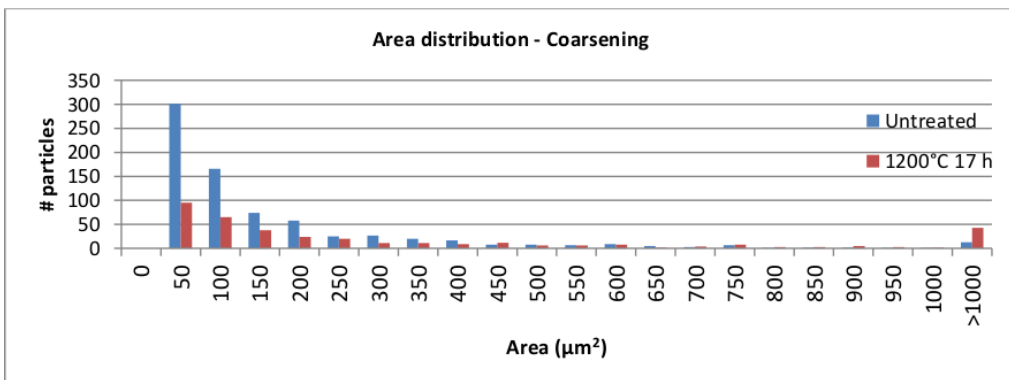


Fig. 49: Distribution of area values in a heat treated sample showing coarsening (compared to the related untreated surface)

impurities have been removed and transferred to the slag during the melting step, therefore the lower quantity of material present, the lower the coarsening rate.

The distribution becomes broader both after splitting and coarsening. Many particles with areas greater than $1000 \mu\text{m}^2$ are observed in every kind of sample. These are either particles which have experienced relevant coarsening (especially at long times), or liquid intermetallics coming to the surface from the core of the sample. Figure 48 shows that splitting creates a relatively high number of particles smaller than $250 \mu\text{m}^2$. Coarsening occurs at the same time, therefore other particles far from the solidification front meeting area can reach extensions up to $500\text{-}600 \mu\text{m}^2$. In Figure 49, the number of small particles decreases drastically compared to the reference. The material flowing through the network of pores and grain boundaries increases the intermetallic particles on the surface and creates particles larger than $1000\mu\text{m}^2$. These particles are more than 5 times in number compared to the ones in the untreated sample.

The small particles at the top and at the bottom of an untreated sample can start the coarsening step once treated for 30 minutes only (Figure 50), thus the area increases. The intermetallics in the center decrease their extension due to splitting. In the reference molten, the accumulation of the liquid phase at the bottom corresponds to a higher average particle extension. In the annealed sample, a drastic reduction of the particle area occurs all over the sample's section, already at short times. At the bottom, splitting happens to a high extent, whereas at the center and top the particles start to coarsen. Samples showing coarsening increase the area all over the sample, but keep the same position profile as their own reference materials. The annealed sample shows a peak at $Y=0.33$ and $Y=2.64$ due to a few particles larger than $3000 \mu\text{m}^2$.

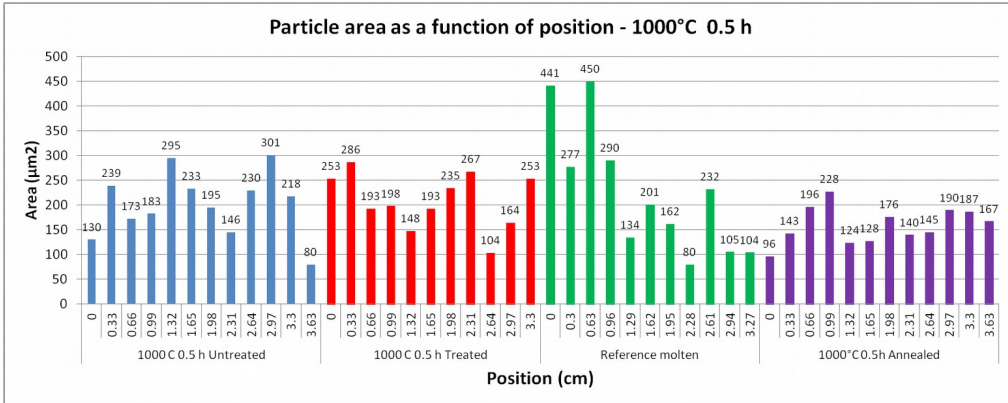


Fig. 50: Particle area as a function of position of samples showing splitting

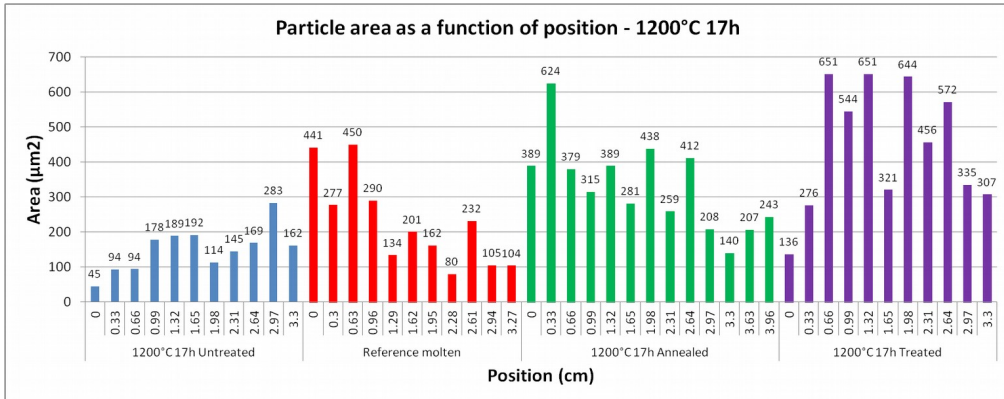


Fig. 51: Particle area as a function of position of samples showing coarsening

2.3.4 Number of particles

The thickness of the samples analyzed was not homogeneous. In order to compare the situations between the different samples, the particle density was considered. This parameter was calculated by counting all the particles observed and dividing by the total extension analysed, which was calculated by multiplying the image area with the total number of pictures.

The reference molten sample shows a slightly higher number of particles (29 per μm^2) compared to the thin cast (20 particles/ μm^2). Samples treated at short

times have an average lower particle density, despite the local increase of the particle number in the center and the competition between splitting and coarsening. Coarsening-behaving heat treatments can reduce particle density down to 9 particles/ μm^2 .

Increasing temperature and time accelerate the kinetics of both splitting and coarsening. Figure 52 and 53 resume the overview of the change of particle density as a function of time and temperature.

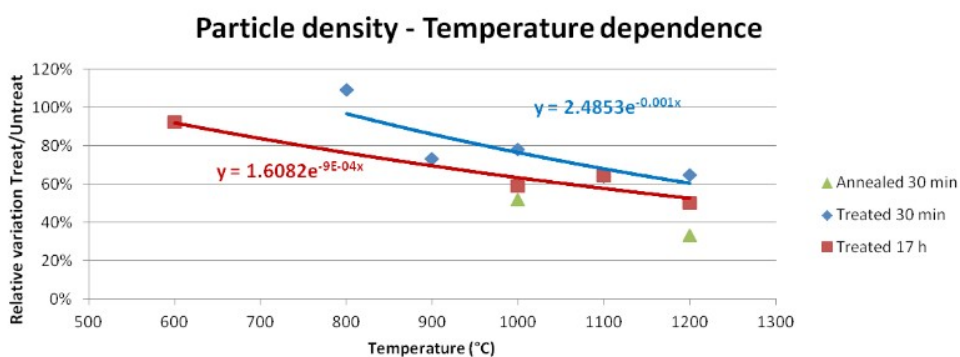


Fig. 52: Temperature dependences at different times of the relative variation for particle density

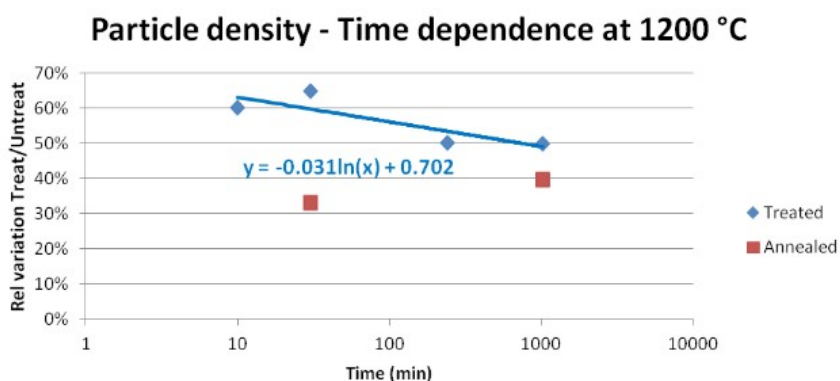


Fig. 53: Time dependence of relative variation of particle density at 1200°C

Despite coarsening tends to dominate over the majority of the section, in some areas of the sample heated at short times the particles number is

increasing. Figure 54 and 55 show the counted particles as a function of position. A higher number of particles is noticed where the liquid accumulates, i.e. at the center of the untreated and at the bottom of the reference molten. At short times, the center of the surface of the treated sample has experienced massive splitting at $Y=2.31$. At long times coarsening prevails and the number of particles decreases to a higher extent. Particles that have reached a round shape already will try to gather, and their number in the sample will decrease.

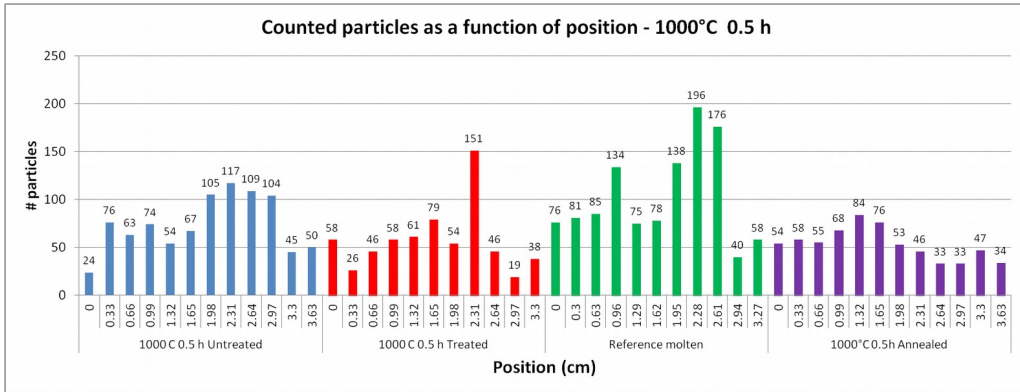


Fig. 54: Counted particles as a function of position in a sample showing splitting, compared to the relative references

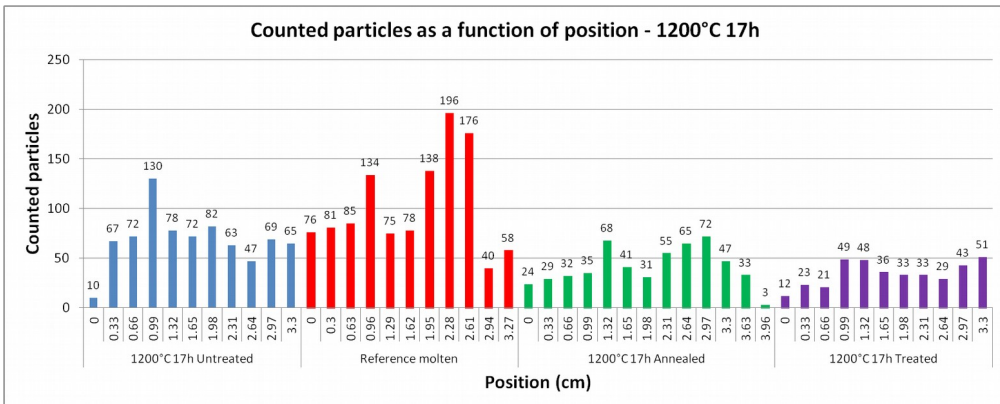


Fig. 55: Counted particles as a function of position of samples showing coarsening, compared to the relative references

2.3.5 Major and minor axis

The major and the minor axis of a particle are defined as the two axis of the ellipse fitting a particle (Figure 39). These two parameters give further details about the effectivity of the splitting and the coarsening transformation on a particle with elongated shape.

The major axis does not vary sharply as the other parameters analyzed so far. Values between 25 and 40 μm are obtained for all the samples considered, and relative variations are in the interval between 80 and 130%. The behavior of the time and temperature variation is also different compared to the other parameters. It can let us understand about the two steps of the mechanism of transformation. Temperature dependence follows a curve which looks close to a parabolic dependence rather than an exponential one. As a matter of fact, at short times the intermetallics will start to split, decreasing the average value down to 80%. Longer times will restore the initial major axis value thanks to the coarsening transformation. At 1000°C and 30 minutes splitting challenges with coarsening in the annealed sample, but at the same time at 1200°C the major axis is larger than in the reference molten sample. This might be due to deviations in microstructural starting differences, but it can be stated that coarsening is dominating thanks to the analysis of the other parameters.

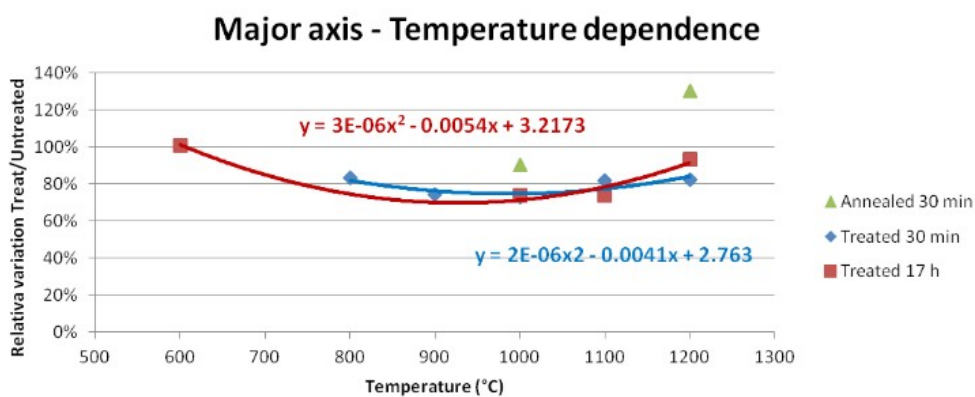


Fig. 56: Temperature dependences at different times of the relative variation for major axis

The time dependence curve (Figure 57) does not show a clear trend, unfortunately. It is possible anyway to notice an initial decrease followed by a sharp increase. The annealed samples show a higher increase in major axis due to the higher number of small particles seen in the reference molten sample.

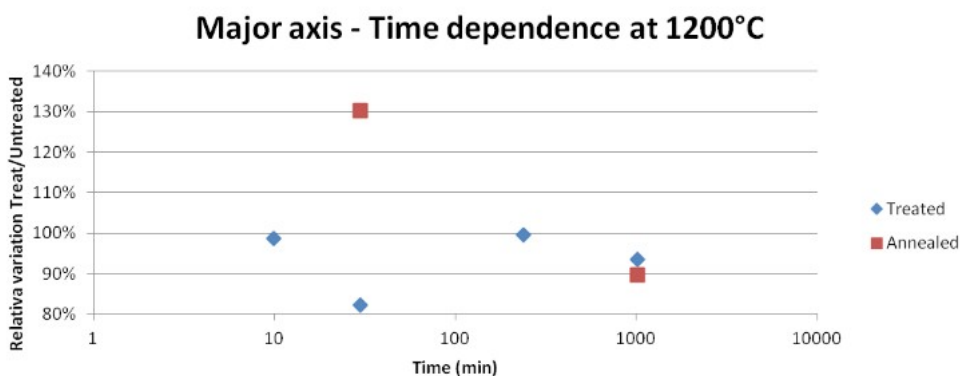


Fig. 57: Time dependence of relative variation of major axis at 1200°C

The position trend has to be analyzed carefully, as the value does not experience such relevant variations. The major axis follows the same dependence as the aspect ratio. A higher value of major axis corresponds to more elongated particles, as the high major axis of the untreated samples found in the center. The sharp decrease in the center of the sample treated at short times (Figure 58) is a clear clue of the splitting step occurred, as well as the increased major axis at the edges corresponds to coarsening. In Figure 59, major axis increases all over the sample, especially at the edges. The trend is very similar to the corresponding reference, independently from the thermal history applied.

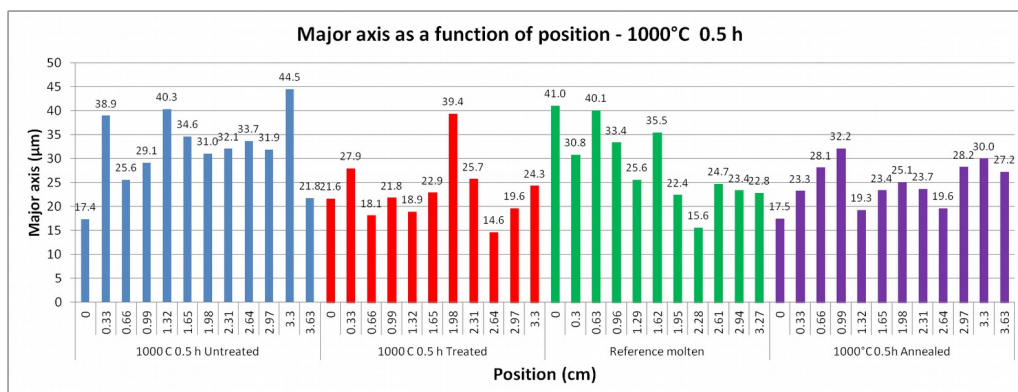


Fig. 58: Major axis as a function of position of samples showing splitting compared to their own reference

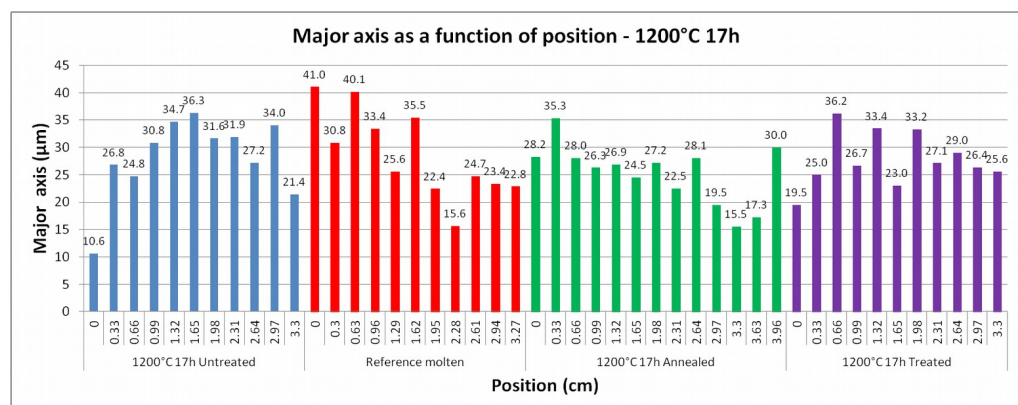


Fig. 59: Major axis as a function of position of samples showing coarsening compared to their own reference

The minor axis is not affected by the splitting step to a relevant extent. The particles generated from splitting have their minor axis almost unvaried. Eventual variations are due to the coarsening at the areas occupied by small and round particles. Therefore the minor axis can give a good overview of the kinetics of the coarsening step. Once liquid, the particles split starting from the edges, where the surface energy driving force is higher, in the direction of the minor axis. The following coarsening increases the minor axis faster than the major axis, to pursue a higher circularity.

The minor axis can increase from 7 to 15 μm , thus confirming the decrease in aspect ratio as a function of both temperature and time. Figure 60 clearly shows that higher temperature means more phases which are molten progressively, thus increasing the material flow. The logarithmic dependence found in Figure 61 well represents the growth of this parameter as a function of time. A increase to 150% of the original value is noticed after 10 minutes only, then the increase is slower at longer times. A particle's minor axis can reach over three times its original value at long times. The minor axis increases to a higher extent than the major axis, thus reducing the aspect ratio considerably. Its increase occurs all over the sample, despite the different thermal history. The same position profiles are kept for untreated and treated samples, but the value increases to different extents according to time and temperature of the heat treatment applied.

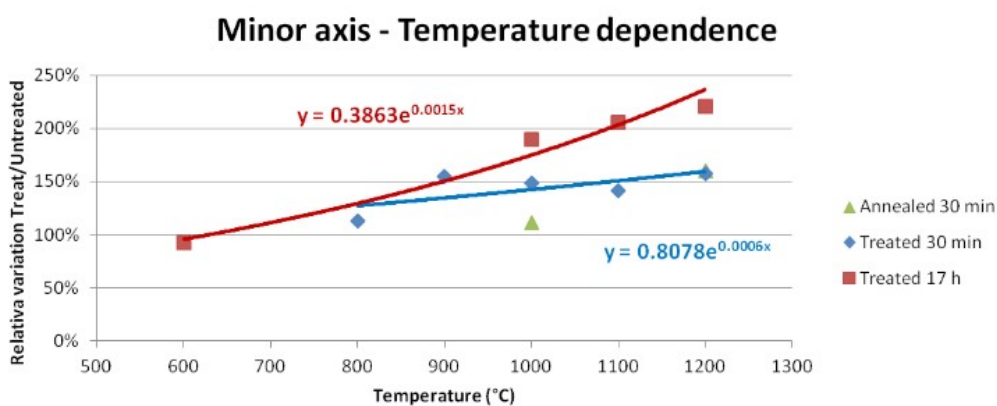


Fig. 60: Temperature dependences at different times of the relative variation for minor axis

Minor axis - Time dependence at 1200°C

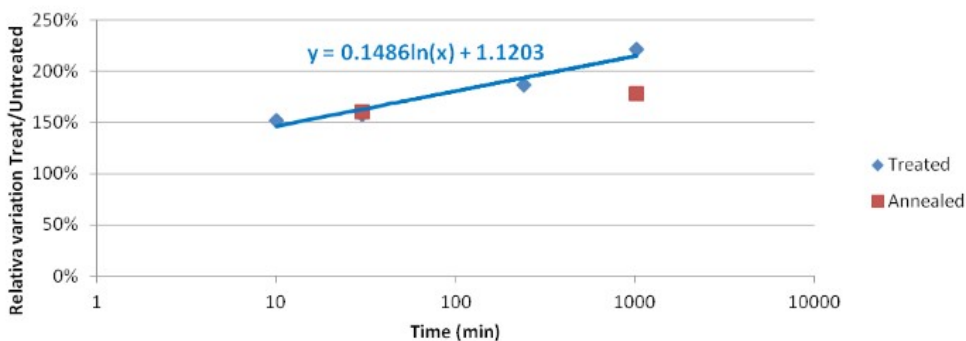


Fig. 61: Time dependence of relative variation of minor axis at 1200°C

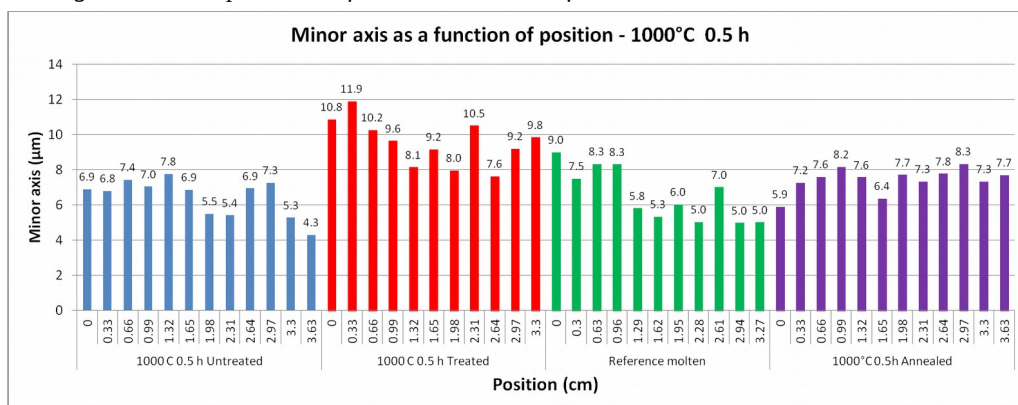


Fig. 62: Minor axis as a function of position in samples showing splitting, compared to their relative references

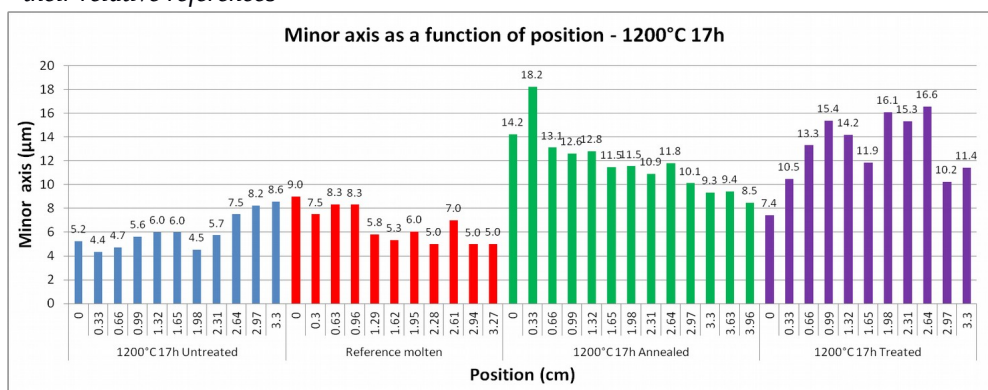


Fig. 63: Minor axis as a function of position of samples showing coarsening, compared to their relative references

2.3.6 Evaluation of uncertainties and further comments

During the heat treatments in the furnace, the actual surface temperature has been assumed to be the same measured by the furnace thermocouples, and it has been supposed to be constant all over the surface. Since the sample is very small compared to the furnace, the variation of the temperature value all over the surface can be considered constant. However, the heating elements on the side of the furnace might have had a higher temperature. The furnace thermocouple is located about 10 cm above the sample. The furnace chamber dimensions are 15x15x15 cm³.

The carbon mold also screens partially the heating of the material. Despite this, the material was molten successfully. The furnace chamber is very small, so the uniformity of the temperature in the furnace can be considered quite high. There might be a deviation from the measured value in the actual temperature of the cast.

Errors in the geometrical parameters analysis performed after SEM can be due to the slight differences in microstructure and to the wide distribution of the data. It is important to notice that the standard deviations are really high, almost in the same order of magnitude as the average value, or even more than twice. Even if the data are widely dispersed, the average value can still give a satisfying overview of the effects of the heat treatment. Despite one single experiment was performed for each condition, the results have significant dependences in time and temperature. The formulas reported on the graphs are shown to give a qualitative overview, but they should be further inquired.

3 COMPOSITIONAL CHARACTERIZATION

3.1 EXPERIMENTAL

3.1.1 XRF analysis

A XRF chemical analysis has been carried on the untreated material and the sample annealed at 1200°C for 17 hours. The material as cast was analyzed by Henning Kjørnli and the annealed material's analysis were carried out by Ingvill Vikan Myhre. Both the analysis have been performed at Elkem Thamshavn.

The composition of a simple piece of material was obtained for an untreated sample. The annealed sample underwent a different analysis. Once a specimen for metallographic analysis had been extracted, the remaining material was sliced in the horizontal direction. The cut was performed manually by using a 2 mm thick diamond blade disc. Five slabs were obtained from this procedure. Each layer had a thickness of approximately 5 mm. The external layers of carbides and oxides have been removed by grinding with SiC-paper.

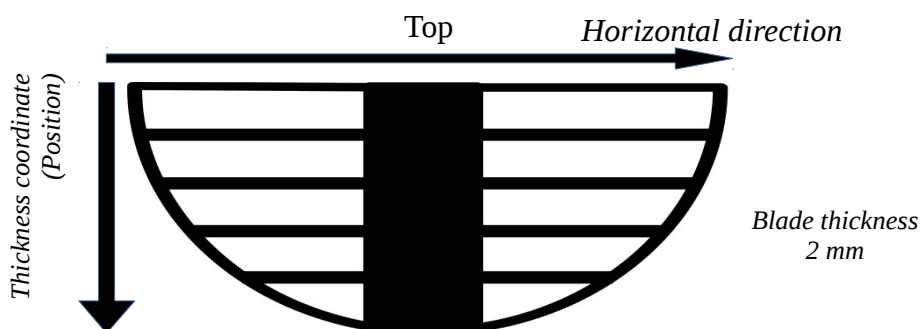


Fig. 64: Cross-section of a cast. The material used for the chemical analysis is coloured in white. The central black spot corresponds to the material previously used for the SEM analysis.

3.1.2 EPMA and X-ray mapping

EPMA (Electron Probe Micro-Analysis) has been performed on the samples used for the metallographic analysis by using a JEOL JXA-8500F. The work has been performed together with Morten Raanes at the Department of Material Science and Technology at NTNU.

EPMA was carried on two samples: the one treated at 600°C and the one annealed at 1200°C, both for 17 hours. Sizes, aspect ratio and positions in the cast of the selected intermetallics have been recorded. Points showing different contrasts inside the intermetallic were selected to detect the relative mass percentage of Fe, Al, Si, Ca, Ti, O, Mn, Ba and Cu. A conversion to atomic percentage gave the phase composition. It was possible to spot the correct phase thanks to the information collected from literature.

X-ray mapping was performed on two particles for each sample. Ba was not included in this analysis.

3.1.3 EDS-BSE-ImageJ[®] analysis

EDS and BSE images were chosen to further analyze the two samples which underwent EPMA, as well as an untreated MG-Si sample. The microscope was the same from the geometrical analysis performed in Chapter 2 of this work (Hitachi SU-6000 FE-SEM). Each image has a different scale according to the size of the intermetallic, but a resolution of 2560x1920 pixel was kept. The EDS-spectra detected the elements present in the phase in a single point. The contrast and the previous experience from EPMA analysis led to the detection of the phase in the chosen point. This method was faster, even if it could not give the high precision which characterizes EPMA.

The phase percentage in the intermetallics was calculated by an ImageJ[®] analysis. Extension of areas with different contrast have been recorded. The phase percentage in each intermetallic has been calculated by relating the measured areas to the hosting intermetallic area. Si precipitates were also

noticed, but their area has not been included in the intermetallic area.

3.1.4 TFS (TiFeSi₂) characterization

Small particles were detected inside the intermetallics during the ImageJ[®] analysis. Their size distributions and circularity varied relevantly before and after the treatment. A detailed image analysis was thought to be relevant to further describe transformations happening during the treatment. The precipitates identified as TFS (TiFeSi₂) particles. They were easily spotted by the high contrast they showed in relation to the other phases present. Data about area, circularity and number of precipitates per intermetallic were collected by an analysis with ImageJ[®]. Particles with sizes below 50 pixel/ptc have been disregarded because of their impossibility to be resolved. The data were collected and graphs were created on LibreOffice Calc[®] and Microsoft Excel[®]. Table 9 resumes the number of intermetallics analyzed with each method for each sample.

Table 9: Number of particles analysed and sum of their extension

Sample	EPMA	EDS	Total intermetallic area per sample (µm ²)
Untreated	0	54	113 633
600°C 17h Treated	29	31	166 507
1200°C 17h Annealed	21	33	171 761

3.2 RESULTS

3.2.1 XRF and SiStruc[®] analysis

Table 10 gathers the percentages of impurities in the samples analyzed. The values for the sample annealed at 1200°C for 17 hours are the average of the five slabs. An approximative composition of the untreated material is presented due to industry's restrictions. The relative variation is expressed by the

following formula:

$$\text{Relative variation} = \frac{\%X_{\text{treated}} - \%X_{\text{untreated}}}{\%X_{\text{untreated}}}$$

Table 10: Average value of the %wt. of Fe, Al, Ca, Ti found after XRF analysis

Element	Untreated	1200°C 17 h Annealed	Relative variation
Fe	0.40	0.27	-20%
Ca	0.05	0.04	-35%
Al	0.15	0.12	-10%
Ti	0.05	0.02	-25%

Inserting these data in SiStruc[®] gave the possibility to make expectations about the content and the composition of the phases present in each sample. Table 11 resumes the results of the SiStruc[®] analysis and the differences in the amount of phases between the two samples. The percentage in brackets next to the %wt expresses the mass fraction of the phase if only the intermetallics were considered. The relative variation is expressed as specified earlier.

Table 11: SiStruc analysis performed on the untreated and the treated sample

Phase	%wt. untreated	%wt. annealed	Relative variation
FeSi ₂	0.458 (47%)	0.361 (48%)	-21%
CaAl ₄ Fe ₆ Si ₈	0.190 (20%)	0.104 (14%)	-45%
CaAl ₂ Si ₂	0.184 (19%)	0.118 (16%)	-36%
TiFeSi ₂	0.093 (10%)	0.067 (9%)	-28%
Al ₈ Fe ₅ Si ₇	0.023 (2%)	0.075 (10%)	226%
TiSi ₂	0.009 (1%)	0.009 (1%)	0%
Al ₃ FeSi ₂	0.009 (1%)	0.015 (2%)	67%
TOTAL	0.966 (100%)	0.749 (100%)	-22%

The total quantity of intermetallics decreases after the annealing. FeSi₂ is the most expected compound in both samples. The quaternary phase and CaAl₂Si₂

follow, but in the annealed sample their quantities decrease. TiFeSi_2 is present in the same relative mass fraction for each sample. $\text{Al}_8\text{Fe}_5\text{Si}_7$ is expected to increase after the annealing with respect to other phases. TiSi_2 and Al_3FeSi_2 might be found in low amounts.

3.2.2 EPMA and BSE-SEM analysis

As far as the chemical characterization is concerned, Table 12 collects the results of the EPMA analysis for the points chosen on each sample. Those points which are labeled as “unknown” show overlapping of several phases.

Table 12: Number of points with given phase analyzed by EPMA point analysis

Phase	600°C 17 h Treated	1200°C 17 h Annealed
Unknown	2	3
$\text{Al}_6\text{CaSi}_8\text{Fe}_4$	47	14
$\text{Al}_6\text{CaSi}_8\text{Fe}_4$ and TFS	3	5
$\text{Al}_8\text{Fe}_5\text{Si}_7$	2	9
$\text{Al}_9\text{Fe}_5\text{Si}_8$	1	0
Ba-Al-Si	1	0
FeSi_2	60	39
FeSi_2 and TFS	2	1
TFS	28	20
Si prec	7	2
Si prec and TFS	1	1
$\text{Al}_6\text{CaSi}_8\text{Fe}_4$ and FeSi_2	2	0
SUM	156	94

3.2.2.1 Untreated and treated sample at 600°C

Figure 65 and 66 show four complex intermetallic particles from the untreated sample and the sample treated at 600°C. These two samples have been compared in the same paragraph since the microstructure was very similar.

The particles coming from the solidification front meeting point contain all the phases predicted by SiStruc[®]. FeSi₂ is both present at its high temperature (HT) and low temperature (LT) structure. Particles of this phase can be distinguished from each other by the presence of cracks and Si precipitates in the LT-FeSi₂. Al₆CaFe₄Si₈ and Al₈Fe₅Si₇ do not show peculiar shapes and are detected all over the sample. CaAl₂Si₂ is mostly present in the center of the cast, especially at the edges of elongated intermetallics. TiFeSi₂ comes either as large particles at the borders of the intermetallic, or as rectangular precipitates in the intermetallics' cores. Eventual cracks formed go through FeSi₂ without crossing TiFeSi₂ particles in the majority of the cases. Other dissolved elements form compounds in minor quantity. Ba-Al-Si and Cu-Al-Si phases have been detected in the sample treated at 600°C.

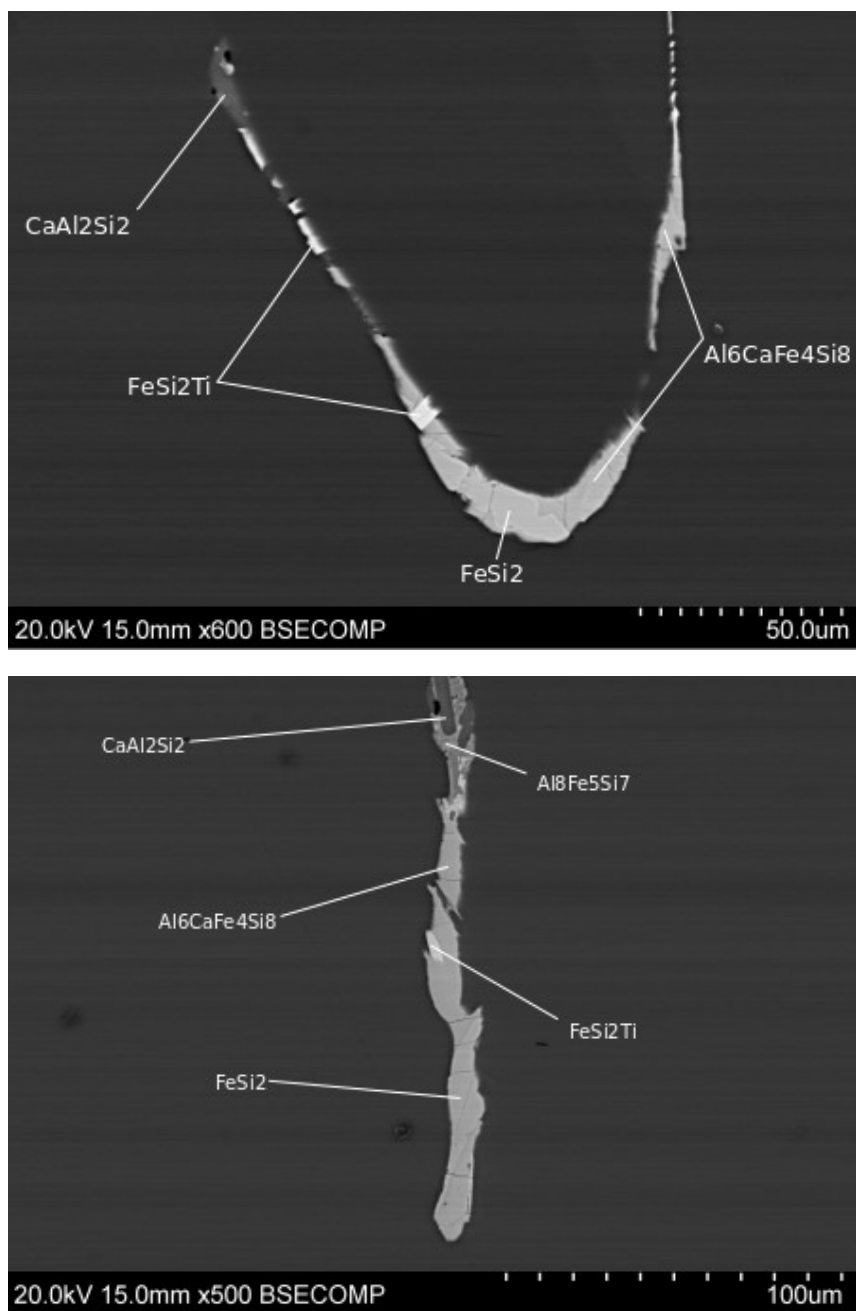


Fig. 65: Two particles coming respectively from the solidification fronts meeting point (A) and from the bottom (B) of the untreated sample

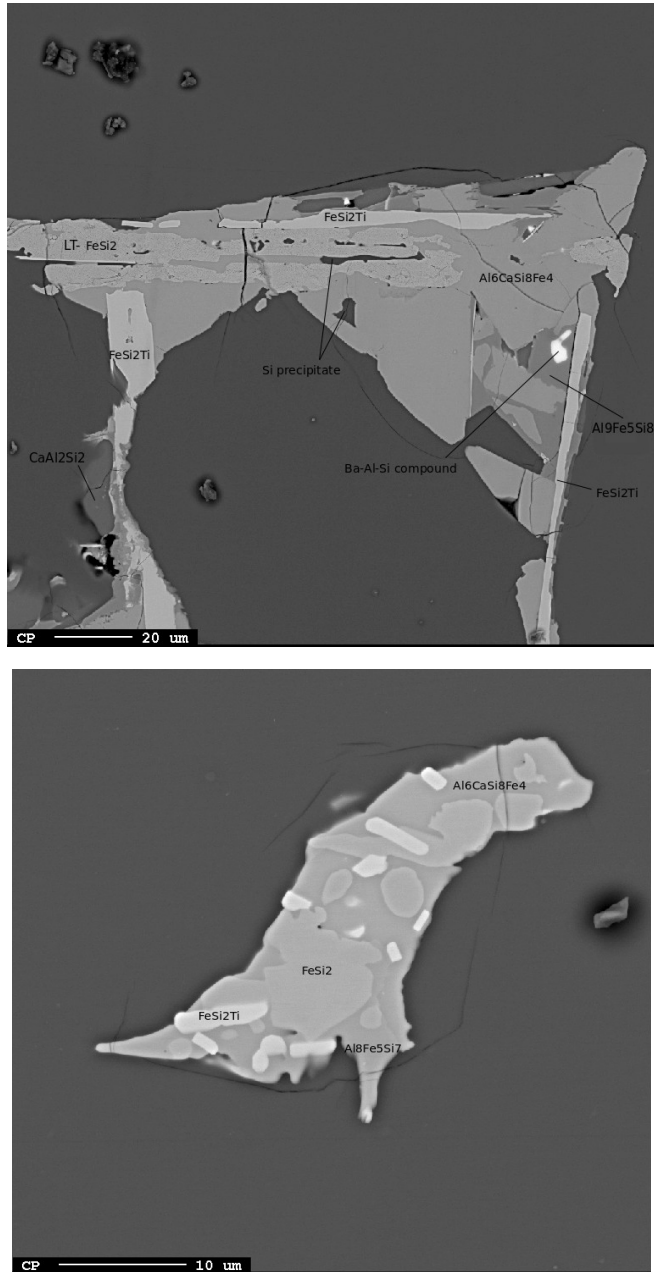


Fig. 66: Two particles coming respectively from the solidification fronts meeting point (A) and from the bottom (B) of the treated sample at 600°C

3.2.2.2 *Sample annealed at 1200°C*

Figure 67 shows two intermetallics found in the annealed sample. FeSi_2 is still the main compound present in the particles. HT-FeSi_2 was not found. Si precipitates and cracks are more frequent in this surface rather than in the former sample. Their quantity increases close to the areas where high quantities of LT-FeSi_2 are detected. $\text{Al}_6\text{CaFe}_4\text{Si}_8$ has reduced, as predicted by SiStruc[®]. This causes TiFeSi_2 to be the second most common compound in the sample. CaAl_2Si_2 was not found in any particle chosen, even if it was expected by SiStruc[®] to be the second most present phase. $\text{Al}_8\text{Fe}_5\text{Si}_7$ occupies larger areas of the sample compared to what was seen in the untreated material. TFS changes its features about the particle size distribution. It is more common to find high number of TFS particles, with irregular shapes and small areas. Some particles kept the rectangular microstructure anyway.

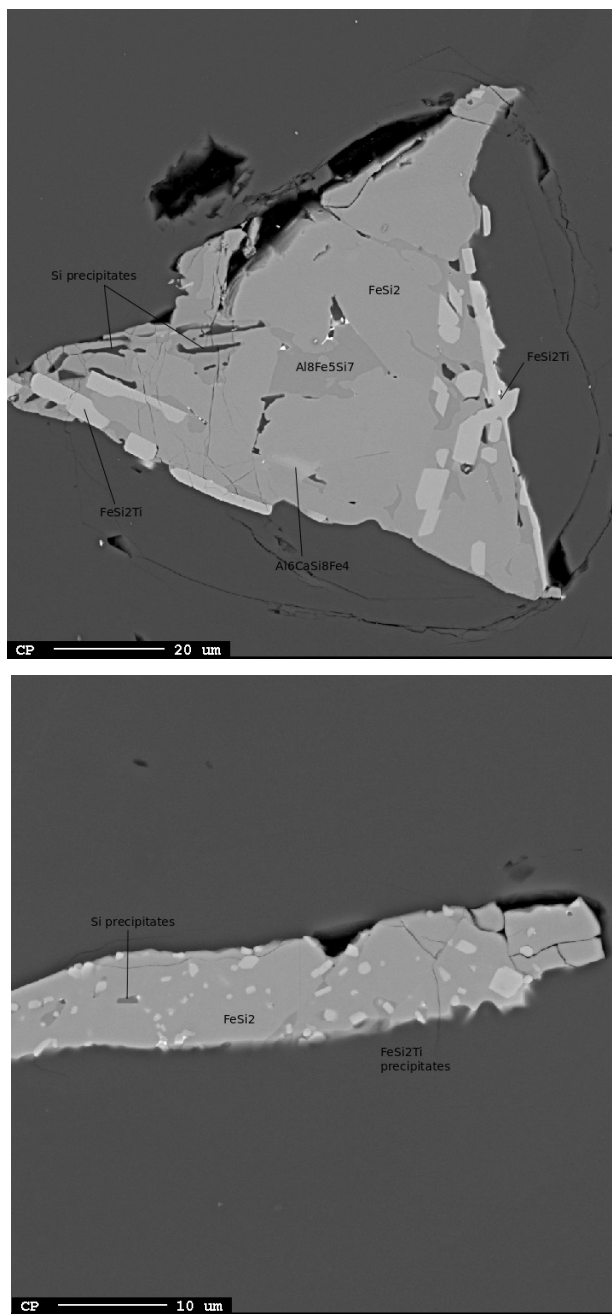


Fig. 67: BSE images coming from the center (A) and bottom (B) of the sample annealed at 1200°C

3.2.3 X-Ray mapping

X-ray mapping (Figure 68 and 69) shows the dispersion of 8 elements both in the intermetallics and in the silicon matrix. Where Al is present in high quantities (pink), the $\text{Al}_8\text{Fe}_5\text{Si}_7$ phase is identified together with yellow areas in the Fe-mapping and blue areas in the Si-mapping. The green area in the Al-mapping corresponds to the quaternary phase (light blue Ca, red Fe and light blue Si), whereas the turquoise one to CaAl_2Si_2 (pink Ca, red Si). In the end, the blue one corresponds to FeSi_2 (pink Fe and green Si). This compound can dissolve low quantities of aluminum. TiFeSi_2 corresponds to the pink spots in the Ti mapping. In this intermetallic, a Cu-Al-Si compound was found in correspondence of the pink area in the Cu-mapping.

For all the elements analysed, the solubility in silicon is much lower than the percentage found in the intermetallics. The areas outside the intermetallic are black or dark blue for most of the element mappings. Elements present in lower amount, such as Mn and Cu, prefer to dissolve in intermetallic phases rather than into silicon, especially in FeSi_2 , $\text{Al}_6\text{CaFe}_4\text{Si}_8$ and $\text{Al}_8\text{Fe}_5\text{Si}_7$. Oxygen was detected in the positions corresponding to the cracks, pores or scratches developed on the surface.

Figure 69 shows the mapping of an intermetallic particle from the annealed sample. The same considerations for the phases made earlier can be also made here. However, the quaternary phase looks different in contrast compared to the untreated sample in the BSE image. This was due to a slightly different setting in contrast between the two samples, since no relevant differences in composition were noticed.

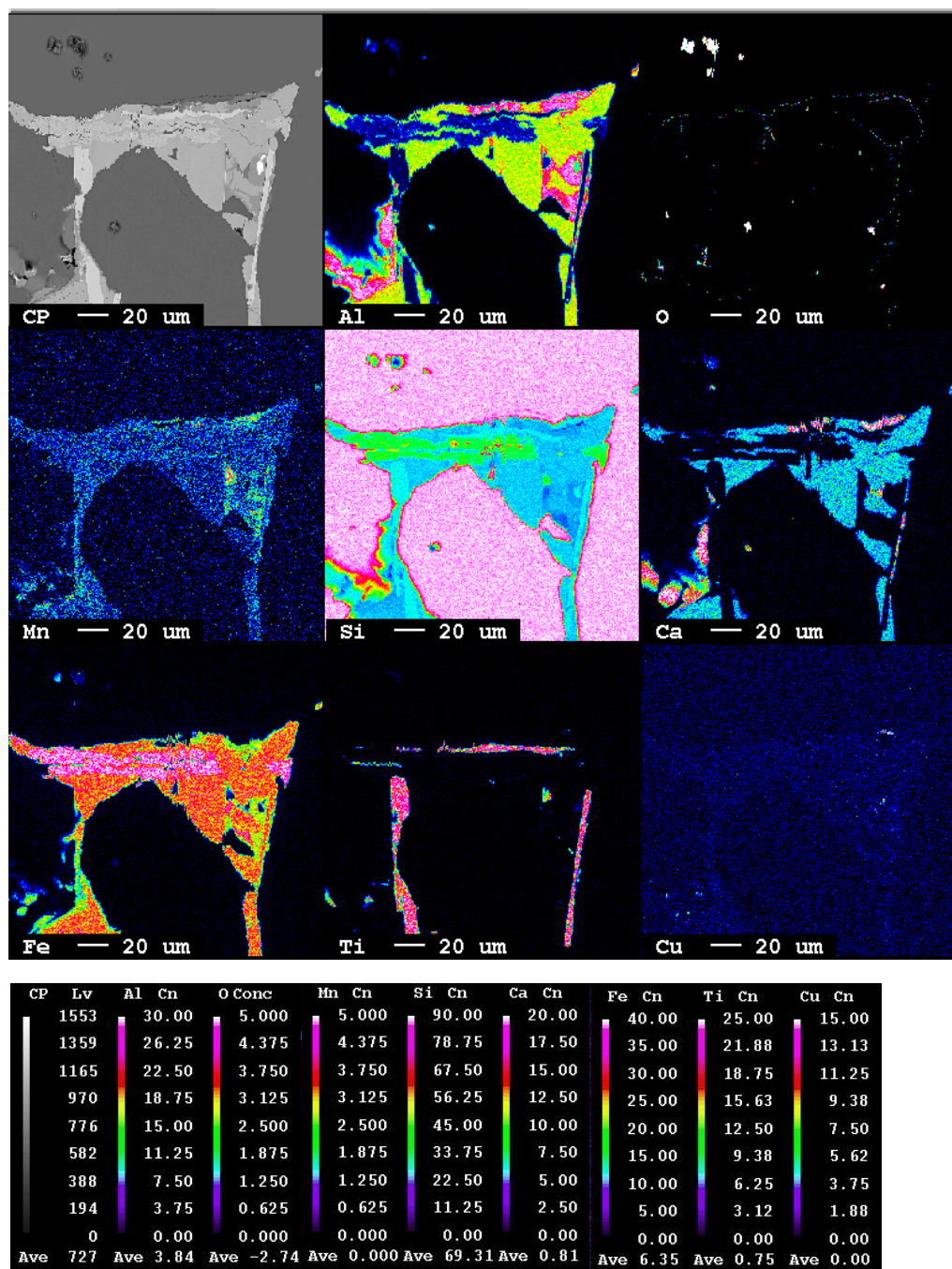
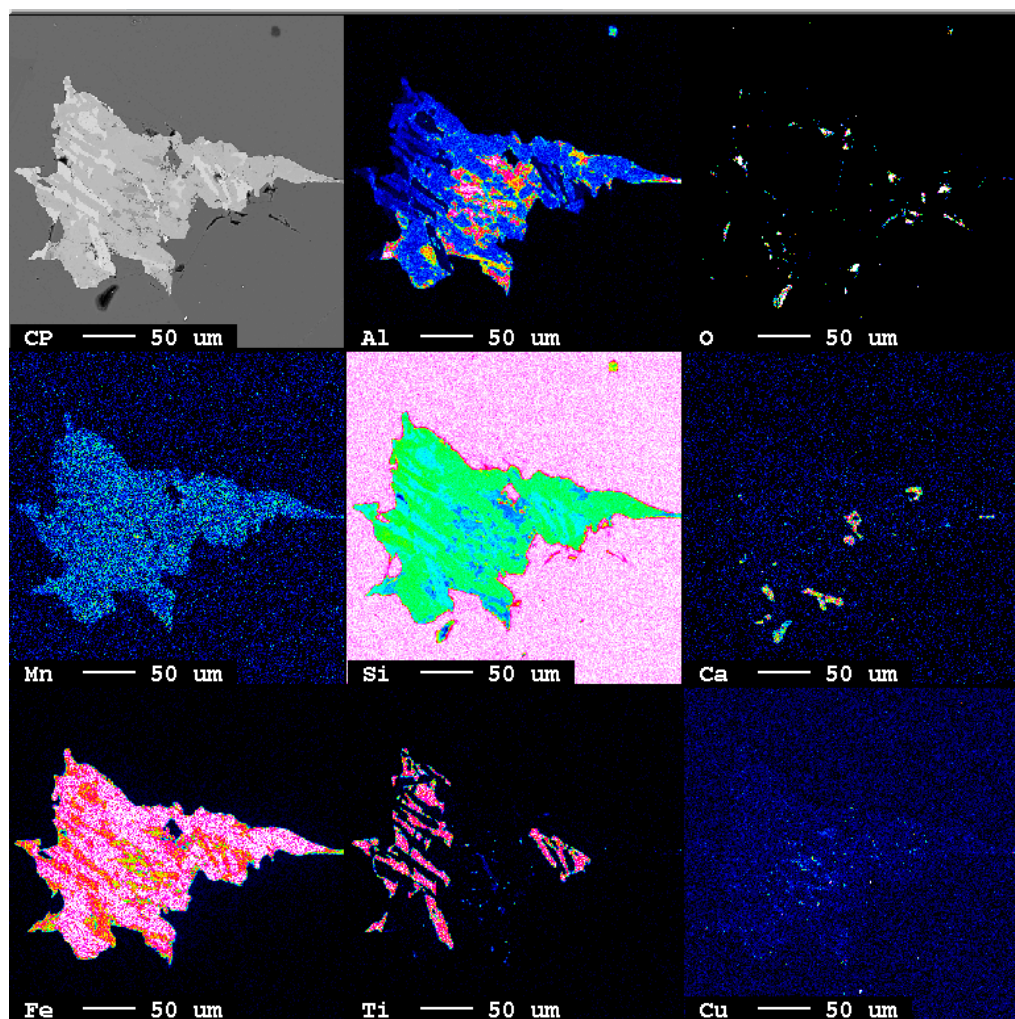


Fig. 68: X-ray mapping of a particle from the sample treated at 600°C



CP	Lv	Al	Cn	O	Conc	Mn	Cn	Si	Cn	Ca	Cn	Fe	Cn	Ti	Cn	Cu	Cn
1553	25.00	5.000		5.000		90.00	5.000	40.00	25.00	15.00							
1358	21.87	4.375		4.375		78.75	4.375	35.00	21.88	13.12							
1164	18.75	3.750		3.750		67.50	3.750	30.00	18.75	11.25							
970	15.63	3.125		3.125		56.25	3.125	25.00	15.62	9.38							
776	12.50	2.500		2.500		45.00	2.500	20.00	12.50	7.50							
582	9.38	1.875		1.875		33.75	1.875	15.00	9.38	5.62							
388	6.25	1.250		1.250		22.50	1.250	10.00	6.25	3.75							
194	3.12	0.625		0.625		11.25	0.625	5.00	3.12	1.88							
0	0.00	0.000		0.000		0.00	0.000	0.00	0.00	0.00							
Ave	749	Ave 1.59	Ave -2.74	Ave 0.000	Ave 72.68	Ave 0.000	Ave 7.97	Ave 0.75	Ave 0.47								

Fig. 69: Mapping of an intermetallic particle from the sample annealed at 1200°C

3.3 DISCUSSION

3.3.1 Chemical analysis: refining and segregation effects

Changes in composition were expected, since the material was molten in air in order to perform the annealing. Once the sample was extracted from the furnace, a white layer was noticed on the top of the cast (Figure 70). This layer is generated by the oxidation of the material during the melting step. Elements diffused to a slag phase from MG-Si. The slag will contain mainly Si, Al and Ca oxides. All these elements have negative ΔG at 1450°C, which is the highest temperature reached during the treatment (**Gaskell, 2010**). At temperatures slightly above 1450°C, Ca also starts to evaporate. This transformation could have happened as well, thus further reducing the content of calcium.



Fig. 70: White layer of oxide covering the top material from the annealed cast at 1200°C for 17 hours

Minor oxidation effects could have altered the quantity of Fe and Ti. Movement of impurities due to sweating could have moved some of these impurities to the slag phase. However, their ΔG for the oxidation reaction is less negative than silicon. Once Si becomes solid, elements are not able to diffuse rapidly to the slag. That explains the lower distribution coefficients for Ti and Fe compared to Al and Ca (Morita, 2003). The most plausible hypothesis for Fe and Ti decrease and impurities displacement in the sample (Figure 71) can be found in the segregation effect. The material for the chemical analysis was taken from the sides of the cast and not from the center. The segregation is controlled by the heat exchange coming from the lateral sides of the mold, as well as from the simple vertical solidification driven by radiation and convection with air. A solidification front is developing from the bottom with a slower velocity compared to the solidification front from the sides and from the top. This can be said since the sample was standing on a warm surface. The bottom of the mold was kept warm, so the developed temperature gradient was small.

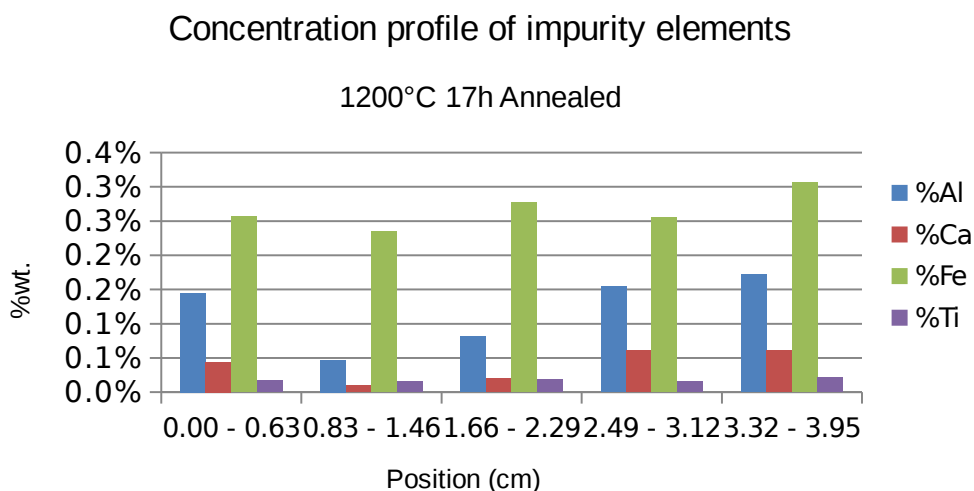


Fig. 71: XRF analysis as a function of position for the annealed sample at 1200°C. The position 0.00 corresponds to the cast bottom., and 3.95 to the interface between slag and silicon

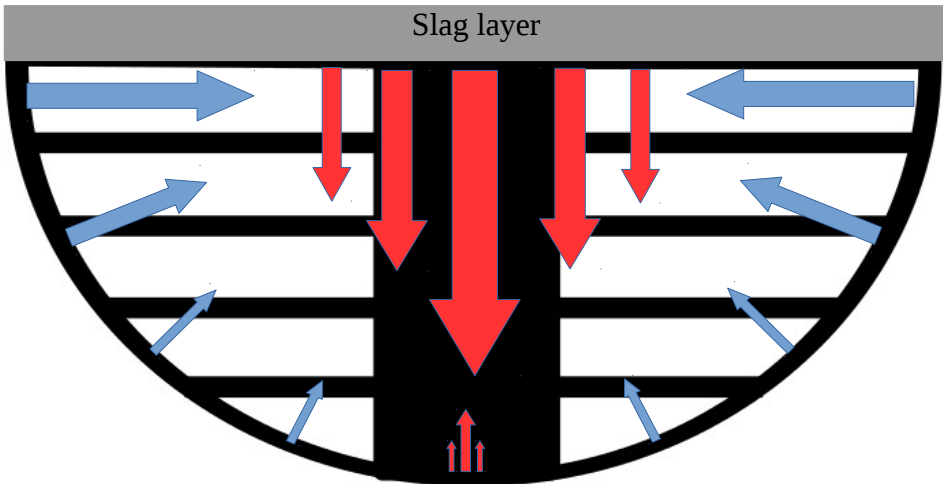


Fig. 72: Segregation and solidification sketch compared to the material extracted for chemical analysis (white areas) and the material collected for metallographic analysis, or discarded by cutting (black areas). The blue arrows show the movement of impurities caused by segregation effects, whereas the red arrows show the effects of directional solidification

3.3.2 Kinetic effects: untreated sample

It is important to underline that SiStruc[®] is a software merely based on thermodynamics. Since solidification in this case is far from equilibrium, data about %wt of different phases have to be handled carefully. Kinetics might have had effects on the final phase composition, thus causing deviations from the previsions calculated by SiStruc[®].

In the untreated sample, for instance, TiSi_2 and Al_3FeSi_2 were expected to be found at least in low quantities, whereas none of them was found. Besides $\text{Al}_6\text{CaFe}_4\text{Si}_8$ is found in higher quantity than CaAl_2Si_2 .

Having a look at the cooling ranges can give a good explanation of this difference between expectations and results. Figure 73 shows the cooling ranges calculated by SiStruc[®] for the composition of the annealed sample. They do not differ much from the results found from the material as cast, therefore the discussion will be valid for both. FeSi_2 will be the first compound which

solidifies. It will be the most present because of the high content of Fe in the material. TiSi_2 and TiFeSi_2 will form at the same point, but previous works have verified that TiSi_2 -formation reaction is hindered when there is a high presence of Fe (Sørheim, 1994; Rong, 1992). The same should be valid for CaAl_2Si_2 and $\text{Al}_6\text{CaFe}_4\text{Si}_8$. CaAl_2Si_2 forms at a lower temperature compared to $\text{Al}_6\text{CaFe}_4\text{Si}_8$. Ca will be involved in the quaternary phase transformation first, and what is left will start reacting with Al and Si to form CaAl_2Si_2 . It can be hypothesized that the formation of the quaternary phase has a faster kinetics than the formation of CaAl_2Si_2 .

The width of the melting ranges should not be considered as a crucial parameter, i.e. it is not true that the longer the melting range, the more phase will be present. Besides, the relative amount of element in the material will be the determining factor. Ca and Ti are present in a lower extent compared to Fe and Al. Ca is limiting the quantity of Ca-containing phases, and Ti does the same for the TiFeSi_2 phase.

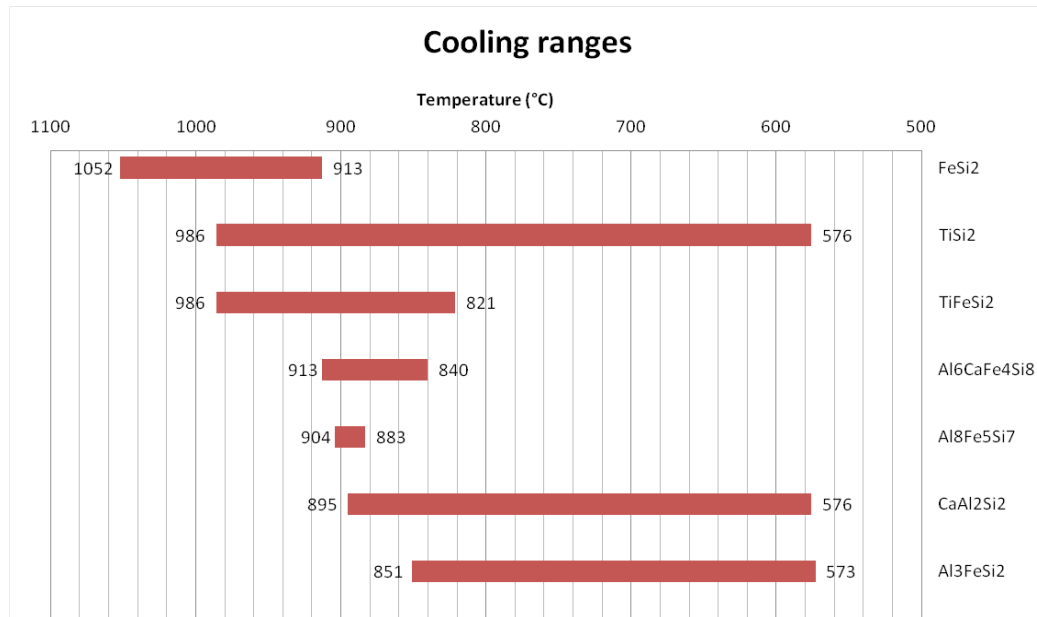


Fig. 73: Cooling ranges of intermetallic phases calculated by SiStruc[®]. The temperatures delimiting the melting range are written on the side of each bar

Figure 74 reports the content of phases predicted by SiStruc[®] compared to the content measured with ImageJ[®] from the samples. Ca-containing phases will be present in different amounts according either to SiStruc[®] or to the measurements performed. CaAl_2Si_2 is present in lower amounts since it is the last Ca-containing phase which solidifies. At that point, Ca would have already reacted to form $\text{Al}_6\text{CaFe}_4\text{Si}_8$. FeSi_2 is formed in a slightly different percentage. Fe will rather form FeSi_2 or TiFeSi_2 in the annealed sample, since the Ca content is reduced by the refining effect. Ti is affected only by segregation, therefore TiFeSi_2 will be relatively be more present compared to the other phases. $\text{Al}_8\text{Fe}_5\text{Si}_7$ increases relevantly but its relative percentage is still very low. In the end, the similarity between the sample treated at 600°C and the untreated sample shows that at this temperature no changes in phase composition are happening. The microstructure of the intermetallic is not altered, either chemically or geometrically.

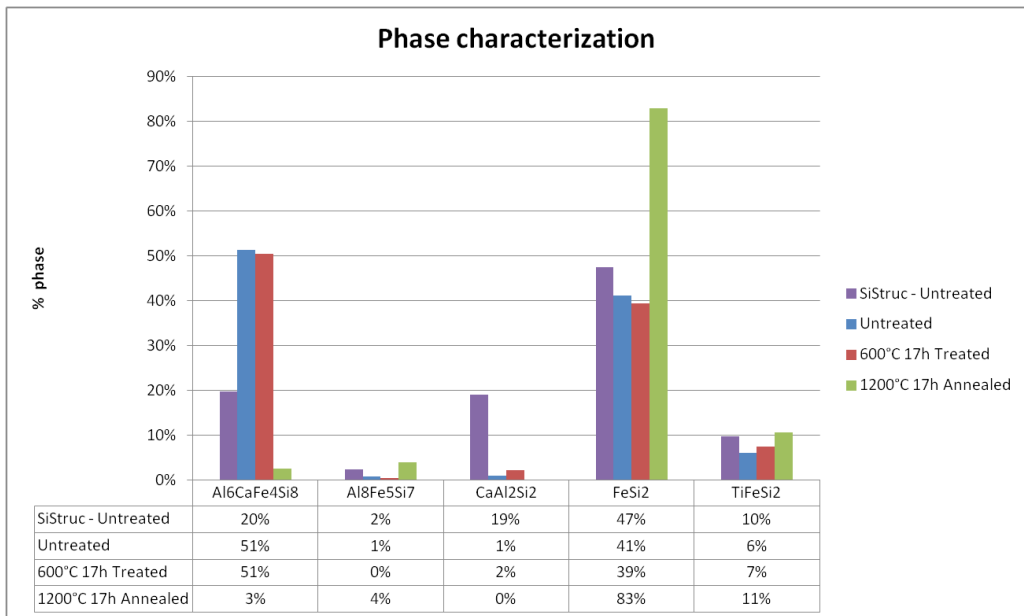
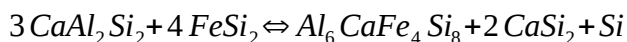


Fig. 74: Phase characterization. Comparison between SiStruc[®] calculation and image analysis

3.3.3 Chemical reactions: annealing effect

Chemical reactions happening in the sample are also disregarded by SiStruc[®]. The main reactions are two. The first one is a proposed mechanism by **Margaria (1994)** which involves several intermetallic phases in MG-Si. The second is a structural transition from a metastable to a stable lattice structure of the FeSi₂ phase, which was confirmed by several experiments and previous works (**de Huff, 1969; Anglezio, 1990; Boomgard, 1984; Margaria, 1996; Bjorndal, 1990; Tveit, 1988**).

According to **Margaria (1994)**, an annealing at 900°C decreases the quantity of CaAl₂Si₂ and increases the amount of Al₆CaFe₄Si₈ according to the equilibrium



This reaction is just a proposed mechanism. A temperature dependence was estimated after annealings performed by **Margaria (1994)**. Unfortunately the present work cannot prove that this reaction is happening. The equilibrium reaction should increase the content of quaternary phase after an annealing. However, the quantity of Ca lost during the melting step was higher than expected. Therefore the quaternary phase is noticed in lower amounts in the annealed sample, and CaAl₂Si₂ might have not formed. If it did, the annealing would start the reaction until its total consumption. CaSi₂ was not found in the annealed sample. The chemical composition of the analysed silicon does not fall in the CaSi₂ existing range in the graph traced by **Margaria (1990)**.

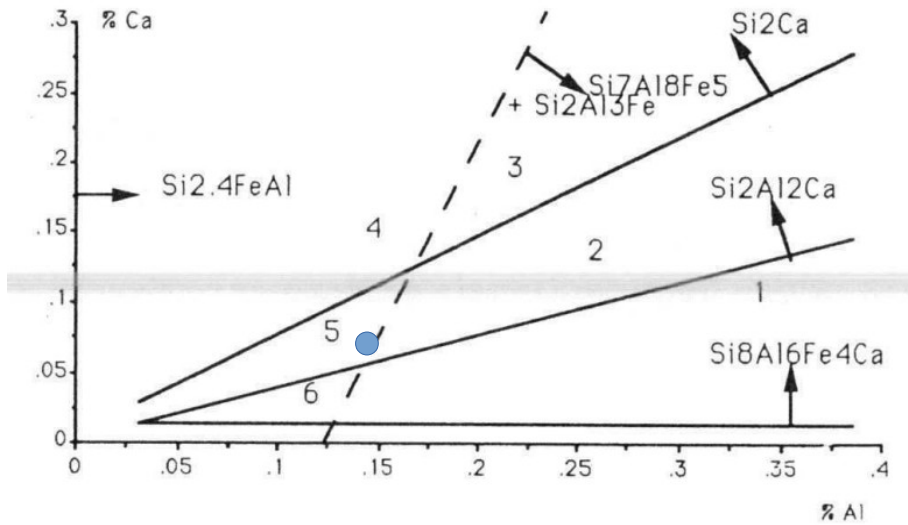


Fig. 75: Compositional range of intermetallics in industrial MG-Si (**Margaria, 1990**). The composition chosen of the untreated material in this work corresponds to the blue point in the diagram

Si precipitates are formed in areas close to the $FeSi_2$ phase. This phase experiences a transition from the high temperature to the low temperature structure. This reaction enlarges the lattice parameters of this compound, transforming it from $FeSi_{2.4}$ (high-temperature structure) to $FeSi_2$ (low-temperature structure) according to the equilibrium



Dilatation of lattice induces stresses in the phases and causes cracks. Cracks created pass through the silicon matrix and all the common intermetallic phases except $TiFeSi_2$, as shown from a similar work performed by **Jo (2014)**. Silicon absorbs part of the stress caused by this dilatation. It is universally known that this material has very low ductility, but it seems it has enough to absorb this stress. If the ductility of silicon had not been high enough, cracks would have widely branched all over the surface with high speed. This transformation has partially occurred in the untreated sample during its solidification in the industrial mold. Annealing can enhance the formation of LT- $FeSi_2$ and the

precipitation of silicon. In an annealed sample, cracks will be larger and more common. Figure 76 and 77 show intermetallics from an untreated and from an annealed sample.

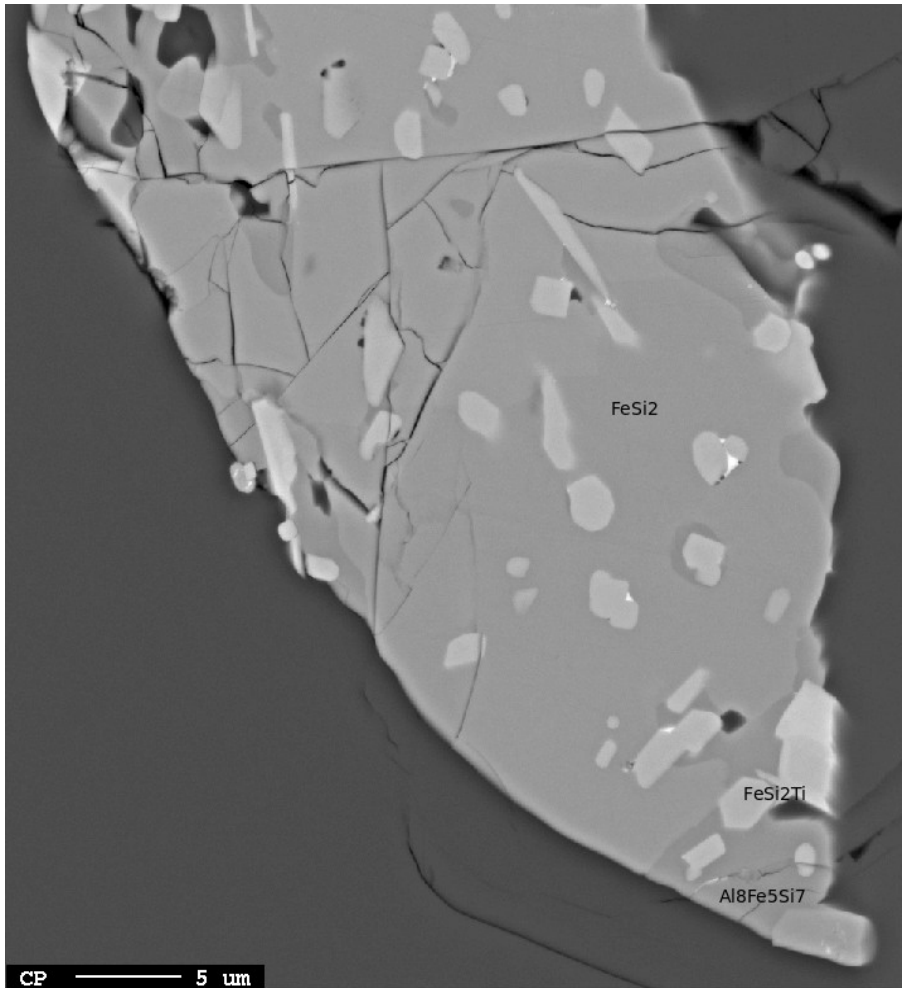


Fig. 76: Intermetallic from an annealed sample at 1200°C for 17 hours

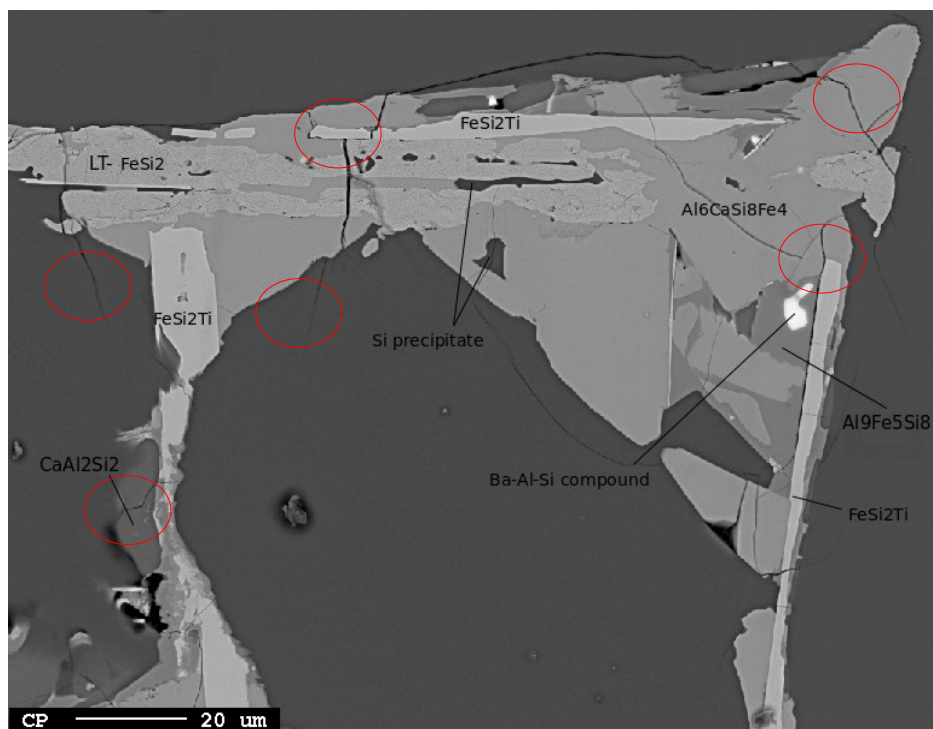


Fig. 77: Cracks in intermetallic going through silicon, FeSi₂, Al-Fe-Si phases and Al₆CaFe₄Si₈, but in most cases not through TiFeSi₂. Picture from sample treated at 600°C

3.3.3 Minor elements in intermetallic phases

Oxygen is not supposed to be present inside the intermetallic phases. A certain amount of this element is detected anyway because of the micro-cracks which expose the material to air. An annealing increases the complete formation of LT-FeSi₂. A higher number of cracks is noticed in the annealed sample.

X-ray mapping confirms that elements present in minor quantities, such as Mn or Cu, tend to dissolve in intermetallic compounds rather than in silicon. Solubilities of elements in silicon are extremely low. For example, Mn has a solubility of the order of $\chi = 10^{-7}$ and Cu of $\chi = 10^{-5}$ in silicon at 1200°C (Tang,

2010), whereas about 0.5%wt Mn or 0.3%wt Cu are found in TiFeSi_2 for example. P is present in low amounts in every phase considered. The solubility of these impurities in intermetallic phases has not been found in literature. Table 13 resumes the amount of minor elements content in the intermetallics found in this work. A similar discussion for Al, Si, Ca, Ti and Fe cannot be made. The overlapping signal from the surrounding phase could alter the results.

Table 13: Average %at. of minor elements present in the two samples analysed

Sample	Phase	P	O	Cu	Mn	#points
600°C 17h	Si prec	0.01	1.75	0.01	0.01	7
	TFS	0.02	1.61	0.01	0.50	28
	$\text{Al}_8\text{Fe}_5\text{Si}_7$	0.02	1.31	0.00	0.38	2
	$\text{Al}_6\text{CaSi}_8\text{Fe}_4$	0.04	0.88	0.02	0.29	47
	FeSi_2	0.01	0.66	0.01	0.31	60
1200°C 17h	Si prec	0.01	0.34	0.04	0.05	2
	TFS	0.12	1.16	0.01	0.53	20
	$\text{Al}_8\text{Fe}_5\text{Si}_7$	0.00	0.45	0.27	0.44	9
	$\text{Al}_6\text{CaSi}_8\text{Fe}_4$	0.06	0.71	0.16	0.21	14
	FeSi_2	0.01	0.41	0.01	0.43	39

3.3.5 TiFeSi_2 (TFS) geometrical characterization

TiFeSi_2 particles were noticed to have a characteristic shape. It could be that TFS develops a high difference in surface energy with FeSi_2 and $\text{Al}_6\text{CaFe}_4\text{Si}_8$. When FeSi_2 is solid, TFS is still liquid in the range from ca. 1050°C to 980°C. The material crosses this temperature range in ca. 5 minutes during solidification. The repulsion makes TiFeSi_2 create several droplets all over the surface. The solidification is very fast for the annealed sample. Particles did not have enough time to reorganise and coarse. Industrial solidification has a longer

time compared to the sample cast in the carbon mold. In the industrial case, the area will be larger and the particles more regular in shape.

The main difference in the TFS characterization before and after a treatment is the number of particles. Figure 78 shows the relation between the hosting intermetallic particle size and the number of TiFeSi_2 particles found inside it. As expected, the green and the red points are almost overlapping. They represent respectively the untreated and the sample treated at 600°C . The blue points represent the annealed sample. It was more common to find a higher number of particles in the annealed sample because of the faster solidification after the annealing was performed. Samples treated at least at 1000°C show the same behaviour, even if a detailed geometrical analysis was not performed.

The solidification of TFS is an event which is also influenced by the local composition. The bigger the intermetallic, the more TFS it will contain in comparison with smaller ones. Figure 79 shows the relation between the hosting intermetallic area and the sum of the area occupied by TFS phase. In each sample, bigger particles have higher quantity of TFS. The difference between the three samples is due to a difference in the area considered for this analysis.

A position dependence was not clearly found. Size distributions and TFS particle numbers are depending on the local composition rather than on the solidification process. The tendency lines in Figure 80 do not show a statistically significant position dependence. However, the highest amounts of TFS are detected in the position close to the last stage of the solidification process. It is not surprising to see a low amount of TFS at the edges of the untreated sample and at the top of the annealed.

The average aspect ratio of a single TFS particle was also related to the hosting intermetallic area. Before the treatment, the particles look more rectangular and regular. Aspect ratios can reach values up to 12 in some cases. After the treatment, droplets start to form. The quick solidification does not allow the complete recrystallization of the TFS phase. The shape looks more circular than rectangular. The aspect ratio is drastically reduced to an average of

3. Larger intermetallics had slower solidification times. The reorganization could reach a higher extent at long times. Figure 81 shows the graph relating the hosting intermetallic area and the average TFS particle aspect ratio.

In the end, the average area of a TFS particle in each intermetallic has been related to the hosting intermetallic area. The particles get smaller after annealing. Some cases still keep high extension. They have been coloured in purple in Figure 82. They created a deviation which was disregarded when tracing the tendency line. As it occurs for the total area dependence, the larger the intermetallic, the larger the TFS particles generated.

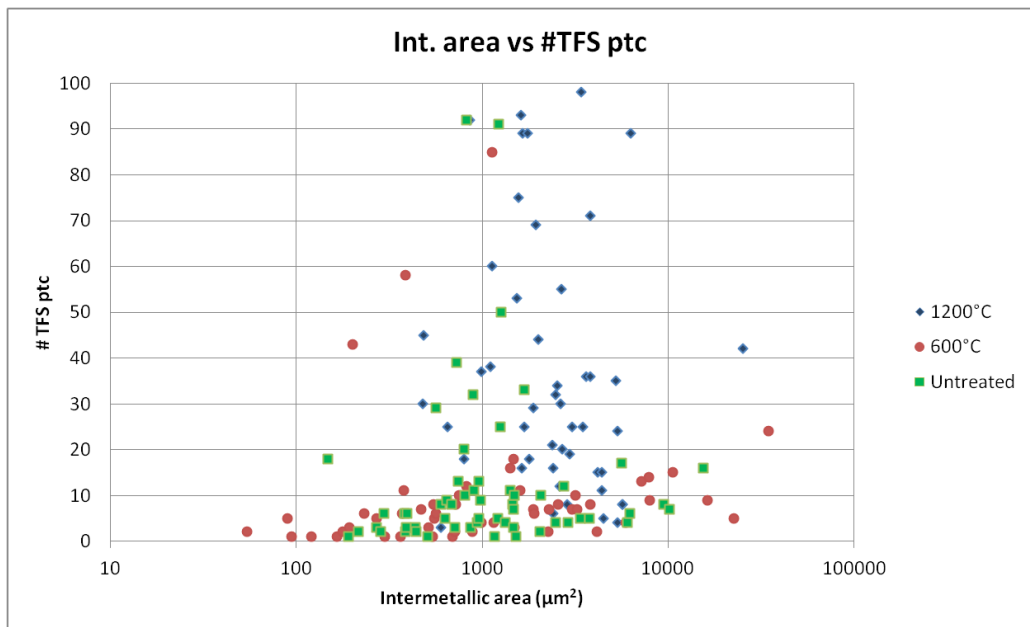


Fig. 78: Hosting intermetallic area related to number of TFS particles counted inside

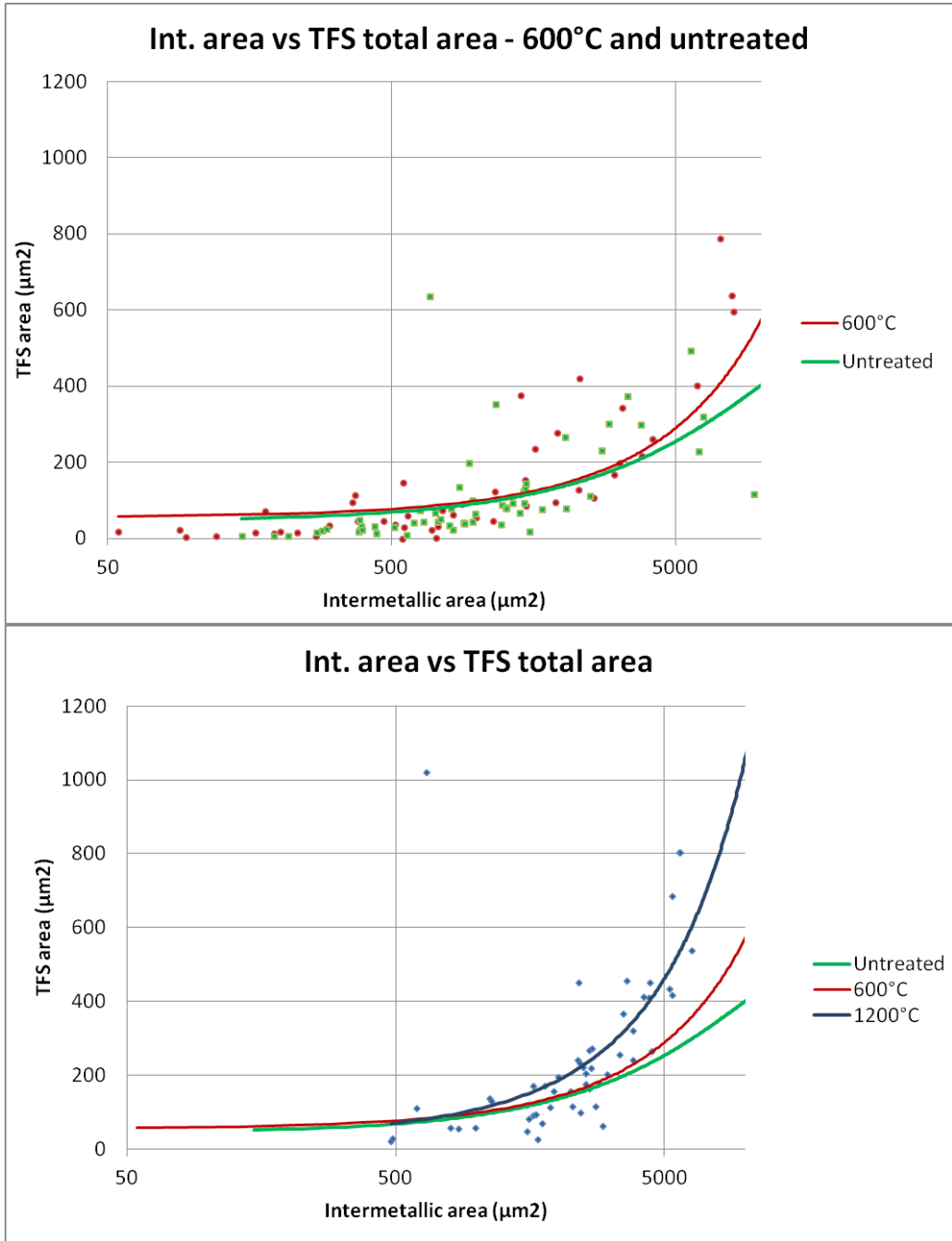


Fig. 79: Relation between hosting intermetallic area sum of TFS particles area. Focus on similarity between 600°C and untreated (a) and comparison with the annealed sample (b)

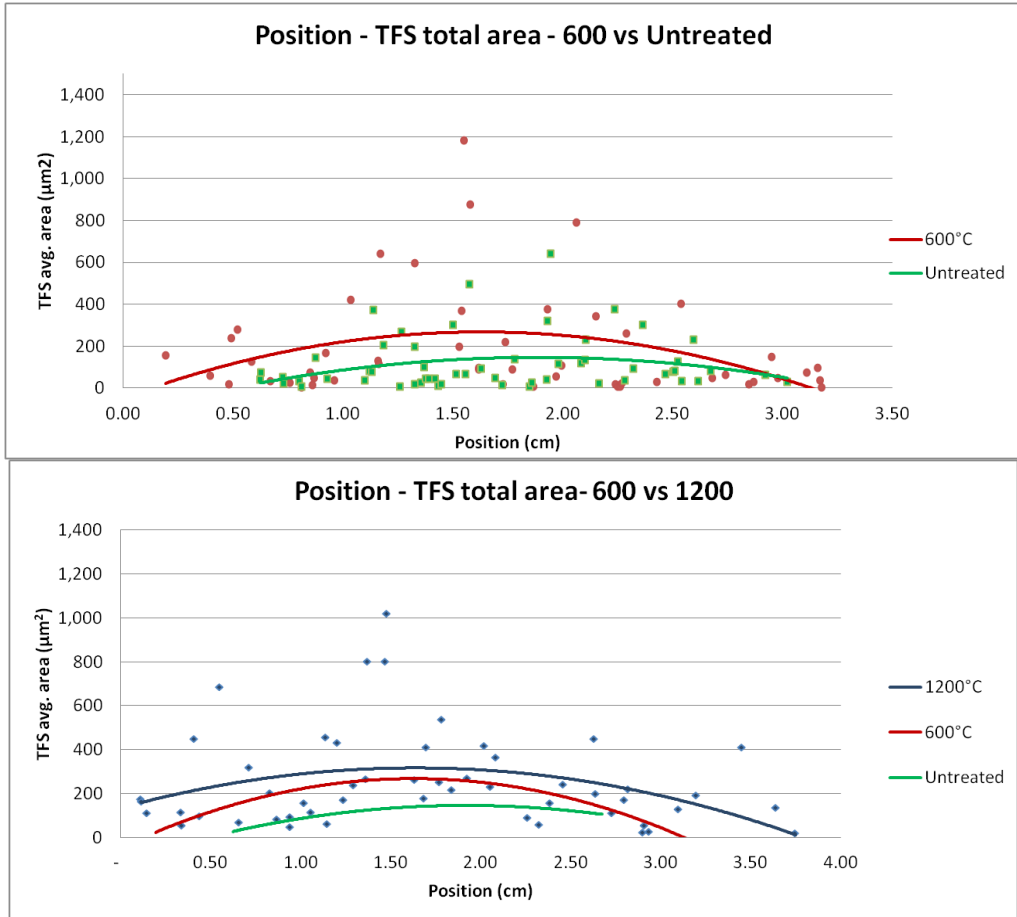


Fig. 80: Relation between position and sum of TFS particles area. Focus on similarity between 600°C ad untreated (a) and comparison with the annealed sample (b)

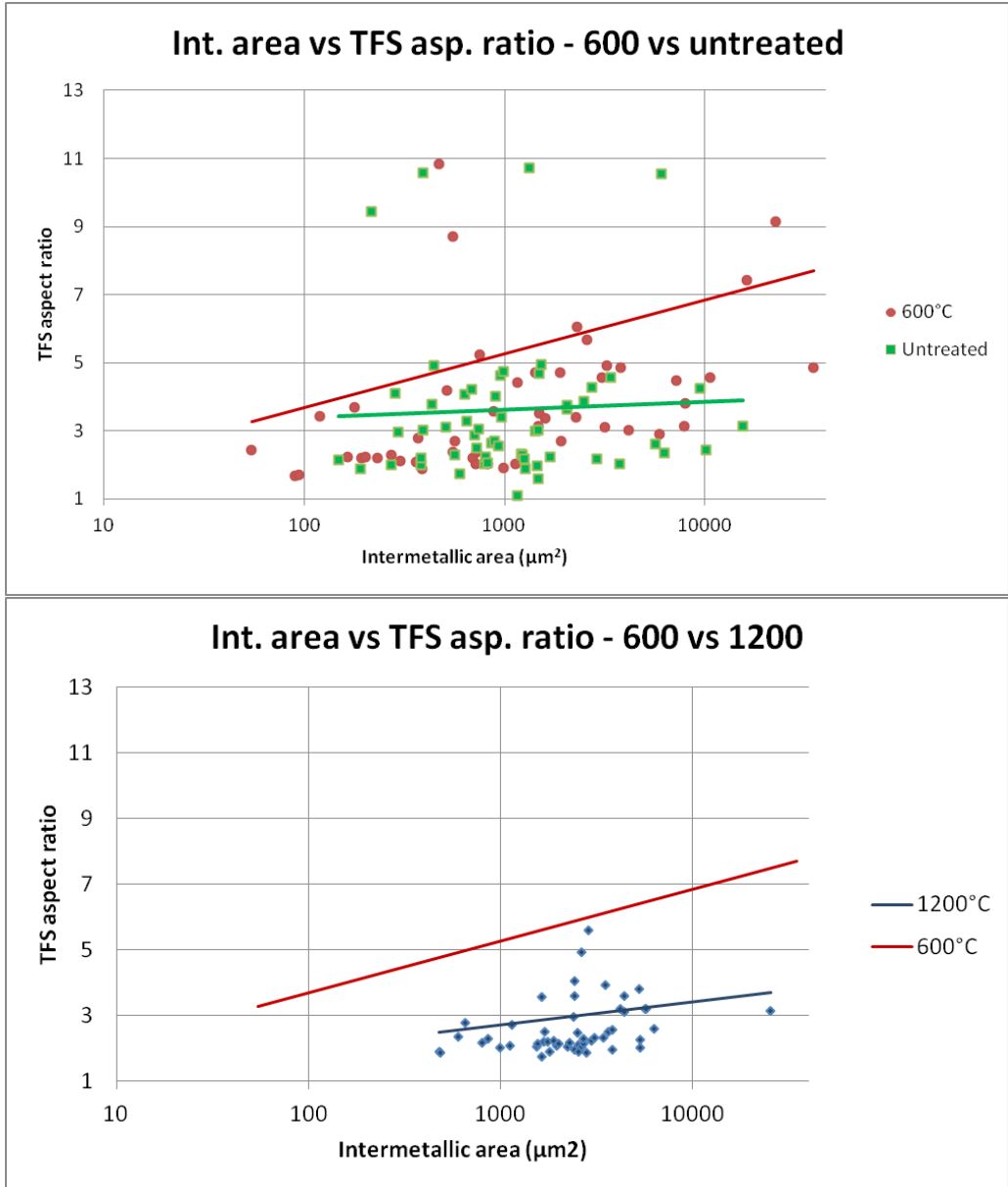


Fig. 81: Relation between hosting intermetallic area and average TFS particle aspect ratio. Focus on similarity between 600°C ad untreated (a) and comparison with the annealed sample (b)

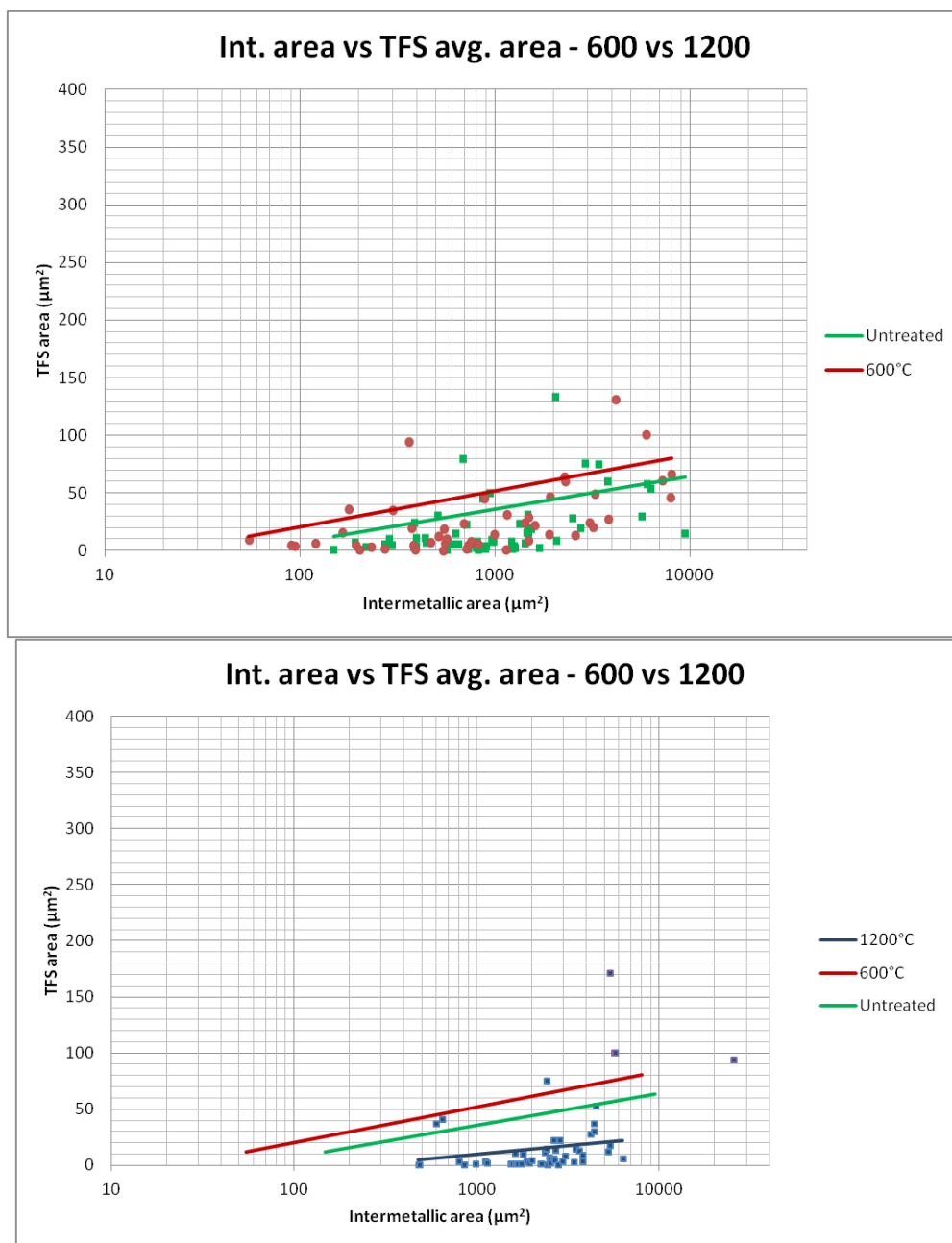


Fig. 82: Relation between hosting intermetallic area and average TFS particle area. Focus on similarity between 600°C ad untreated (a) and comparison with the annealed sample (b)

3.3.6 Evaluation of uncertainties and further comments

The XRF signal will count the total amount of the alloying elements present in every phase. This includes intermetallics, oxides and silicon matrix. The material analyzed by XRF was inhomogeneous. The oxides and the carbides formed respectively at the top and at the sides of the mold have been grinded away with SiC paper. No other contamination is involved.

Experiments could have been carried on in an inert atmosphere to limit compositional changes. Refining and segregation effects needed to be discussed together for those samples which have melted. It was necessary to avoid misunderstandings about the impurity elements mass balance and elements distribution in the sample. Despite the variation in chemical composition, Chapter 2 shows that the transformation happening to the intermetallic shapes are the same also when a melting step is not performed.

The electron beam used for EPMA analysis will penetrate the surface and extract electrons from a phase below in some cases. Some neighbouring phases can be involved as well, since the beam has a circumference of 1 μm radius. EPMA was the best method available for this analysis. It was confirmed to be enough precise to express clear statements about the phase composition.

Grain boundary diffusion can also have its own effect at 1200°C. From previous works, it can be seen that Al can diffuse at grain boundary as fast as Fe in the bulk. Diffusion would happen also in solid state. However, the results found in literature refer to a low and narrow temperature range which is not covered in this work. In any case, the higher the temperature, the smaller the difference between bulk and grain boundary diffusion lengths.

4 CONCLUSIONS

The previous experiments carried on at Salten and the model developed for the characterization of the inclusions gave the expected results compared to the scanning of the thin cast untreated samples. The intermetallics are round and small close to the bottom and the top of the cast. They start showing elongated shapes and extended areas where the solidification fronts meet. The causes of this specific microstructure are related to macro-segregation, release of latent heat during solidification and reorganization of microstructure in the temperature ranges where the intermetallics are still liquid (1200-850°C).

Heat treatments were carried on MG-Si to detect variations in microstructure. Two thermal histories were chosen: one including a melting step, and one without it. In both cases it was noticed that an annealing over 850°C can enhance microstructural changes. The higher the temperature, the higher the speed of the transformation. The number of particles, circularity and extension will be affected. At short times, the splitting transformation occurs. Elongated particles will turn into many smaller round particles. At long times, such intermetallics will undergo Ostwald's ripening. Impurities will travel through the grain boundaries or bulk Si. Large particles will further increase in dimension and smaller intermetallics will disappear. The time effect is relevant after a 30 minutes treatment. This might be significant on a industrial scale (**Berget, 2014**), being 30 minutes a time in the order of magnitude of the solidification of a thin cast.

XRF chemical analysis and EPMA detected respectively chemical and phase composition. They were performed on the sample annealed at 1200°C with a melting step. The same analysis was made on an untreated sample and on a sample treated at 600°C without a melting step. It was demonstrated that these two have the same microstructure. This implies that at 600°C no change occurs in the material.

FeSi₂ is the most present phase both before and after the treatment. Ca was lost in relevant amounts after the treatment, thus decreasing Al₆CaFe₄Si₈ and CaAl₂Si₂ content. TiFeSi₂ (TFS) relative percentage was therefore higher after the treatment. The causes in the compositional changes were attributed to oxidation, segregation and chemical reactions. The first effect acts as a slag refining treatment. It decreases Ca and Al in MG-Si. Segregation moves Fe and Ti to the centre of the sample. The reactions are of two kinds. FeSi₂ undergoes a transition from HT- to LT-structure which decreases the percentage of this phase in the material and creates silicon precipitates. The second reaction consumes CaAl₂Si₂ and FeSi₂, according to literature studies. Al₆CaFe₄Si₈, CaSi₂ and Si are supposed to increase, but the refining step did not allow the creation of Ca-containing phases.

The TFS particle size, circularity and number have been inquired. TFS particles before a treatment look rectangular, large and regular. After the treatment the shape is closer to a circle, the extension is reduced and the number is increased. Surface energy effects and a quick cooling rate are thought to be the cause of the shape variation. The TFS particles are repelled from the solid substrate. A slower solidification could have allowed them to recrystallize in rectangular precipitates.

Final considerations about the effects of the annealing and refining on the production of MCS are resumed in Table 14 and 15. Table 14 only regards the relative mass percentage related to the intermetallic content. It is important to underline that an oxidation effect is decreasing the total content of intermetallics. Table 15 has been formulated by a comparison with Table 6. The conclusion are that refining effects decrease both reactivity and selectivity, whereas annealing increases selectivity but decreases reactivity.

Table 14: Variation in relative phase percentage after refining at 1450°C for 2 hours, followed by annealing at 1200°C for 17 hours.

Effect	FeSi ₂	FeSi ₂ Ti	Al ₈ Fe ₅ Si ₇	CaAl ₂ Si ₂	Al ₆ CaFe ₄ Si ₈
Annealing	÷	0	0	÷	+
Refining	+	+	+	÷	÷

Table 15: Expected effects on MCS production after a melting step of 2 hours at 1450°C and an annealing at 1200°C for 17 hours.

Effect	Phase	MCS reactivity change	MCS selectivity change
Annealing (Ca-ternary phase to Ca-quaternary phase, reduced FeSi ₂)	FeSi ₂	P	P
	FeSi ₂ Ti	0	0
	Al ₈ Fe ₅ Si ₇	0	0
	CaAl ₂ Si ₂	N	P
	Al ₆ CaFe ₄ Si ₈	N	P
	OVERALL	N	P
Refining (reduced Al and Ca content)	FeSi ₂	N	N
	FeSi ₂ Ti	N	N
	Al ₈ Fe ₅ Si ₇	P	N
	CaAl ₂ Si ₂	N	P
	Al ₆ CaFe ₄ Si ₈	P	N
	OVERALL	N	N

Legenda

+ = *increase*

0 = *unvaried*

÷ = *decrease*

P = *moving towards +*

N = *moving towards ÷*

5 FURTHER CHALLENGES

In these experiments, the heating rate and the cooling rate have been kept constant for all the treatments. The cooling rate could also be investigated, in order to have an extra parameter for controlling silicon solidification and microstructure.

It was demonstrated that the distribution of elements in the intermetallic phases changes by annealing, but the refining effect has hindered some of the transformation. Dubrous and Anglezio (**Dubrous et al., 1991**) found that there is a change in amount of the different phases upon annealing. Especially the amounts of quaternary phases of Al-Ca-Fe-Si increased upon annealing at 900°C. Experiments in a non-oxidative atmosphere can verify the reaction mechanism proposed by **Margarita (1991)**. It would be interesting to analyse separately the effect of the melting step and the effect of the annealing. The same analysis carried out in chapter 3 can be performed on a sample treated at 1200°C for 17 hours without a melting step, in order to quantify the differences and separate refining and annealing effects with higher effectivity.

It is known that silicon grain size is not affected at the temperatures considered in this study. On the one hand it can be supposed that the structure of silicon is more flexible at the temperature ranges considered so far. The liquid compounds are allowed to move through the grain boundaries. On the other hand, diffusion of dissolved elements in silicon might not be disregarded, as proved in other previous works on Al-Si alloys.

Many samples show a narrower distribution in the parameters analyzed, for example in area and aspect ratio. This increases the control on the average values. The problems related to the production of dimethyl-dichlorosilane are dependent on the size distribution of the intermetallics. If a proper size

distribution is reached before the process by performing a controlled solidification of silicon, the quality of the product can be improved. The production of silicones with silicon with controlled thermal history can be an interesting challenge to check if the quality of the final product is actually increasing.

REFEFRENCES

Amundsen, A.H., 2013. Strukturkarakterisering av Si del 1. Salten ovn 2-prøve tynnstøp~3 cm.

Anglezio, J.C. et al., 1990. Characterization of Metallurgical Grade Silicon. *Journal of Materials Research*, 5, pp.1894–1899.

Aylward, G.H., F., T.J.V., 2008. *SI chemical data. 6th edition ed. 2008: Wiley.* 6th edition., Wiley.

Barin, I., 1989. *Thermodynamical Data of Pure Substances*, Weinheim: VCH Verlags Gesellschaft.

Berget, K.H., 2014. *Private communication*, Trondheim, Norway.

Bernardis, S., 2012. *Engineering impurity behaviour on the micron-scale in metallurgical-grade silicon production*. Cambridge, USA: Massachusetts Institute of Technology.

Bird, R.B., S., W.E. & Lightfoot, E.N., 1976. *Transport Phenomena*, John Wiley and Sons.

Bjordal, M., 1990. *Studier av en faseovergang i 58% ferrosilisium ved hjelp av elektronmikroskopi - Hovedoppgave i materialfysikk*. Master thesis. Trondheim, Norway: NTH Norge tekniske Høgskole.

Boomgaard, J. van den, 1984. Stability of the high-temperature phase FeSi₂. *Journal of the iron and steel institute*.

Cahn, J.W., 1956. The kinetics of grain boundary nucleated reactions. *Acta Metallurgica*, 4, pp.449–459.

Ceccaroli, B., L., O., 2003. Solar grade silicon feedstock. In *Handbook of photovoltaic science and engineering*. John Wiley and Sons.

Chung, H., 2010. Effects of retrograde solubility on the purification of MG-Si during fractional melting. *Solar energy materials & Solar cells*, 2010. 95: p. 45-48., (95), pp.45–48.

Collins, C.B., C., R.O., 1957. Properties of silicon doped with iron or copper. *Physical review*, 108(6), pp.1409–1412.

deHuff, J. A., 1969. The structure of ferro-silicon. *Electrical furnace proceeding*, pp.167–174.

Dons, A.L., 2009. Final report Si-struc-SINTEF F9400.

Dubrous, F., A., J.C., 1991. Structure and behaviour of metallurgical grade silicon. In 48th Electrical furnace conference. pp. 33–34.

Engh, T., 1992. *Principles of refining metallurgy* 1st ed., New York (USA): Oxford University press.

Fisher, D.J., 1998. *Diffusion in Silicon: 10 years of research*, Trans Tech Pubn.

Flemings, M.C., 1971. Segregation in castings and ingots. *Solidification*, pp.311–340.

Garcia, M., 2014. Oppvarming av støp: private communication.

Gaskell, D., 2008. *Introduction to the thermodynamics* 5th ed., New York (USA): Taylor and Francis.

Graff, K., P., H., 1981. The properties of iron in silicon. *Solid-state science*

and technology, 128(3), pp.669–674.

Hoel, J.O., 2014. *Fluidized bed reactor presentation (private communication)*, Trondheim, Norway.

Hondros, E.D., S., M.P., 1983. *Interfacial and surface thermochemistry*, North-Holland: Cahn R.W. and Haasen P.Eds.

Hopkins, J., R., A., 1986. Impurity effects in silicon for high efficiency solar cells. *Journal of Crystal Growth*, 75(1), pp.67–79.

Hwang, J.C.M., H., P.S. & Lewis, J.E., C., D.R., 1980. Grain boundary diffusion of aluminum in polycrystalline silicon films. *Journal of applied physics*, 51(3), pp.1577–1581.

Incropera, F.P., D., D.P., 2002. *Fundamentals of heat and mass transfer*, New York: Wiley.

Isobe, T., N., H. & Hashimoto, K., 1989. Diffusion coefficient of interstitial iron in silicon. *Japanese journal of applied physics*, 27(7), pp.1282–1283.

Jo, Mi Ru, H., Yoon-Huk & Lee, Yeon Cheol, K., Yong-Mook, 2014. A nano-Si/FeSi₂/Ti hetero-structure with structural stability for highly reversible lithium storage. *Nanoscale*, 6(2), pp.1005–1010.

Knacke, O., K., O. & Hesselman, K., 1991. *Thermochemical properties of inorganic substances* 2nd ed., Berlin: Springer-Verlag.

Laroze, G., P., J-L. & Weber, G., G., B., 1992. Proceedings of the Silicon for the chemical industry. In Geiranger, Norway, pp. 151–163.

Lobo, S., 2010. *Modeling of the radiation lost during the casting of*

metallurgical silicon at Elkem Salten. Master thesis. Trondheim, Norway: NTNU - Norwegian University of Science and Technology.

Margaria, T., 1994. Identification and Control of the Characteristics of Silicon used in Direct Synthesis. In *Silicon for the chemical industry*. pp. 69–80.

Margaria, T. et al., 1992. Intermetallic compounds in metallurgical grade Silicon. In *INFACON*. Cape Town, pp. 209–214.

Margaria, T. et al., 1996. Silicon Refining: Experimental Studies and Industrial Means to Control Silicon Quality. *Silicon for the chemical industry*, pp.21–31.

Massalski, T.B., 1990. *Binary alloys phase diagrams*, Materials Park, Ohio: ASM International.

Morita, K., M., T., 2003. Thermodynamics of solar-grade-silicon refining. *Intermetallics*, 11, pp.1111–1117.

Møll, M.F., 2014. *Solidification of silicon: macro- and microstructure as functions of thermal history and composition*, . Department of materials science and engineering, Trondheim: NTNU - Norwegian University of Science and Technology.

Rong, H., 1992. *Silicon for the direct process to methyl-chlorosilanes*. Institutt for uorganisk kjemi, Trondheim: NTH Norge tekniske Høgskole.

Roskill, 2014. A 2014 Roskill report Silicon and Ferro-silicon: Global Industry Markets & Outlook. Available at: <http://www.roskill.com/reports/steel-alloys/silicon/leaflet>. Visualized on March 10th, 2014.

Schei, A. et al., 1992. Impurity Distribution in Silicon. *Silicon for the*

chemical industry, pp.11–23.

Schei, A., T., H., 1998. *Production of silicon alloys*, Trondheim: Tapir Forlag.

Schüssler, G., H., G., 1989. NO Patent 169831.

Shewmon, P., 1989. *Diffusion in solids*, The mineral, metals & materials society .

Sundaresan, R., B., D.E. & Fossum, J.G., 1983. Potential improvement of poly-silicon solar cells by grain boundary and intragrain diffusion of aluminum. *Journal of applied physics*, 55(4), pp.1162–1167.

Sutton, A.P., B., R.W., 1995. *Interfaces in crystalline materials*, University of Michigan, USA: Clarendon press.

Sørheim, H., 1994. *The influence of intermetallilc phases on the production of methyl-chlorosilanes*. Doctoral thesis. Trondheim, Norway: NTH Norge tekniske Høgskole.

Tang, K., Ø., E. & Tranell, G., T., M., 2010. *Thermochemical and Kinetic Databases for the Solar Cell Silicon Materials*, Trondheim, Norway: NTNU - Norwegian university of science and technology.

Tveit, H., 1988. *Størkning av 75% Ferrosilisium: Forløp. struktur og styrke*. Trondheim, Norway: NTNU.

Weber, E., 1983. Transition metals in silicon. *Applied Physics*, A(30), pp.1–22.

Zumdahl, S., 2007. *Chemistry 7th edition.*, Boston, USA: Houghton Mifflin Company.

APPENDIX

A. Analysis of the heat treated samples

Table 16: Numerical values of the parameters analyzed

Sample	Area (μm^2)	Dev STD Area (μm^2)	AR ($\pm\text{StDev}$)	#Ptc/μm^2	Maj. axis (μm)	Min. axis (μm)
600° C 17h Untreated	213.17	774.40	6.82±8.40	22	31.64	6.05
600° C 17h Treated	162.77	299.82	7.92±9.00	21	31.98	5.61
800° C 4h Untreated	155.29	326.35	8.22±9.26	21	30.72	5.47
800° C 4h Treated	171.38	383.40	8.33±9.66	20	32.19	5.38
800° C 0.5h Treated	145.13	291.92	4.92±6.36	23	25.57	6.21
900° C 0.5h Untreated	205.61	485.31	8.10±8.38	20	32.83	5.82
900° C 0.5h Treated	237.41	543.15	2.99±3.23	15	24.36	9.01
1000° C 0.5 h Untreated	208.27	491.81	6.97±8.13	20	32.35	6.44
1000° C 0.5 h Treated	215.93	311.59	2.93±4.88	16	23.62	9.60
1000° C 17h Untreated	198.54	408.97	7.03±7.62	21	32.91	6.32
1000° C 17h Treated	306.70	428.47	2.16±1.44	12	24.41	12.03
1100° C 0.5 h Untreated	265.02	701.83	6.08±7.00	19	33.48	7.30
1100° C 0.5 h Treated	293.42	469.59	2.80±2.27	12	27.38	10.33
1100° C 17h Untreated	172.77	337.50	8.03±9.97	21	31.77	5.91
1100° C 17h Treated	413.20	2176.41	2.03±1.01	14	23.48	12.17
1200° C 10 min Untreated	254.34	584.98	7.17±8.02	19	35.66	6.79
1200° C 10 min Treated	422.62	1321.80	5.19±10.50	11	35.20	10.34
1200° C 0.5h Treated	348.01	1233.45	2.56±1.63	12	24.65	10.70
1200° C 4h Treated	598.43	2406.88	2.49±1.53	10	29.84	12.65
1200° C 17h Untreated	161.19	311.41	7.38±10.12	19	29.98	6.00
1200° C 17h Treated	460.42	880.73	2.37±1.45	9	27.99	13.26

Table 17: Comparison between a treated sample, and its cross section

Parameter	1200°C 0.5h	Cross section
Area StDev (μm^2)	1233.45	372.40
Area (μm^2)	348.01	210.45
Total # particles	490	559
Aspect ratio	2.56	2.27
Major axis (μm)	24.65	19.00
Minor axis (μm)	10.70	9.99

Table 18: Relative variation for the aspect ratio

	600°C	800°C	900°C	1000°C	1100°C	1200°C
10 min						72%
30 min		60%	37%	42%	46%	35%
240 min		101%				34%
1020 min	116%			31%	25%	32%

Table 19: Relative variation for the average particle extension

	600°C	800°C	900°C	1000°C	1100°C	1200°C
10 min						166%
30 min		94%	115%	104%	111%	216%
240 min		110%				235%
1020 min	76%			155%	239%	286%

Table 20: Relative variation for the particle density

	600°C	800°C	900°C	1000°C	1100°C	1200°C
10 min						60%
30 min		109%	73%	78%	64%	65%
240 min		93%				50%
1020 min	92%			59%	64%	50%

Table 21: Relative variation for the major axis

	600°C	800°C	900°C	1000°C	1100°C	1200°C
10 min						99%
30 min		83%	74%	73%	82%	82%
240 min		105%				100%
1020 min	101%			74%	74%	93%

Table 22: Relative variation for the minor axis

	600°C	800°C	900°C	1000°C	1100°C	1200°C
10 min						152%
30 min		113%	155%	149%	142%	158%
240 min		98%				186%
1020 min	93%			190%	206%	221%

B. Analysis of annealed samples

Table 23: Numerical values of the parameters analyzed

Sample	Area (μm^2)	Dev STD Area (μm^2)	AR(\pmStDev)	#Ptc/μm^2	Maj. axis (μm)	Min. axis (μm)
Reference molten sample	217.96	674.11	5.21 \pm 6.45	29	27.22	6.60
1000° C 0.5 h Annealed	157.77	236.31	3.77 \pm 5.09	15	24.58	7.36
1200° C 0.5h Annealed	337.77	418.28	4.06 \pm 5.40	9	35.43	10.58
1200° C 17h Annealed	322.05	524.10	2.25 \pm 1.21	11	24.39	11.77
1200° C 17h Rem. Treated	246.93	746.75	2.21 \pm 1.20	12	21.93	10.46

Table 24: Relative variation compared to untreated, reference molten and treated sample at 1000°C for 0.5 hours

Ratio	Area (μm^2)	AR	#Particles/μm^2	Major axis (μm)	Minor axis (μm)
Ann./Ref. Mol.	72%	73%	52%	90%	111%
Tr./Untr.	104%	42%	78%	73%	149%
Ann./Tr.	73%	128%	92%	104%	76%

Table 25: Relative variation compared to untreated, reference molten and treated sample at 1200°C for 0.5 hours

Ratio	Area (μm^2)	AR	#Particles/μm^2	Major axis (μm)	Minor axis (μm)
Ann./Ref.	155%	78%	33%	130%	160%
Tr./Untr.	216%	35%	65%	82%	158%
Ann./Tr.	97%	158%	77%	144%	99%

Table 26: Relative variation compared to untreated, reference molten and treated sample at 1200°C for 17 hours

Ratio	Area (μm^2)	AR	#Particles/μm^2	Major axis (μm)	Minor axis (μm)
Ann./Ref.	148%	43%	38%	90%	178%
Tr/Untr.	286%	32%	47%	93%	221%
Rem. Treat/Ref.	136%	42%	41%	81%	158%
Ann./Tr.	70%	95%	122%	87%	89%

C. Chemical analysis

Table 27: Results of the XRF analysis and melting ranges (°C) calculated by SiStruc® for the studied MG-Si

Element	Amount (%wt.)
Fe	0.50
Ca	0.05
Al	0.20
Ti	0.05

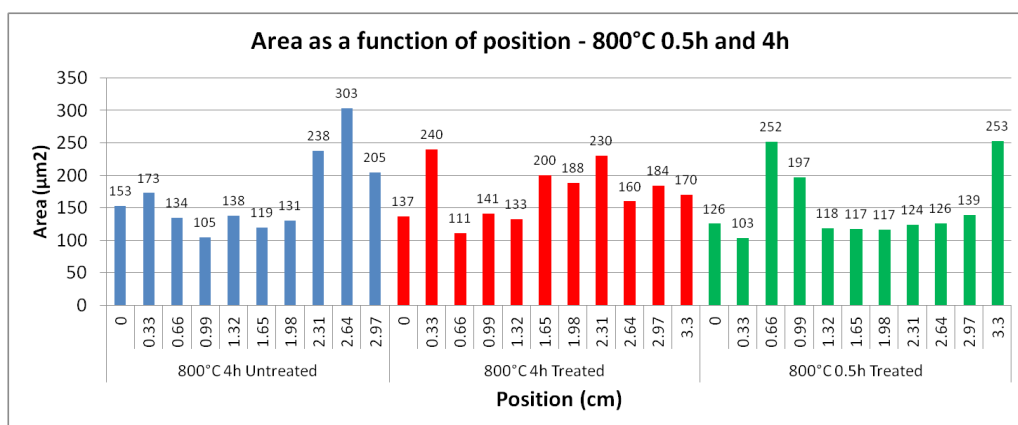
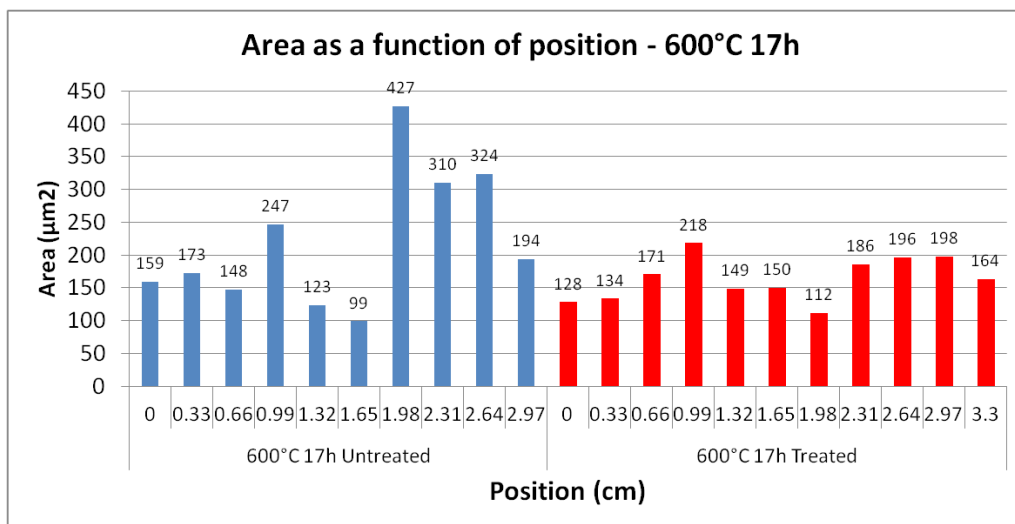
Phase	Amount (%wt.)	Melting range (°C)	
FeSi ₂	0.46	1052	913
TiSi ₂	0.01	986	576
TiFeSi ₂	0.09	986	821
CaAl ₅ Fe ₇ Si ₈	0.20	913	840
Al ₈ Fe ₅ Si ₇	0.02	904	883
CaAl ₂ Si ₂	0.18	895	576
Al ₃ FeSi ₂	0.01	851	573

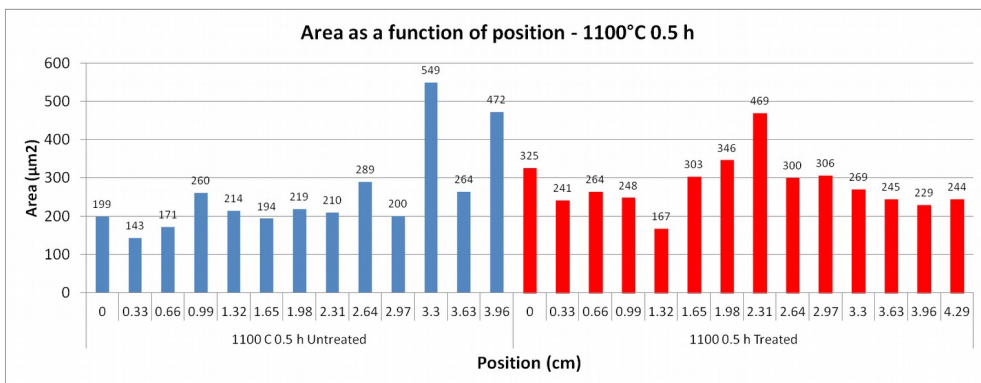
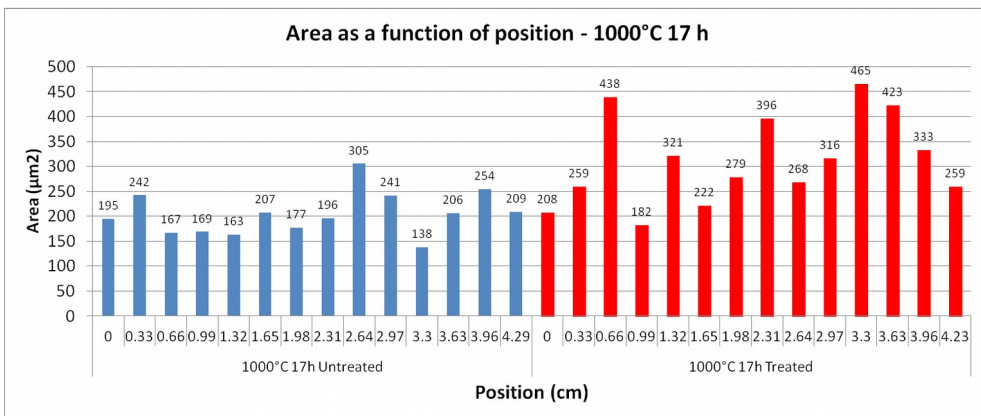
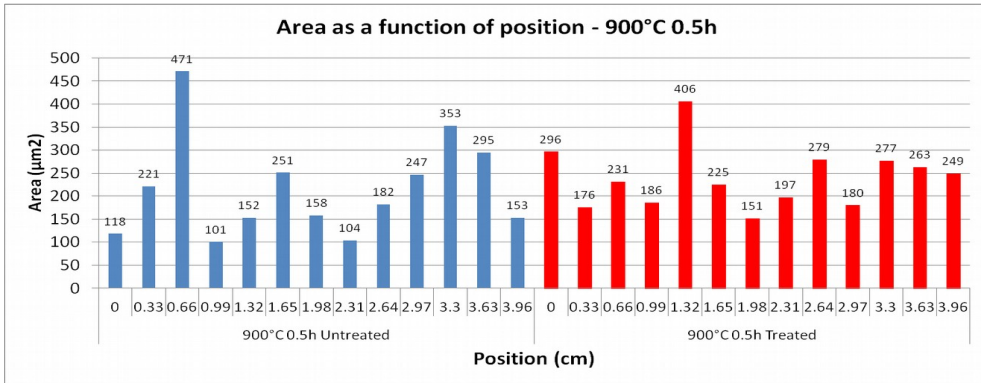
Table 28: Chemical analysis for sample annealed at 1200°C for 17 hours

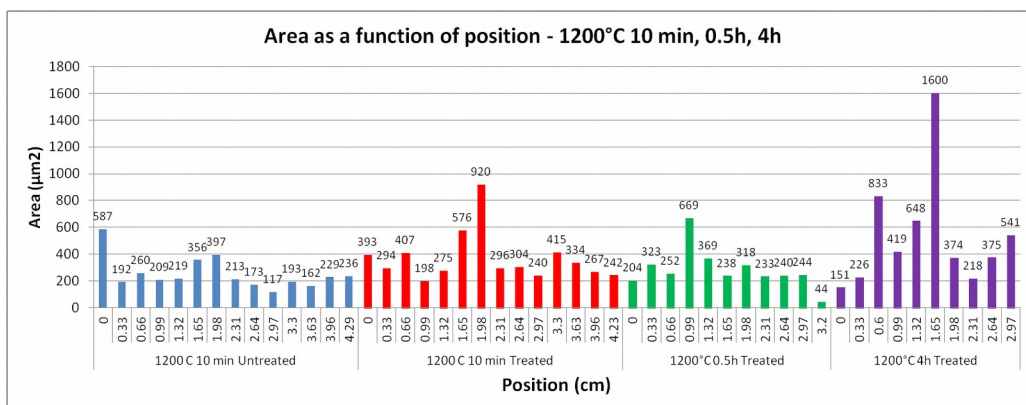
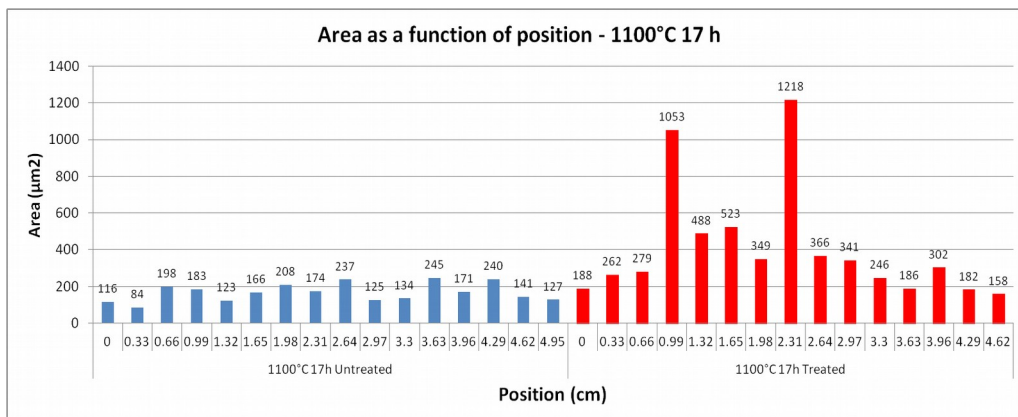
Position (cm)	%Si	%Al	%Ca	%Fe	%Ti
0.00 – 0.63	99.417	0.145	0.044	0.257	0.017
0.83 – 1.46	99.577	0.047	0.010	0.235	0.016
1.66 – 2.29	99.488	0.081	0.020	0.277	0.018
2.49 – 3.12	99.397	0.155	0.061	0.255	0.016
3.32 – 3.95	99.319	0.172	0.061	0.306	0.021
Average	99.957	0.120	0.039	0.266	0.018

D. Position profiles in the samples analyzed

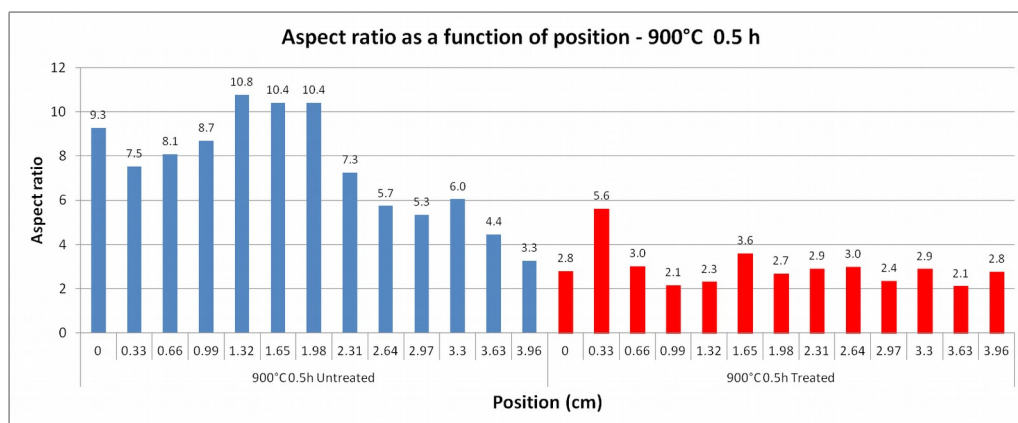
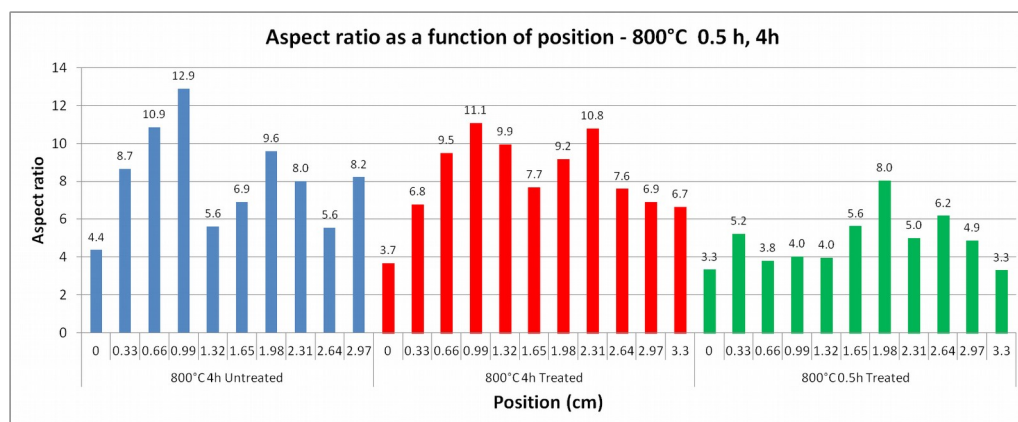
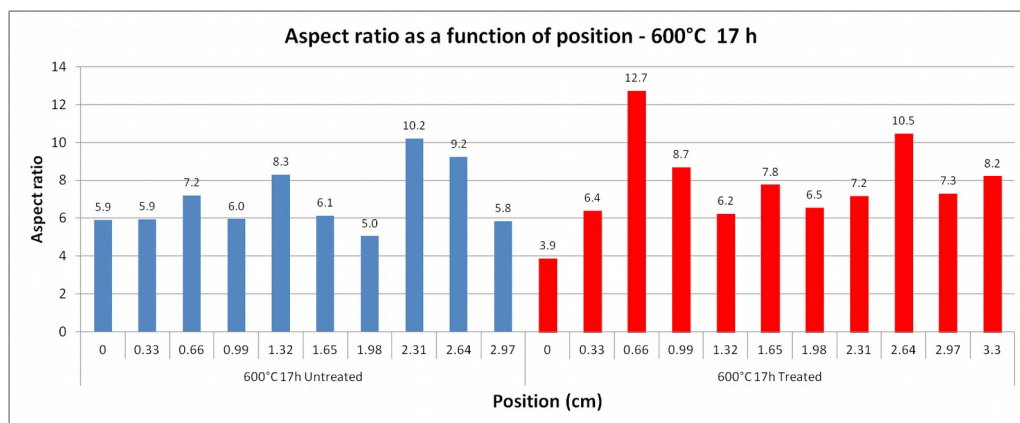
D.1 Area

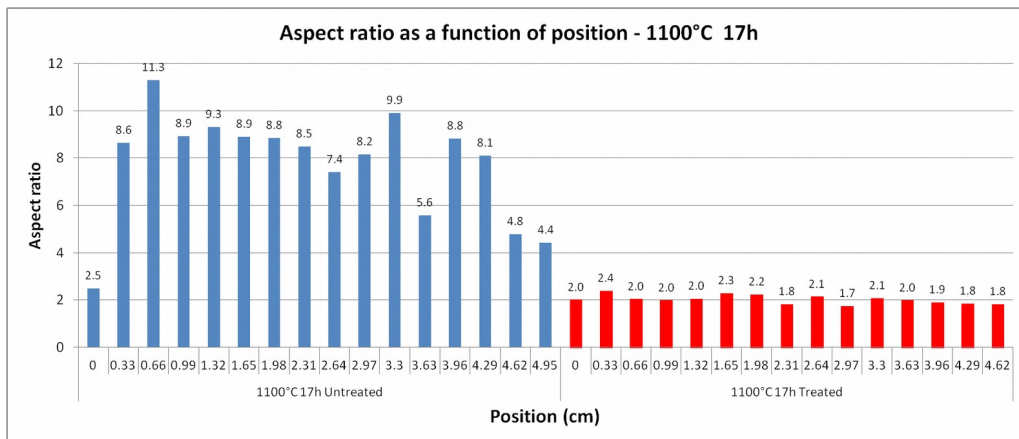
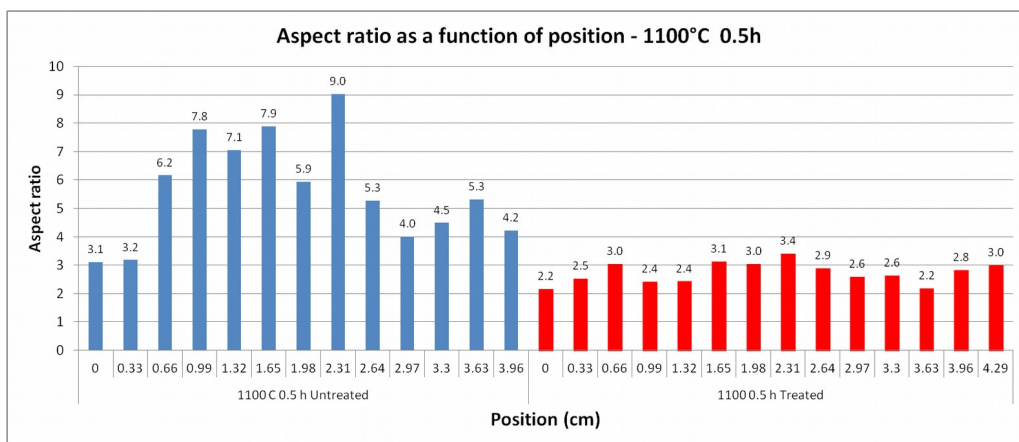
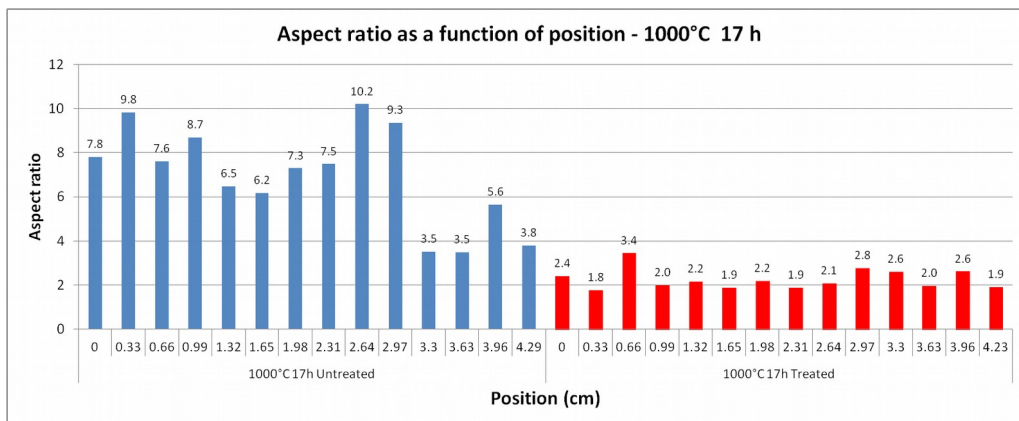


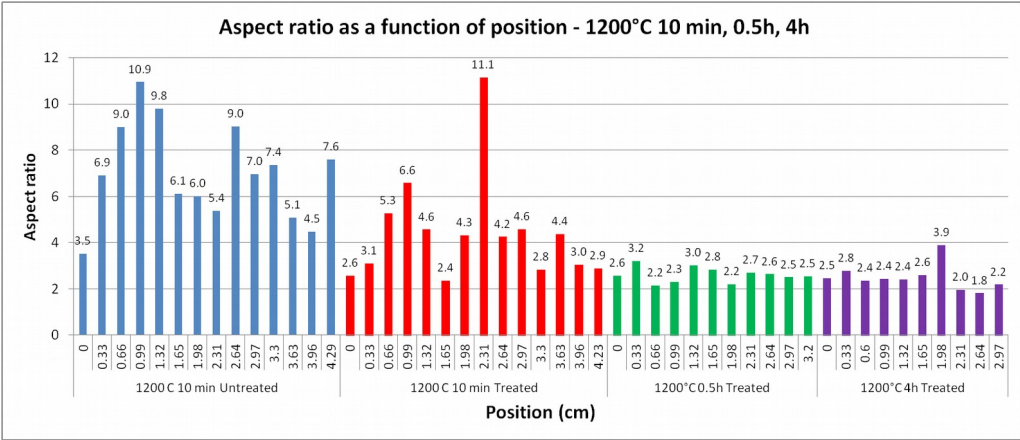




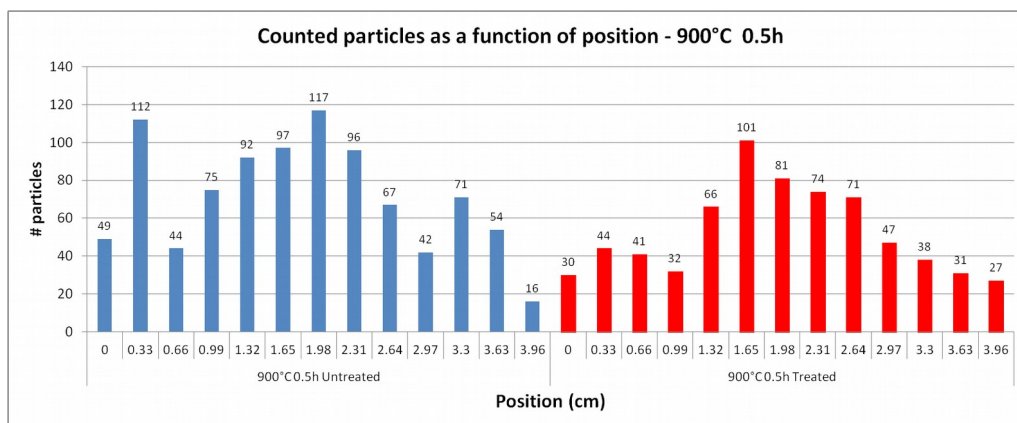
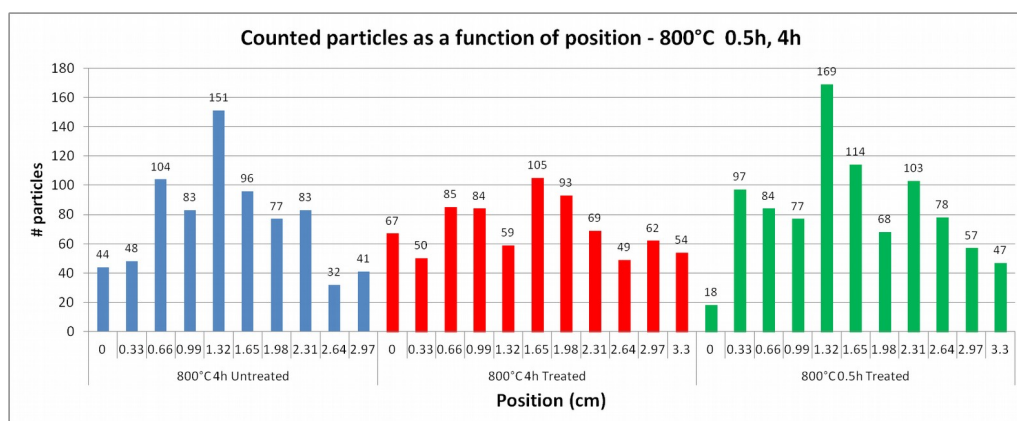
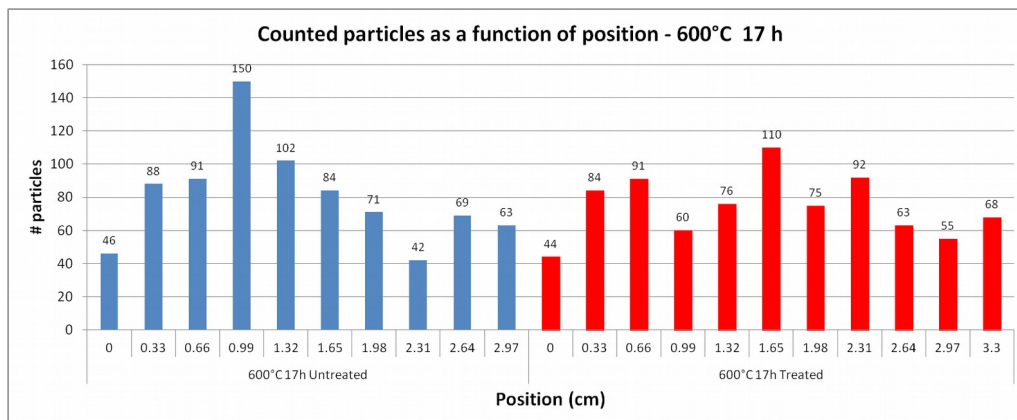
D.2 Aspect ratio

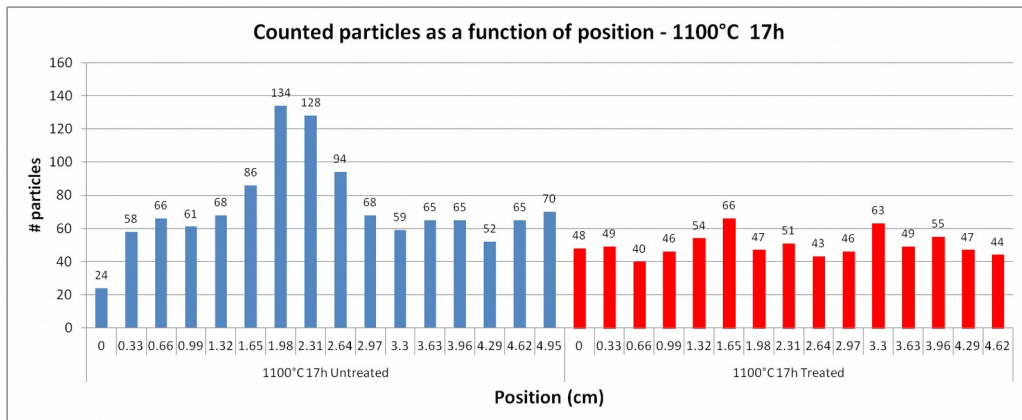
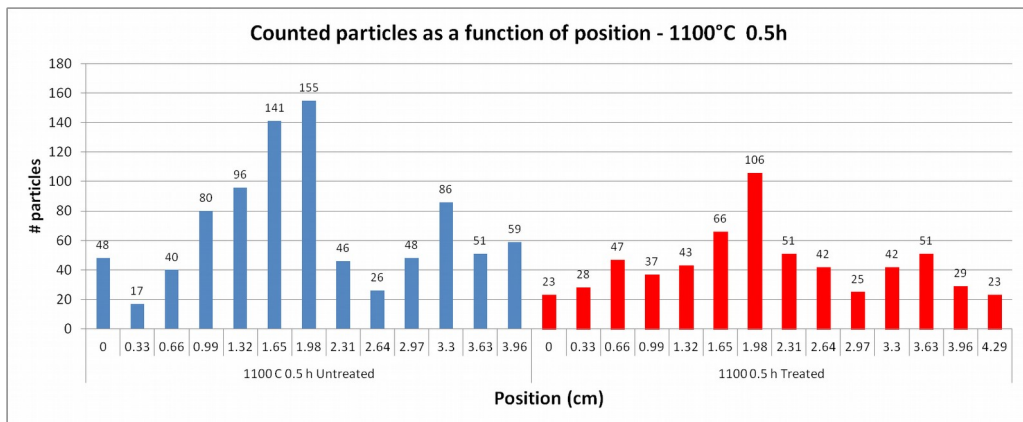
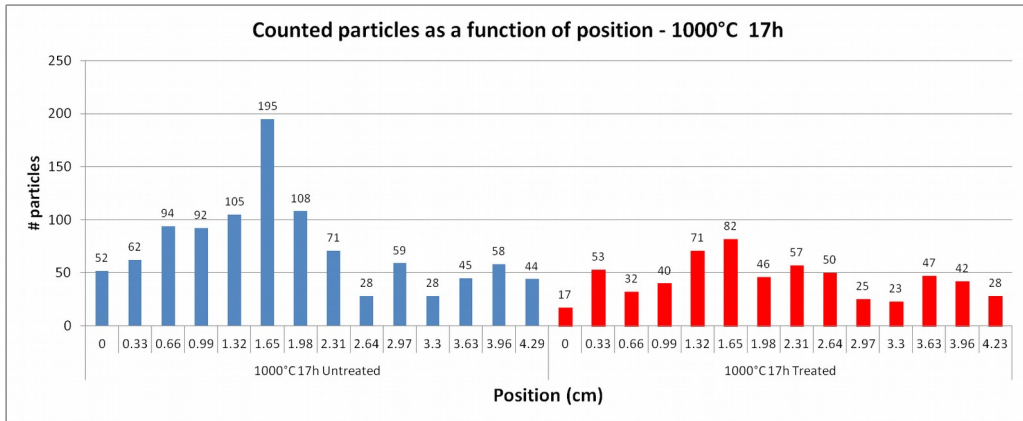


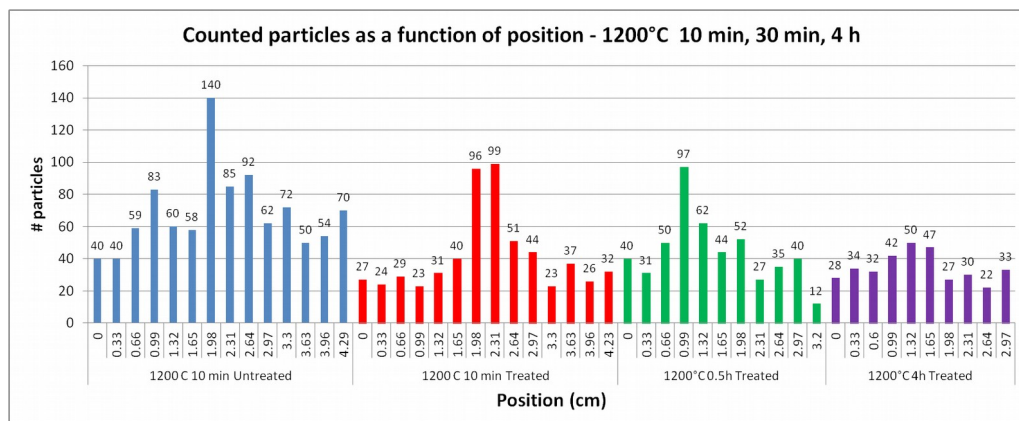




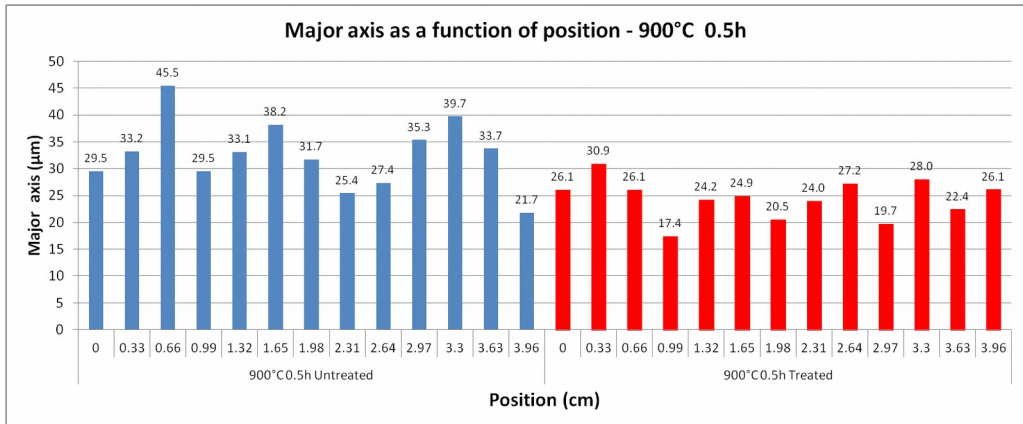
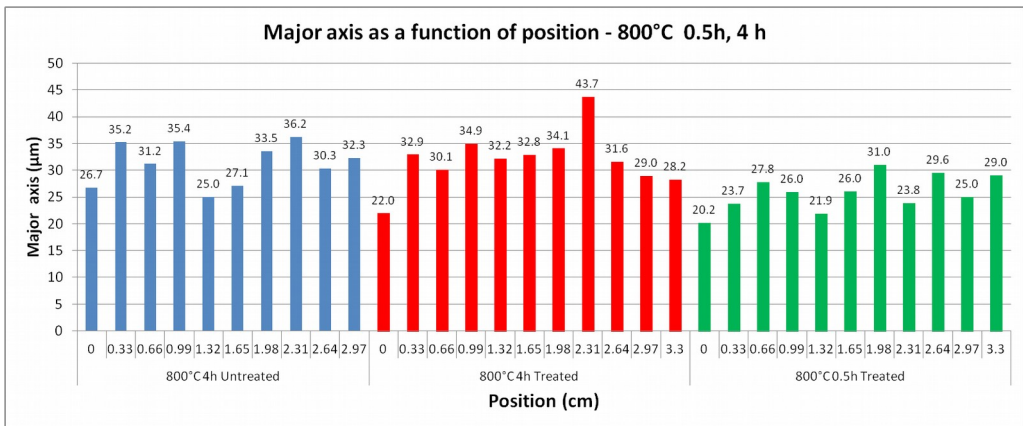
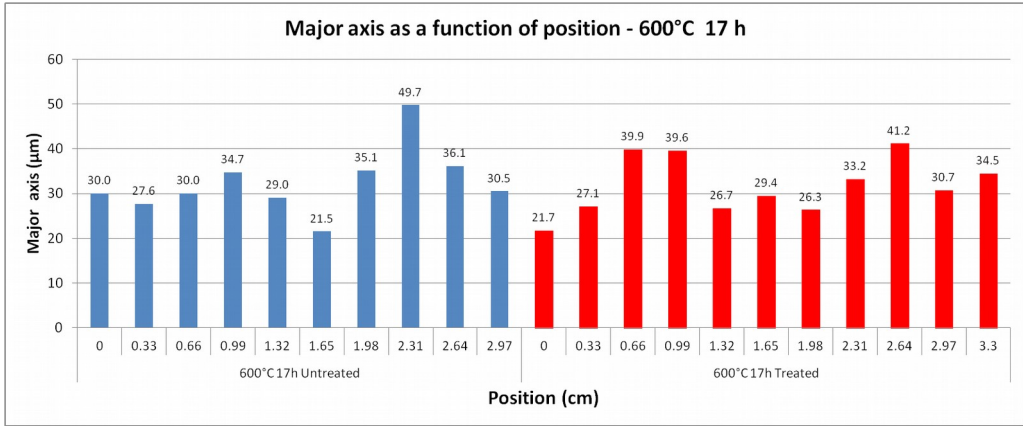
D.3 Counted particles

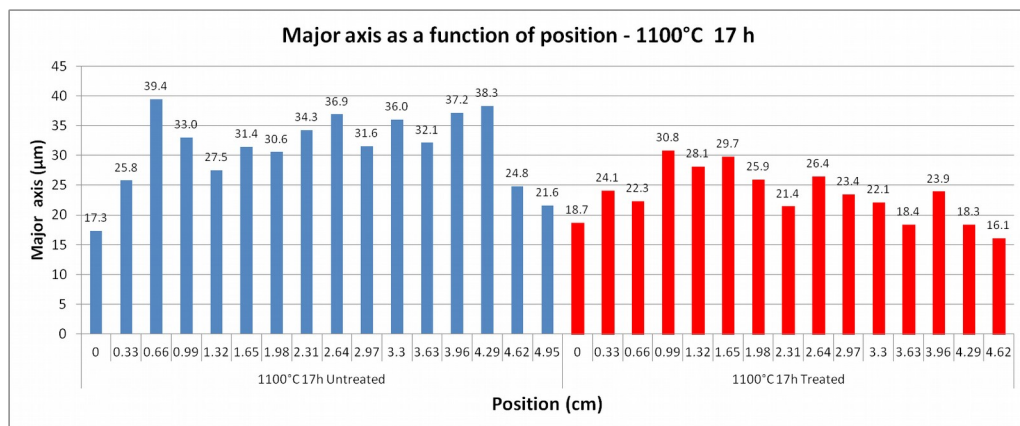
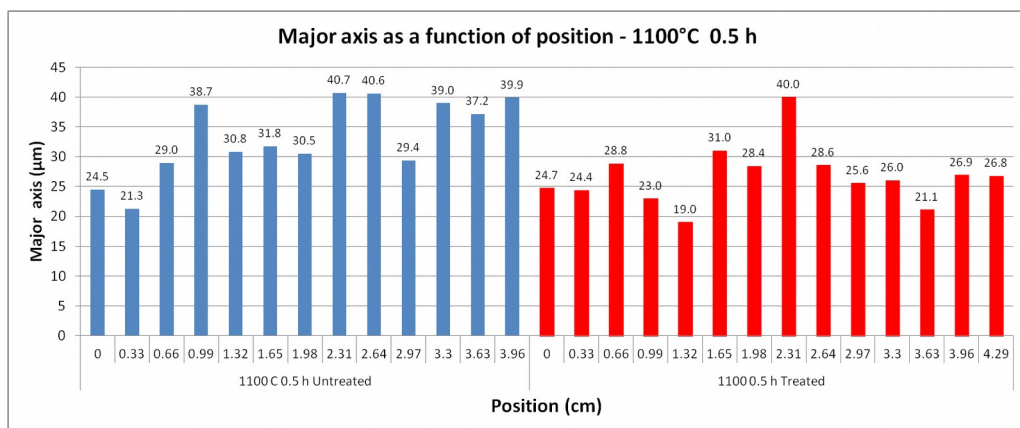
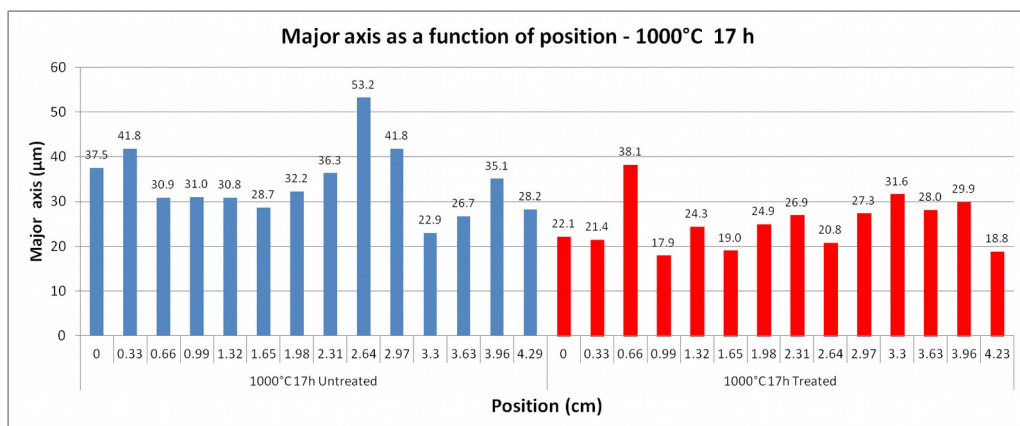


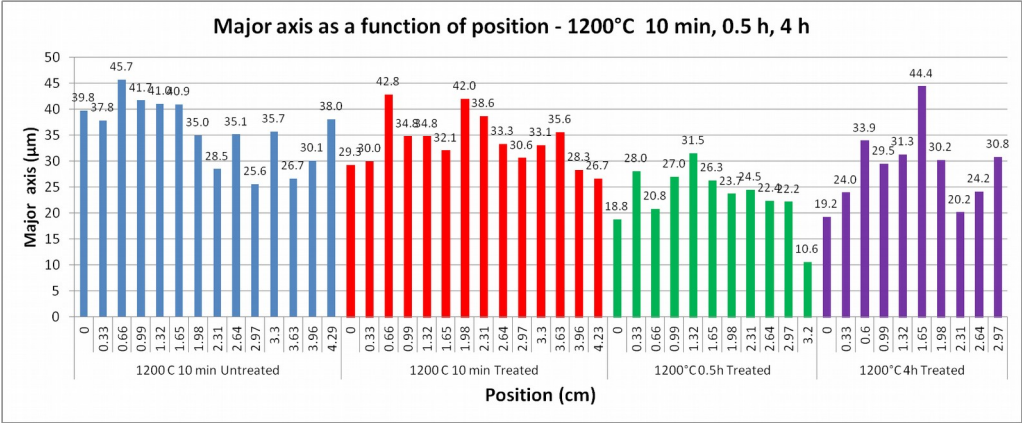




D.4 Major axis







D.5 Minor axis

